Authigenic Carbonate Burial and Its Impact on the Global Carbon Cycle: A Case Study from Late Devonian Strata of the Western Canada Sedimentary Basin

by

Sean Gazdewich
B.Sc., Carleton University, 2018
A Thesis Submitted in Partial Fulfillment of the
Requirements for the Degree of

MASTER OF SCIENCE

in the School of Earth and Ocean Sciences

Authigenic Carbonate Burial and Its Impact on the Global Carbon Cycle: A Case Study from Late Devonian Strata of the Western Canada Sedimentary Basin

by

Sean Gazdewich
B.Sc., Carleton University, 2018

Supervisory Committee

Dr. J.M. Husson, Supervisor
(School of Earth and Ocean Sciences, University of Victoria)

Dr. L.A. Coogan, Departmental Member
(School of Earth and Ocean Sciences, University of Victoria)

Dr. C.R. Barnes, Departmental Member
(School of Earth and Ocean Sciences, University of Victoria)

ABSTRACT

It has been hypothesized that authigenic carbonate minerals, formed within the pore spaces of marine siliciclastic formations during early diagenesis, may have had a substantial influence on the global carbon cycle, particularly in times of low oxygen in Earth history. According to this idea, alkalinity is generated via anaerobic organic matter degradation, resulting in carbonate oversaturation and the precipitation of low δ^{13}C carbonate cements. If a substantial amount of ^{13}C-depleted carbonate was sequestered in this authigenic sink, the δ^{13}C of dissolved inorganic carbon (DIC) in the global ocean would be driven to more positive values without significant organic carbon burial - a signal which would be recorded in marine carbonates. Research presented herein tests this hypothesis from newly acquired lithostratigraphic and coupled stable carbon and oxygen isotope data of Upper Devonian limestone and black shale formations preserved within the Western Canada Sedimentary Basin. The Late Devonian includes a mass-extinction event, and is characterized by pervasive ocean anoxia and a dramatic reduction in platformal carbonate sediment deposition. As such, it has been hypothesized to represent an ideal time for the emergence of an active authigenic carbonate sink. Results show that both basinal shale (Besa River and Exshaw formations) and platform carbonates (Wabamun Group and its equivalents), record a δ^{13}C signal that is within the expected range of Devonian seawater (3‰ to -2‰), signifying that precipitated authigenic carbonate had no influence on the isotopic composition of DIC. It was observed, however, that evaporitic depositional settings can accumulate carbonate sediment with low δ^{13}C values (down to -8.4‰), potentially caused by local water column organic matter respiration during prolonged water-mass residence in a restricted marginal marine setting. If such depositional environments were globally pervasive, such as during during global sea-level lows, it is plausible that the carbon isotope mass balance would be affected.

Contents

List of Tables

List of Figures

ACKNOWLEDGEMENTS

This thesis would not have been possible without the contributions of many people.

First and foremost, I would like to thank my supervisor Jon Husson for his guidance and patience over the course of my work. His valuable suggestions and edits greatly improved the quality of this research. I would like to thank Tyler Hauck for providing assistance and guidance in the field as well as for his help in acquiring core samples from the government of Alberta. Our discussions on the Devonian stratigraphy of Western Canada have proven invaluable. Completion of this thesis was expediated by helpful laboratory assistance from Connor Vanwieren and Erinn Raferty. I also wish to thank my fellow graduate students Mariko Cappello, Ben Kumpf and Ahron Cervania for their help with troubleshooting the numerous errors I encountered with Matlab, Python and Latex. Parks Canada is thanked for allowing me access to field sites situated within Jasper National Park. The Alberta Energy Regulator and the BC Oil & Gas Commission are thanked for allowing me access to the core sections. Finally, I would like to thank all my family and friends, including the UVic SEOS community, whose moral support these last two years have been invaluable to the successful completion of my research.

Research funding for this project was provided through an NSERC Discovery grant awarded to Dr. Jon Husson.

Chapter 1

Introduction

Geochemical records of ancient shallow-water carbonates are archives of the evolutionary history of Earth's climate and environment. These records are especially important when investigating events in deep time, such as the Precambrian and the Paleozoic Era, for which there is no oceanographic information that comes from preserved deep seafloor (the oldest ocean crust is from the Mesozoic [Müller et al., 1997]). The stratigraphic variation in δ^{13}C of shallow-water carbonates is used as a proxy to interpret the mass fluxes of carbon into sedimentary reservoirs [Ripperdan, 2001], although care must be taken to disentangle global from local signals. When global signals are presumed to be found, profiles of δ^{13}C values have also been used as a tool for global chronostratigraphic correlation, especially for time periods that lack index fossils, and as an important parameter for constraining Earth systems models [Kump and Arthur, 1999, Berner and Kothavala, 2001]. However, recent research has called into question the common framework for interpreting stable carbon isotope records, postulating that a combination of local biogeochemical and diagenetic processes can decouple the chemistry of carbonate sediments from that of the global ocean [Oehlert and Swart, 2014, Dyer et al., 2015, Geyman and Maloof, 2019, Jones et al., 2020].

One problem of particular interest is how to explain large $\delta^{13}C$ variability found in Precambrian carbonates [Halverson et al., 2005, Johnston et al., 2012, Grotzinger et al., 2011]. Sustained high δ^{13}C values ($> +5‰$), especially in the Neoproterozoic, imply high rates of organic carbon burial, further implying a coeval increase in the release of oxygen to the ocean-atmosphere system through oxygenic photosynthesis [Kump and Garrels, 1986]. Assuming that primary production and

respiration is the primary control on oxygen levels in the ocean-atmosphere system, this interpretation is not corroborated by other geochemical proxies indicating low levels of oxygen at this time, unless high production of oxygen in the Neoproterozoic is balanced by a coeval rise in oxidative weathering of the continents or an increase in mantle-derived reducing gases [Catling and Claire, 2005]. To explain this discrepancy between $\delta^{13}C$ records and levels of atmospheric oxygen, a recent study has proposed that the precipitation of carbonate minerals within the pore spaces of marine siliciclastic formations during early diagenesis may have provided an alternate carbon sink, one that can drive $\delta^{13}C$ of seawater to more positive values without necessitating a coupled release of O_2 to the atmosphere [Schrag et al., 2013]. Sulfate (and iron) reduction during anaerobic recycling of organic matter raises the carbonate saturation state of sedimentary pore waters, encouraging the precipitation of authigenic carbonate with low $\delta^{13}C$ values [Higgins et al., 2009]. Because of lower atmospheric O_2, this authigenic sink would have been prominent during the Precambrian, and could have reemerged during transient ocean anoxia events in the Phanerozoic Eon (541 - 0 million years (Ma.)). A similar hypothesis considers the removal of inorganic carbon with low $\delta^{13}C$ values through hydrothermal seafloor weathering of basalt as a potential third sink for carbon [Bjerrum and Canfield, 2004]. This hypothesis postulates that ocean crust carbonitization is a significant carbon sink. Evidence suggest that the presence of hydrothermal carbonates are ubiquitous in Archean greenstone belts [Sleep and Zahnle, 2001]. Gradients in $\delta^{13}C$ between deep marine carbonate precipitation may have been large enough relative to shallow-water carbonates to affect the carbon isotope composition of DIC. The central difference between these hypotheses is the locus of burial of carbonate with low $\delta^{13}C$ values: siliciclastic deposits [Schrag et al., 2013] or in carbonated seafloor [Bjerrum and Canfield, 2004].

Evaluating the importance of $CaCO_3$ buried in siliciclastic sediments has been the basis of several recent research publications and has been tested with data from a variety of time periods throughout Earth history [Sun and Turchyn, 2014, Saitoh et al., 2015, Zhao et al., 2016, Mitnick et al., 2018, Barnes et al., 2019]. Here, an attempt is made to quantify the amount and isotopic composition of $CaCO_3$ buried in black shale units, and the resultant effects on seawater chemistry, during the Late Devonian, a time of upheaval in Earth's history that included the Frasnian-Famennian mass extinction and the Hangenberg crisis

[Kaiser et al., 2016]. Geologically, this was marked by a widespread crash in shelf carbonate systems, and accompanying global rise in siliciclastic deposition [Peterhänsel et al., 2008, Kaiser et al., 2016, van Loevezijn and Raven, 2017]. The presence of positive δ^{13}C excursions in globally dispersed equivalent strata and the widespread deposition of organic-rich black shales, suggest a significant perturbation of the carbon cycle [Kaiser et al., 2016]. Strata of this age are well preserved throughout the subsurface of Western Canada and outcrop prominently in the Rocky Mountain Front Ranges, covering an areal extent of 100,000's of km^2. Sedimentary facies representing the deep basin, slope and carbonate platform depositional environments are preserved, providing an excellent opportunity to undertake a field test of the authigenic sink hypothesis.

The research presented herein includes new lithostratigraphic, δ^{13}C and δ^{18}O data from Famennian-aged shallow-marine carbonate and deep marine siliciclastic formations found within the Western Canada Sedimentary Basin (WCSB). These data are used to evaluate the carbon isotope record of platform carbonates in response to potentially increased carbonate burial in the deep basin. Supplemental to these records are measurements of inorganic carbon abundances in marine shales to quantify the amount of carbonate burial in organic-rich siliciclastic sediments - a two-pronged approach to testing the authigenic sink hypothesis. Continued quantitative tests for this hypothesis are important because it addresses inconsistencies in carbon isotope record and how it is used to reconstruct to the global carbon cycle, and has profound implications for the geochemical evolution of the Earth system.

Chapter 2

Background

2.1 Authigenic Carbonate and the Long-Term Global Carbon Cycle

The global carbon cycle refers to the amount of carbon held within the various reservoirs that make up the Earth system and the exchange fluxes between them. These reservoirs principally constitutes the lithosphere, oceans and atmosphere, and the exchange fluxes are governed by both physically and biologically-mediated reactions [Emerson and Hedges, 2008]. For timescale >1 Ma, the production of carbon outgassed from the solid Earth is matched by its burial as organic carbon or calcium carbonate in the surface environment [Kump and Arthur, 1999, Ripperdan, 2001, Hayes and Waldbauer, 2006]. The balance between the mass of carbon being released into the ocean-atmosphere versus the amount that becomes buried is strongly influenced by geological processes. Carbon may be released as CO_2 into the atmosphere through outgassing at active volcanoes or during metamorphic reactions as carbonate rocks are subducted into the mantle. Owing to the relatively short atmospheric residence time of carbon (<10 years) [Kump et al., 2004, Allen et al., 2014, Harde, 2017], the atmosphere serves effectively as a conduit for carbon exchange between the lithosphere reservoir and the ocean reservoir. Carbon is present in the oceans in both inorganic or organic form. Dissolved inorganic carbon (DIC) forms in the ocean system from the free exchange of CO_2 between the atmosphere and ocean. DIC is also formed through silicate and/or carbonate weathering on the continents, and transported into the ocean by river drainage systems. DIC is eventually converted into calcium carbonate ($CaCO_3$)

by calcifying organisms, and later deposited as carbonate sediment - although in the Precambrian, the lack of animals meant $CaCO_3$ burial must have been accomplished by microbial or inorganic processes, including direct in-situ precipitation as seafloor cements [Grotzinger and James, 2000, Higgins et al., 2009]. Like inorganic carbon, organic carbon is also present in the oceans as two forms: (1) dissolved organic carbon (DOC), including from soils, terrestrial plants and from algae, and (2) particulate organic carbon (POC), composed of living or deceased organisms (both terrestrial and marine). Carbon both in inorganic or organic forms will become buried over time and thus returned to the lithosphere.

Since inherent limitations of the rock record (and our knowledge of it) prevent the direct measurement of carbon mass fluxes in deep time, evaluation of carbon cycling across Earth history is attempted most commonly by the analysis of carbon isotopes of sedimentary phases, either from marine carbonate ($\delta^{13}C_{carb}$) or organic carbon ($\delta^{13}C_{org}$). δ^{13}C is a measure of the ratio of ^{13}C to ^{12}C relative to a standard in a sedimentary phase. Sediment with a positive δ^{13}C value will be relatively enriched in ^{13}C, while sediment that has a negative δ^{13}C value is relatively depleted in ^{13}C compared to the reference standard. Determined by mass balance equations, changes in the carbon isotopic composition of marine carbonate and organic carbon matter reflects the change in the fraction of organic carbon burial relative to total carbon burial through time [Kump and Arthur, 1999]. This relationship is derived from the following isotope mass balance equation:

$$\frac{d}{dt}(M\delta_{carb}) = F_w\delta_w - F_{b,carb}\delta_{carb} - F_{b,org}(\delta_{carb} + \Delta B) \tag{2.1}$$

where M represents the total amount of inorganic carbon in the ocean-atmosphere system, F_w the combined weathering flux (which includes the input from volcanic outgassing) and its corresponding carbon isotope composition (δ_w), $F_{b,carb}$ and $F_{b,org}$ are the burial fluxes of both marine carbonate and organic carbon and δ_{carb} and $\delta_{carb} + \Delta B$ are the respective carbon isotope compositions of these burial fluxes. ΔB represents the isotopic difference between organic matter and carbonate, and when combined with δ_{carb}, substitutes for δ_{org}. Assuming steady state conditions, whereby the input of carbon is balanced by the output of carbon via burial, this equation can

be further simplified:

$$f_{org} = \frac{\delta_w - \delta_{carb}}{\Delta B} \tag{2.2}$$

where f_{org} represents the fraction of organic carbon buried (i.e. $F_{b,org}/(F_{b,carb}+F_{b,org})$. If we assume that ΔB and the carbon isotope composition of the weathering flux remain constant over time, then it becomes clear that the only variable affecting δ_{carb} is the fraction of organic carbon burial. Kinetic isotope fractionation of carbon during photosynthesis results in the production of organic carbon matter that is depleted in ^{13}C ($<< 0‰$). The removal of carbon through the burial of low δ^{13}C organic matter will result in an overall δ^{13}C enrichment in the carbon isotope composition of the DIC pool. Calcium carbonate is precipitated in isotopic equilibrium with seawater, and therefore records the isotopic composition of DIC. Thus, an increase or decrease in the organic burial sink through variations in the rates of primary production or organic matter preservation would drive carbon isotope excursions in marine DIC, which can then be recorded in buried marine carbonates or organic matter. Negative excursions may occur from the release of carbon into the oceanic-atmosphere system by the oxidation of organic matter [Ripperdan, 2001].

The burial flux of carbon through deep time also has a strong control on the oxidation state of the Earth's surface. This is because the burial of photosynthetic organic matter results in a net release of O_2 into the atmosphere [Emerson et al., 1997]. Therefore, there is an inferred coupled relationship which relates δ^{13}C in marine carbonates with atmospheric levels of oxygen, assuming other redox-sensitive elements do not act as electron donors. It is this relationship which informs Earth system models for atmospheric oxygen content throughout the Phanerozoic [Freeman and Hayes, 1992, Berner, 1998, Berner et al., 2000, Bergman et al., 2004]. However, there are instances in Earth history which challenge this framework. One such occurrence is in the Precambrian, a time period known for having both the highest and lowest recorded carbon isotope excursions in carbonates (Figure 2.1) [Halverson et al., 2005, Grotzinger et al., 2011, Johnston et al., 2012]. If these δ^{13}C values from shallow water carbonates record global seawater values, then high δ^{13}C values for marine carbonate ($>> 0‰$) are hard to reconcile with evidence that suggests low atmospheric O_2 levels [Catling and Claire, 2005]. To adress this discrepancy, it has been proposed that authigenic carbonate stored within marine

siliciclastic formations could potentially act both as a quantitatively important sink for carbon and influence the carbon isotope composition of marine DIC [Schrag et al., 2013].

Authigenic carbonate is defined as any carbonate mineral precipitated either at the sediment-water interface or within sediment pore spaces. Certain pathways of anaerobic organic matter degradation (e.g., sulfate reduction (eq. 2.3) or iron reduction (eq. 2.4)) produce alkalinity, which promotes the precipitation of carbonate minerals [Berner et al., 1970, Curtis, 1987, Coleman and Raiswell, 1993].

$$2CH_2O + SO_4^{2-} = HCO_3^- + HS^- + H_2O \tag{2.3}$$

$$CH_2O + 4Fe(OH)_3 + 7CO_2 = 4Fe^{2+} + 8HCO_3^- + 3H_2O \tag{2.4}$$

Cements produced from this process are presumed to be depleted in ^{13}C relative to ^{12}C [Irwin et al., 1977]. However, ^{13}C enrichment may occur if carbonate precipitation takes place within the zone of methanogenesis (Figure. 2.3). Despite its current occurrence at several marine localities [Mazzini et al., 2004, Ketzer et al., 2018], authigenic carbonate precipitation is thought to be uncommon in the modern ocean environment because it is inhibited by the relatively high amounts of dissolved oxygen in seawater. Nevertheless, recent modelling efforts to quantify the authigenic sink in the modern ocean has suggested that at least 1% to as high as 10% or more of marine carbon burial may be attributed to authigenic carbonate precipitation, with authigenic carbonate accumulation being greater near the coastal regions of ocean basins [Sun and Turchyn, 2014, Bradbury and Turchyn, 2019]. However, the effect of this burial sink on the carbon isotope composition of the DIC reservoir was not constrained in these studies. Time periods of expanded anoxia in the world's oceans could have favored a more prominent authigenic sink [Higgins et al., 2009]. Such conditions would have been especially dominant during the Proterozoic Eon (2500-541 Ma.) [Planavsky et al., 2014], but may have returned transiently during the Phanerozoic. If appreciable amounts of authigenic carbonate was been sequestered as low $\delta^{13}C$ cements, then this could provide a mechanism for explaining positive carbon isotope excursions without changing atmospheric O_2 (Figure. 2.4). Conversely, a negative carbon isotope excursion could be explained by a decrease in the burial flux of authigenic carbonate or by the incorporation of authigenic carbonate within carbonate shelf sediments [Schrag et al., 2013]. It is worth noting that authigenic carbonate-bearing

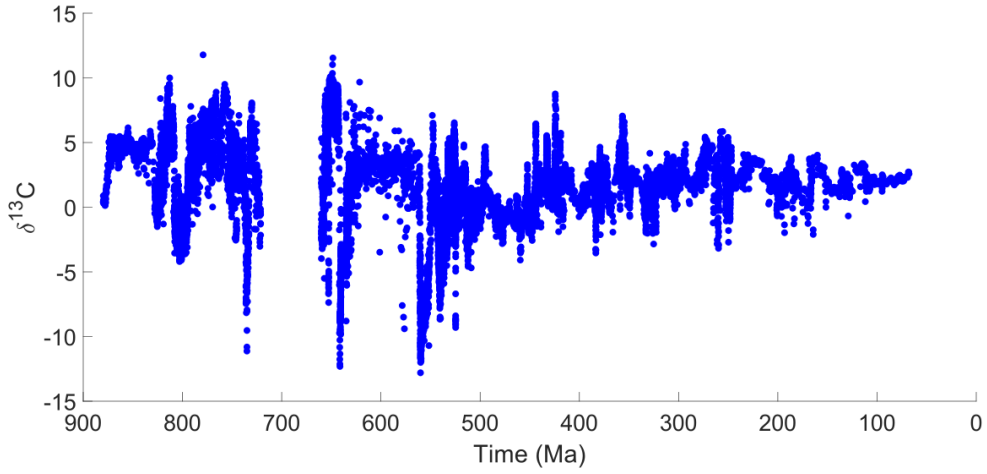

Figure 2.1: Compilation of $\delta^{13}C_{carb}$ measurements across the Neoproterozoic Era and the Phanerozoic Eon [Burns and Matter, 1993, Brasier et al., 1996, Prave, 1999, Brasier and Shields, 2000, McKirdy et al., 2001, Hoffman and Schrag, 2002, Workman et al., 2002, Halverson et al., 2004, Halverson et al., 2005, Maloof et al., 2005, Fike et al., 2006, McCay et al., 2006, Halverson and Hurtgen, 2007, Kouchinsky et al., 2007, Ishikawa et al., 2008, McFadden et al., 2008, Sawaki et al., 2008, Macdonald et al., 2009, Prave et al., 2009, Verdel et al., 2011, Husson et al., 2012, Rose et al., 2012, Pokrovsky and Bujakaite, 2015]. Blue circles mark individual sample measurements of either calcite or dolomite. Inset represents the Late Devonian period. Period interval 730 Ma to 660 Ma where no data are plotted corresponds to the Sturtian 'Snowball Earth' glaciation, with no marine carbonates of that age.

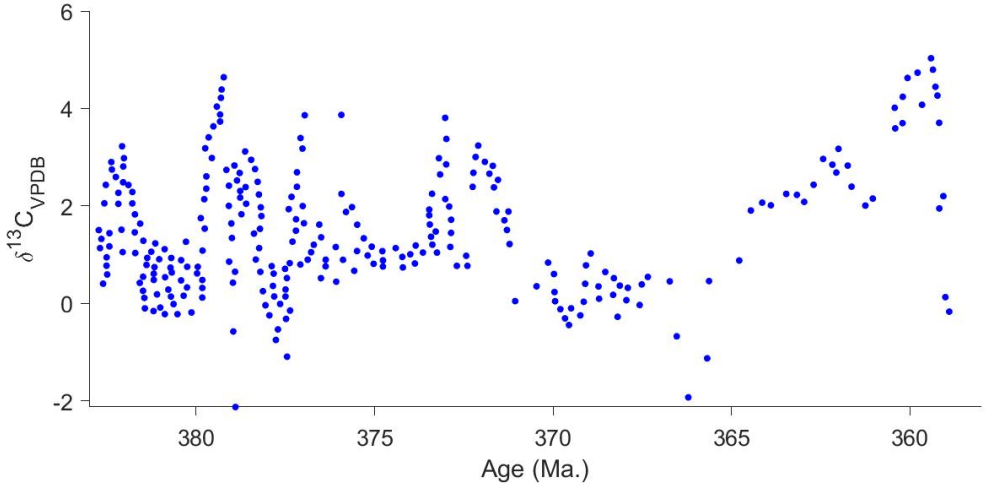

Figure 2.2: The Late Devonian portion of Figure 2.1.

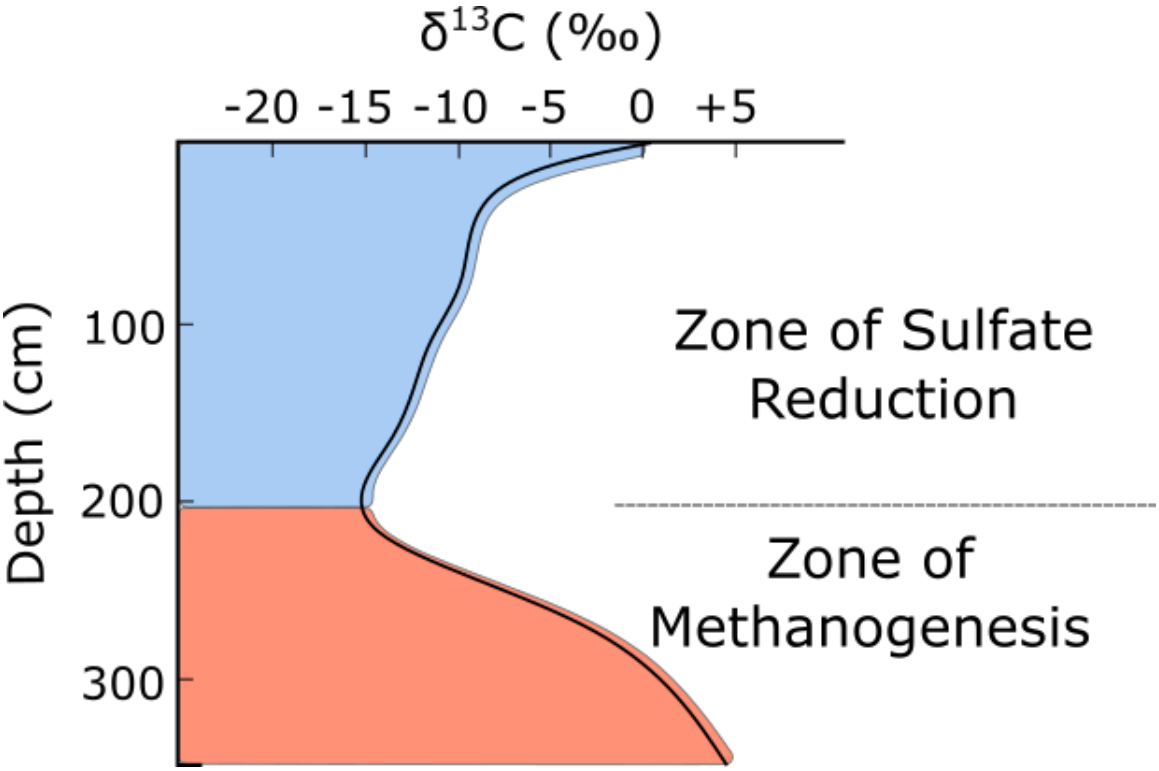

Figure 2.3: Changes with depth in δ^{13}C of DIC in sediments. The blue zone indicates the zone of SO_4^{2-} reduction, which is represented by a decrease in isotopic composition. The red zone indicates the zone of methanogenesis and is represented by an overall enrichment in pore water isotopic composition (modified from [Claypool and Kaplan, 1974]).

stratigraphic sections may have been disregarded from the chemostratigraphic literature because they originate from post-depositional processes, and are unlikely to represent a primary DIC carbon isotope signal and thus are not useful for basin-to-basin correlation purposes. Nonetheless, authigenic carbonate-bearing formations provided valuable insight into carbon cycling dynamics and therefore merit investigation. One test of the authigenic sink hypothesis is to investigate marine sedimentary formations from instances in Earth history when boundary conditions existed that promote the precipitation of authigenic carbonate. One such time period was the Late Devonian.

2.2 Late Devonian Earth History

The Late Devonian was a crucial period in Earth's history. Hosting one of the "Big Five" mass extinction events of the Phanerozoic [Kaiser et al., 2016], biodiversity in the Late Devonian experienced large swings. Considerable debate continues as to whether or not the Late Devonian represents a true mass extinction caused by elevated extinction rates, or whether biodiversity loss was caused by reduced speciation [Bambach et al., 2004, Stanley, 2016]. In either case, evidence suggests a disturbed Earth system resulting in stressed marine and terrestrial ecosystems. Often cited as a single event, the Late Devonian mass extinction may be best understood as a series of biotic crises, each having an impact on the diversity of life.

By the beginning of the Late Devonian, an epoch which incorporates the Frasnian (382.7 – 372.2 Ma) and Famennian stages (372.2 – 358.9 Ma), the Earth was experiencing a time of relative warmth, with CO_2 levels and global surface temperatures elevated relative to present [Berner and Kothavala, 2001]. The majority of Earth's landmass was located within the southern hemisphere or near equatorial regions [Mac Niocaill and Smethurst, 1994] (Figure 2.5). An exceptional sea-level highstand caused much of the Laurentian craton to be covered by expansive epeiric seas, which allowed for the abundant deposition of carbonate rocks [Halbertsma et al., 1994]. These epeiric seas spawned the growth of many diverse marine organisms and reefal communities. Reef communites during the Devonian were primarily defined by stromatoporoid sponges, tabulate corals, calcareous algae and rugose corals (though rugose corals were predominantly relegated to the benthic zone) [Fagerstrom, 1994, Kaiser et al., 2016]. Peak species diversity

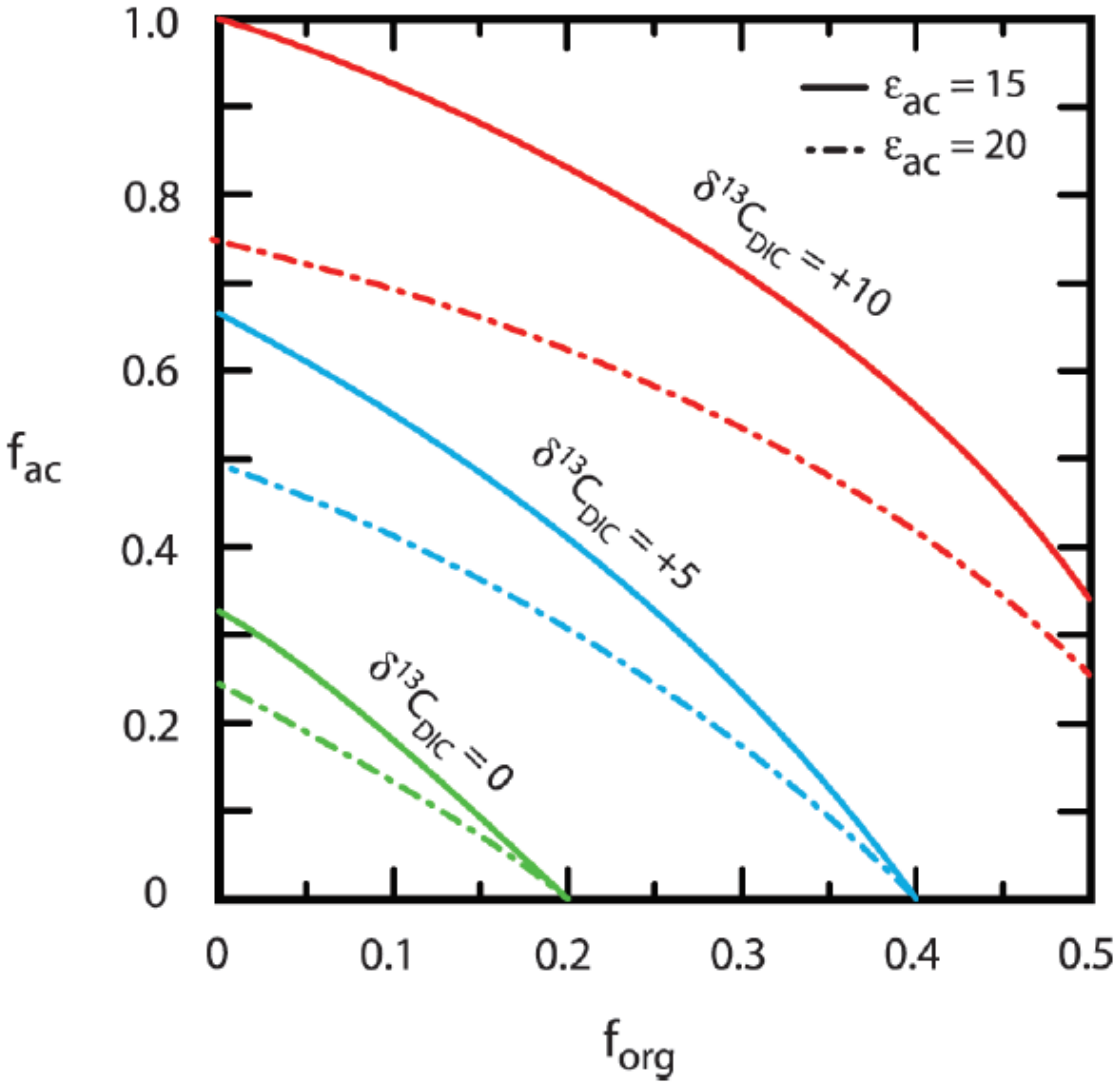

Figure 2.4: This figure illustrates the effect that the fraction of total carbonate burial that is authigenic ($f_{ac} = \frac{F_{ac}}{F_{carb}+F_{ac}}$) relative to the fraction of total carbon burial that is organic ($f_{org} = \frac{F_{org}}{F_{org}+F_{carb}+Fac}$) has on the isotopic composition of seawater. Contours represent different values of δ^{13}C of DIC, and are a function of the isotopic fractionation factor between marine carbonate and authigenic carbonate, with assumed global average values of 15 and 20‰ (modified from [Schrag et al., 2013]). For reference, the isotopic fractionation between marine carbonate and organic matter is $\approx$ 27‰.

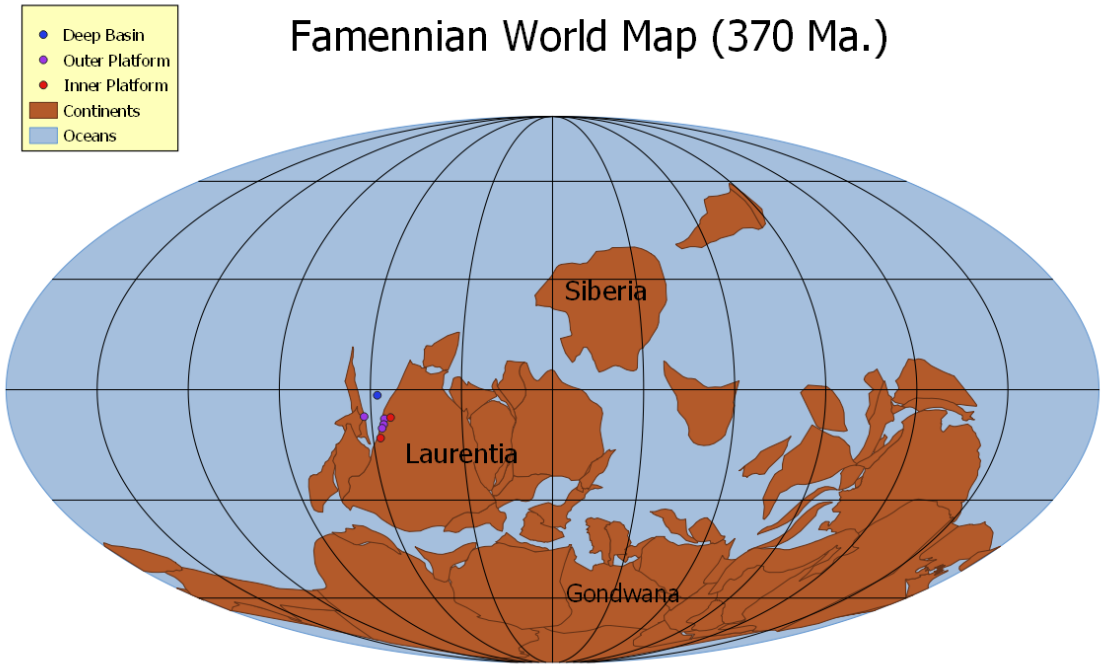

Figure 2.5: The distribution of continents during the Early Famennian. Study sections are represented by points and grouped based on their respective depositional environments (See Figure 2.8). Continental area also includes the submerged continental shelves. The names of prominent supercontinents are also labeled. The paleogeographic reconstruction is from [Wright et al., 2013], delivered via the Macrostrat API [Peters et al., 2018].

for rugose corals and stromatoporoids occurred during the Eifelian-Givetian ages [Stearn, 1988, Sorauf, 1989]. Ultimately, the Devonian proved to be the zenith for Paleozoic reefs. Metezoan reef development extended to high latitudes with the presence of vast reef belts 1000's of kilometres in extent [Copper, 1994]. Such growth may have been aided by the archipelagic configuration of continents at warm equatorial regions allowing for free circulation of ocean waters [Copper, 2002]. Life on land also made significant evolutionary developments such as the emergence of arborescence and seed-bearing trees [Algeo et al., 1995, Pawlik et al., 2020].

The Late Devonian incorporates two prominent extinction episodes: the Frasnian-Famennian (F-F) exctinction and the Hangenberg Biotic Crisis, below the Devonian-

Carboniferous boundary (D-C). These events in particular decimated coral reef communities and pelagic organisms [Copper and Scotese, 2003, Kaiser et al., 2016]. The exact mechanism(s) which initiated the onset of these events remain enigmatic. Several causes have been proposed for both the F-F extinction and the Hangenberg crisis, including bolide impacts [Claeys et al., 1992, Morrow et al., 2005], large scale magmatic events [Filipiak and Racki, 2010, Ricci et al., 2013, Rakociński et al., 2020] and glaciations [Caplan and Bustin, 1999, Streel et al., 2000]. It has been documented, however, that the timing of these events correlate with prominent positive carbon isotope excursions [Cramer et al., 2008, Myrow et al., 2011] and widespread deposition of black shale formations [Kaiser et al., 2006, Becker et al., 2016], which suggest expanded ocean anoxia during the latest Frasnian and at the Famennian-Tournaisian boundary. Supplementary geochemical proxies supports this conclusion: the precipitation of framboidal pyrite, which typically occurs at the interface between oxic and hydrogen-sulfide bearing waters [Wilkin and Barnes, 1996], has been observed in black shale formations ([Schieber and Baird, 2001, Marynowski et al., 2012, Barnes et al., 2019], this study) and trace metals enrichment in black shales [Riquier et al., 2006, Barnes et al., 2019], in particular redox-sensitive elements that accumulate in anoxic sediments (e.g., Mo, U and V). Timing of ocean anoxia also correlates with the decline in phytoplankton microfossil diversity, with organisms that typically thrive in oxic settings, observed across the Devonian/Carboniferous boundary [Riegel, 2008].

Sedimentologically, the Famennian is of interest because it is characterized by a crash in carbonate depositional systems, attributed to the extinction of marine calcifying organisms, and subsequent increase in marine siliciclastic formations (e.g. siltstones and black shales) [Kaiser et al., 2016], (Figure 2.6). Before this crash, the Middle Devonian represented a zenith of carbonate platform development [Copper and Scotese, 2003]. A combination of sustained sea-level highstand and a warm greenhouse climate ensured that carbonate reefs covered an areal extent estimated at 5 million square kilometers [Copper, 1994]. However, a sharp decline in reef building organisms began at the F-F boundary. This change was manifest by a transition from stromatoporoid-, tabulate coral- and colonial rugose coral-dominated reefs to frameless mudmounds dominated by calcimicrobes and microbialites, relegated to deeper waters [Fagerstrom, 1994]. This trend continued into the Famennian, and only recovered in the Early Carboniferous, though the presence of Waulsortian

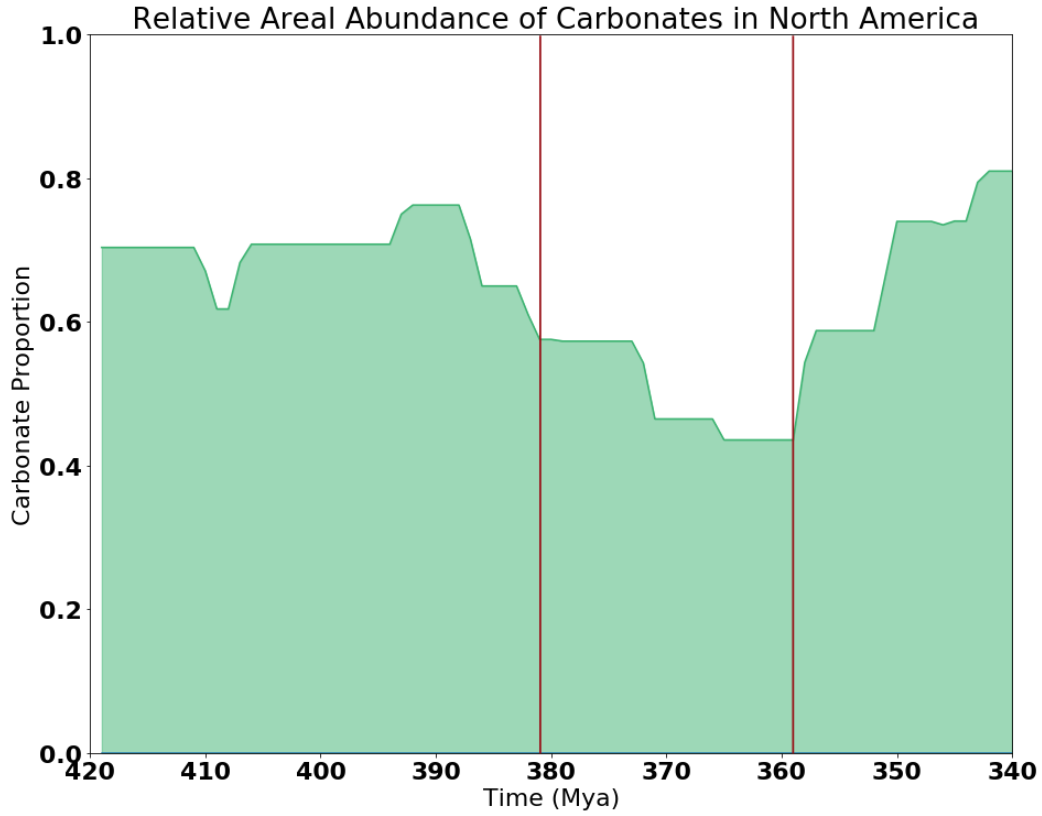

Figure 2.6: Relative areal abundance of carbonate deposition in preserved North American sedimentary rocks during the Devonian and Early Carboniferous. For reference, the Late Devonian Epoch, which includes the Famennian Stage, is from 382.8 to 358.9 Ma. In both this figure and Figure 2.4, there is a clear drop in carbonate deposition. Data is sourced from the Macrostrat database [Peters et al., 2018].

mudmounds in the Tournaisian imply that reef facies did not recover fully until the Visean [Lees, 1997].

The reasons for this carbonate crash remain contentious [Webb, 2002]. Extrinsic factors such as a shift in global tectonic plate motions could affect reef biodiversity and spatial distribution by changing available habitat area [Leprieur et al., 2016]. This could have occurred during the amalgamation of Pangea which would have altered ocean current systems [Copper, 1994, Webb, 1994]. Eustatic controls on the distribution of marine environments, particularly affecting the flooding or draining of epeiric seas, could have had a significant impact on the accommodation of carbonate buildups [Johnson et al., 1985, Webb, 2002, Haq and Schutter, 2008]. Indeed, the F-F boundary is marked by an overall marine transgression related to the Taghanic onlap intiated in the Middle Devonian coincident with the Acadian Orogeny [Johnson, 1970, Sandberg et al., 2002, Zambito et al., 2012] and an end-Famennian marine regression attributed to Southern Hemisphere glaciation [Caplan and Bustin, 1999, Sandberg et al., 2002]. In the event of rapid marine transgression, increasing accommodation may outpace the biotic production of carbonate leading to a "drowned" platform. In the event of a severe marine regression, accommodation is reduced relative to sediment supply. Carbonate platforms become exposed and subsequently eroded.

It has also been proposed that a transition from a Devonian "greenhouse" to Carboniferous "icehouse" climate conditions may have resulted in steeper latitudinal thermal gradients increasing thermohaline circulation and enhanced vertical mixing of ocean waters [Caplan and Bustin, 1999]. Consequently, the upwelling of nutrient-rich bottom waters onto the platform would have led to eutrophication suffocating reef communities and accumulating large deposits of organic-rich shales characteristic of the Hangenberg extinction [Caplan and Bustin, 1999, Murphy et al., 2000, Perkins et al., 2008]. Alternatively, increased nutrient runoff resulting from the development of continental forests may have inhibited carbonate production by increasing turbidity, and ultimately replacing oligotrophic marine environments with eutrophic ones [Hallock and Schlager, 1986, Wood, 1993, Algeo et al., 1995, Dahl and Arens, 2020]. Finally, a proposed change in ocean water chemistry whereby a change in the Mg/Ca ratio of seawater driven by seafloor spreading rates could have had an effect on

calcifying organism turnover. According to this hypothesis, high levels of ocean crust production results in a drawdown of Mg^{2+} and release of Ca^{2+} via hydrothermal alteration, thereby lowering the Mg/Ca ratio of seawater (and vice versa during periods of low rates of seafloor spreading). A rise in Mg/Ca ratio could have disfavoured the low Mg "calcite sea" biomineralizers that dominated the Devonian oceans, causing a transition to the high-Mg "aragonite sea" organisms observed in the Early Carboniferous [Stanley and Hardie, 1998, Stanley and Hardie, 1999].

Regardless of the collapse of shelf carbonates, mass balance dictates that the output of carbonate burial must equal the input of alkalinity on geologic timescales. Therefore, if carbonate burial by Devonian reefs or other platformal systems was to decrease, then the balance must be taken up by another sink, such as authigenic carbonate precipitation. Theoretically, this state could have been promoted either by the suppression of carbonate saturation gradients as a result of anoxic respiration [Higgins et al., 2009], or by the upwelling of waters with elevated alkalinity [Grotzinger and Knoll, 1995]. Regardless, evidence suggests that this particular time interval, defined by global anoxia, biotic turnover and a shift from carbonate to marine siliciclastic depositional regimes, implies boundary conditions conducive to an authigenic sink as an important component to the global carbon cycle.

2.3 Geological Setting

2.3.1 Upper Devonian Stratigraphy and Tectonic History of the Western Canada Sedimentary Basin

Upper Devonian strata is well preserved throughout western Canada, where it forms part of the Western Canada Sedimentary Basin (WCSB), spanning an areal extent of 100,000's of km^2. Famennian formations, which include both platformal carbonates and their basinal equivalents, are found in the subsurface of Alberta and BC, and also outcrop within the Front Ranges of the Rocky Mountains. Geochemical work on these formations, specifically the response to shelf carbonate crash as recorded in carbon isotope values and shale geochemistry, has thus far been lacking. Accordingly, this location provides an appropriate target for evaluating controls on Late Devonian DIC carbon isotopic composition.

Strata within the WCSB were deposited on the northwest margin of Laurentia forming a supracrustal sedimentary wedge prograding westward, and ranges from Early Paleozoic to Paleocene in age. During the Late Devonian, the WCSB was located within equatorial latitudes [Mac Niocaill and Smethurst, 1994] (Figure 2.5). At this time, an expansive epeiric sea hosted a prominent carbonate factory on a passive margin [Halbertsma et al., 1994, Peterhänsel et al., 2008]. This carbonate platform developed along a westward-prograding continental terrace wedge delimited by the Cordilleran miogeocline at its western edge, later evolving into a foreland basin potentially initiated by the outboard Antler Orogeny in the southwest [Smith et al., 1993, Root, 2001] or by westward propagation of a subduction zone along the western margin of Laurentia resulting from collisonal tectonics between Gondwana and Laurentia-Baltica [Colpron and Nelson, 2009]. A regional depression associated with Late Paleozoic tectonics is referred to as the Prophet Trough [Richards et al., 1994]. This structural deformation is thought to be linked to the Antler magmatic arc and igneous activity of the Kootenay terrane [Speed and Sleep, 1982].

In-board from the Prophet Trough, lies the Peace River Arch (PRA), which was a paleotopographic high during much of the Paleozoic. The PRA was progressively onlapped by Cambrian to Upper Devonian carbonates, evaporites and clastics [O'Connell et al., 1990]. By Famennian time, the PRA had experienced near complete inundation and was overlain by carbonates representing the Wabamun Group, with marine transgression being a result of increased basinal subsidence of the passive margin potentially initiated by regional tectonic stresses [Dix, 1990] or through tectonic eustacy [Johnson et al., 1985]. During the Late Devonian episodic siliciclastic infill, represented by Frasnian-Famennian Sassenach, Graminia Silt and Trout River formations, originated from northern sources [Hauck et al., 2017]. Intermittent compressionary tectonic activity during the late Jurassic to early Eocene led to the accretion of allochthonous exotic terranes resulting in the earlier deposited passive margin sediments to be detached from the crystalline basement, forming a series of imbricate thrust sheets. These thrust sheets would become known as the Rocky Mountain Foreland Thrust and Fold Belt [Pană and van der Pluijm, 2015]. Today, portions of Late Devonian strata outcrop among these thrust sheets in the Rocky Mountain Front Ranges.

Famennian stratigraphy within the basin is dominated by the Wabamun Group carbonates and its equivalents (Figure 2.7), with carbonate lithologies thickening basinward (towards the present-day northwest). Shale and argillaceous limestones are present at the basin margin in the northwest, platform limestone facies are found in north-central Alberta, and become progressively dolomitic and evaporitic towards the southwest (Figure 2.8). Regional stratigraphy broadly conforms to an epeiric shelf depositional model. In Alberta's subsurface, the Wabamun Group comprises the peritidal carbonates and evaporites of the Stettler Formation and, and open-marine carbonates of the Big Valley Formation. In the Rocky Mountain Front Ranges, the lower peritidal to subtidal Palliser Formation is coeval to the Wabamun, and overlies the mixed carbonate-clastic Sassenach Formation [Meijer-Drees et al., 1993, Peterhänsel et al., 2008]. In the deep basin, the Famennian consists entirely of marine shales of the Besa River Formation [Ferri et al., 2011]. The basin slope includes shales from the Fort Simpson Formation and open marine carbonates of the Tetcho and Kotcho formations. Towards the end of the Famennian, increased accommodation combined with a nutrient-stressed carbonate system resulted in the drowning of the platform [Caplan and Bustin, 1999, Richards et al., 2002, Peterhänsel et al., 2008]. This event is marked by the widespread deposition of the organic rich Exshaw Formation black shales, which covered the entirety of the WCSB and spans the Devonian-Carboniferous boundary [Savoy et al., 1999]. The Exshaw itself is divided into two members: lhe lower member, Famennian in age, comprises laminated shale, and the upper member is a silty to sandy carbonate that is Tournaisian in age [Smith and Bustin, 2000].

2.4 Purpose

The work presented herein attempts to address the authigenic carbonate sink hypothesis. This entails a compilation of δ^{13}C profiles of Famennian formations across the WCSB to assess the carbon isotope response (recorded in marine carbonates) to shelf carbonate collapse. Target formations (specifically: Palliser, Sassenach, Wabamun Grp., Besa River) were chosen because they lack high-resolution stable isotope data. Based on the reduction of carbonate facies in the Upper Devonian and the widespread deposition of black shales formations, it is predicted that a greater proportion of carbon is being sequestered as low δ^{13}C authigenic carbonate which may

have affected the isotopic mass balance of the carbon cycle. Owing to both increased organic carbon burial and authigenic carbonate burial, high δ^{13}C values are expected in the platformal carbonates, and low carbon isotope values in carbonate are expected in the basinal black shale formations. Furthermore, I aim to quantify the amount of carbonate precipitation within basinal sediments. A strong authigenic sink necessitates the precipitation of carbonates with low δ^{13}C values on or near the seafloor during early diagenesis in large volumes. Through the construction of well constrained stratigraphic and geochemical records, the merit of the authigenic sink hypothesis will be tested.

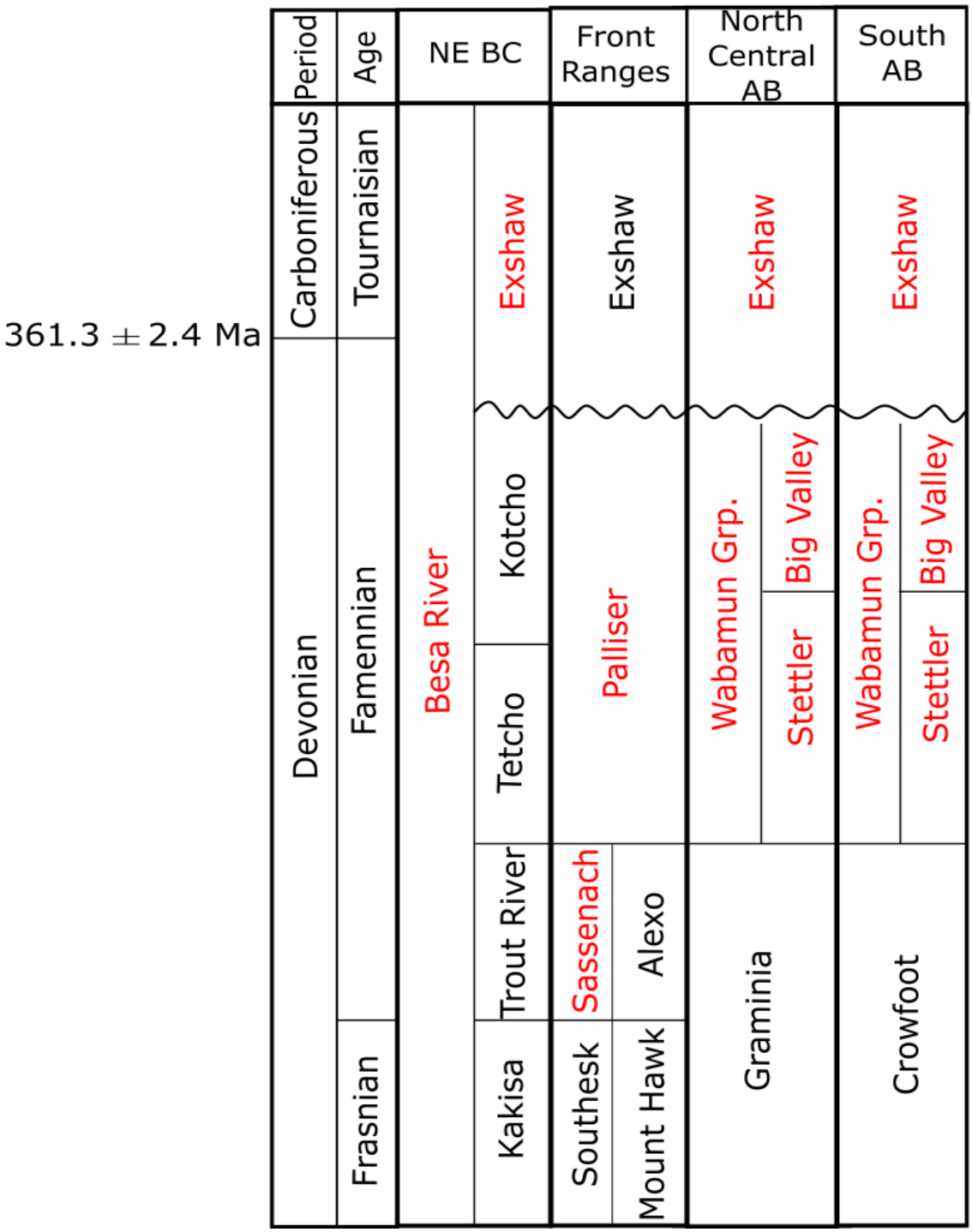

Figure 2.7: Late Devonian – Early Carboniferous stratigraphy of the WCSB. Stratigraphic nomenclature compiled from [deWitt and McLaren, 1950, McLaren and Mountjoy, 1962, Macqueen and Sandberg, 1970, Richards and Higgins, 1988, Meijer-Drees et al. 1993]. Red highlighted formations represent formations that were sampled for this study. Re-Os age date for the Devonian-Carboniferous boundary was measured from field samples taken at Jura Creek, AB, [Selby and Creaser, 2005]. The lower member of the Alexo Formation is partly equivalent to the Southesk and Mount Hawk formations [Workum and Hedinger, 1992]

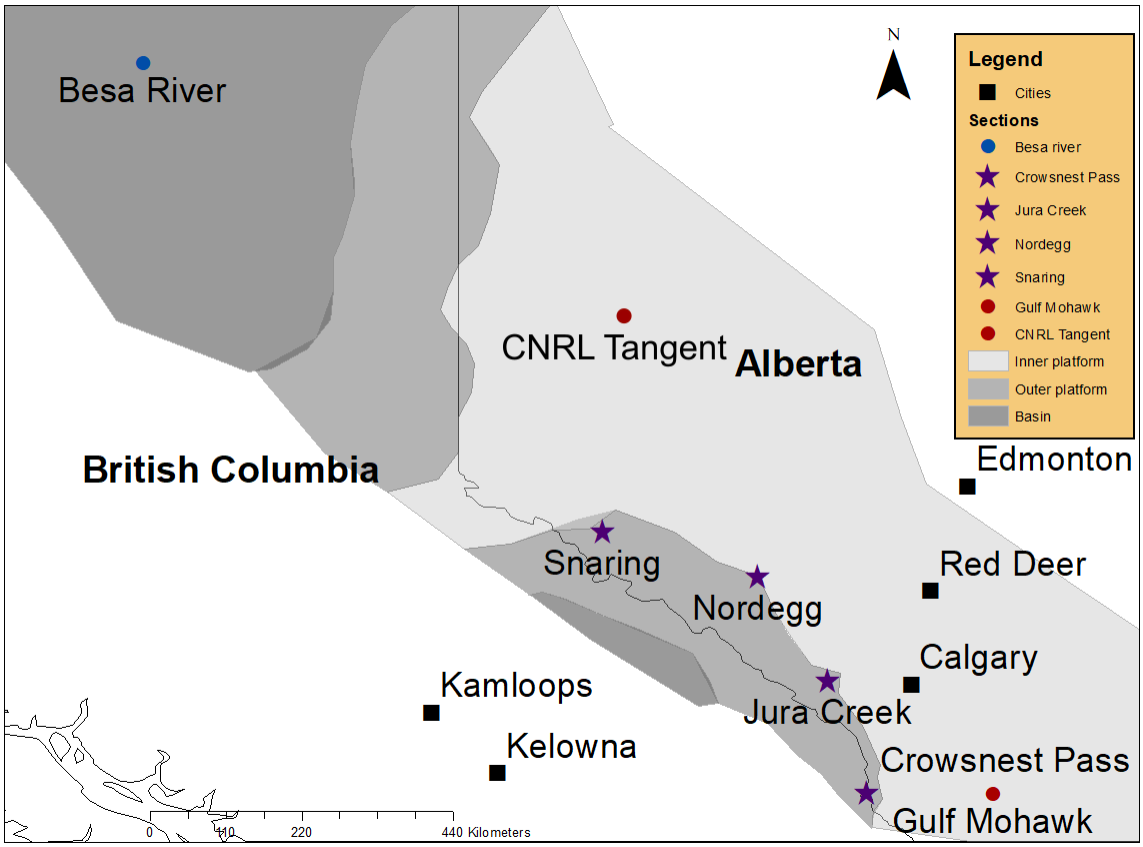

Figure 2.8: Simplified lithofacies distribution across the WCSB during the Famennian (modified from [Peterhänsel et al., 2008]). Stars indicate outcrop study locations. Circles indicate core study locations. Each symbol is colour coded to reflect its relative depositional environment within the WCSB. Blue, attributed to the deep basin; Purple, attributed to the outer platform; and Red, attributed to the inner platform.

Chapter 3

Materials and Methods

Seven stratigraphic sections were measured for this study, representing a range of depositional environments across several hundred square kilometers. Four outcrop sections were logged in the southern Canadian Rockies: Snaring (53°03'36"N, 118°05'57"W), Nordegg (52°29'36"N, 116°00'15"W), Jura Creek (51°05'42"N, 115°09'11"W) and Crowsnest Pass (49°37'36"N, 114°38'48"W). Three core sections were logged: A-38-B/94-N-8 Besa River, 09-23-80-24W5 CNRL Tangent and 11-36-7-23W4 Gulf Mohawk, whose geographic location represented northeast British Colombia, north-central Alberta and southeast Alberta, respectively, forming a NW-SE transect roughly 1275 km long (Figure 2.8). At each locality, the physical stratigraphy was described and lithofacies were correlated to respective formations within the WCSB. Representative samples of each lithofacies were prepared for thin-section petrography. Using standard transmitted microscopy, lithofacies were classified following Dunham's classification system [Dunham, 1962] and mudstone lithofacies were classified using Potter's classification system [Potter et al., 2012].

During lithostratigraphic logging, samples of carbonate were sampled for $\delta^{13}C$ and $\delta^{18}O$ analyses. Sampling resolution was at 1 meter intervals, or at finer resolution for thinner sections and on either side of prominent lithologic boundaries. At the University of Victoria, a Dremel drill press was used to extract approximately 10 mg of powder from the finest-grained component of each sample, most often micrite. For sections 09-23-80-24W5 CNRL Tangent and 11-36-7-23W4 Gulf Mohawk, a Dremel rotary drill with a tungsten carbide cutter bit was used for collecting powder done on site at the Alberta Energy Regulator's Core Research Facility in Calgary. Prior to sampling, the external surface of the core was abraded away to minimize

the risk of contamination.

A total of 750 rock powders were taken for stable isotope analysis, 54 shale/siltstone and 696 carbonate. Powders were left to dry in an oven for at least 6 hours at 90°C. Samples were weighed into a glass exetainer, capped and then flushed with helium. Samples were then reacted with 15 drops of anhydrous phosphoric acid from a 1 ml syringe. Samples were left to react for 1 hour at 85°C, and CO_2 in the head space was sampled via an auto-sampler and analyzed on a Sercon 20-22 continuous flow isotope ratio mass spectrometer (IRMS) with a Gasbox II front end device at the University of Victoria. All carbon and oxygen isotope ratios are reported as per mil (‰) values relative to VPDB (Vienna Pee Dee Belemnite) standard. Analytical uncertainty (1σ) is 0.05 to 0.1‰ for δ^{13}C and 0.15 to 0.2‰ for δ^{18}O, based upon replicate measurements of two secondary calcite standards (internationally recognized IAEA-CO-8 and in-house standard VTS) (Figure 3.1). Every five unknowns is bracked by measurements of these two standards, as well as a third standard (IAEA-603) used for beam drift correction. Drift refers to deviation from an expected isotopic ratio of a reference standard (in this case, IAEA-603). To compensate for this drift and to better constrain measurement accuracy, measured isotopic ratios of a primary standard are corrected to true values, and the bracketed secondary standards and unknowns are similarly corrected. After drift correction, ratios are converted into delta-values according to the following equation:

$$\delta^{13}C = (R_{samp}/R_{stnd} - 1) \times 1000, \tag{3.1}$$

where R_{stnd} is the VPDB standard. All sample measurements are further normalized using the two-point normalization method [Paul et al., 2007]. A linear regression line is fitted between two reference standards (IAEA-603 and IAEA-CO8). The two-point corrected δ^{13}C of the sample is then calculated according to the following equation:

$$\delta^{T}_{sample} = \frac{\delta^{T}_{CO8} - \delta^{T}_{603}}{\delta^{M}_{CO8} - \delta^{M}_{603}} \times (\delta^{M}_{sample} - \delta^{M}_{CO8}) + \delta^{T}_{CO8} \tag{3.2}$$

where (T) refers to true value and (M) refers to measured value. This procedure is repeated for δ^{18}O. After two-point correction, the in-house standard remains as a secondary standard for monitoring of accuracy and precision (Figure 3.1).

Powders from 21 shale horizons (out of 54 shale samples total) were measured for their carbonate content (wt% $CaCO_3$). This was done using a UIC Inc. carbon coulometer with a CM5130 acidification module at the University of Victoria. Between 40 to 70 mg of shale powder was produced, using a rock pulveriser, and was weighed out into vials. A 3 minute purge time was used to clear atmospheric CO_2 from the sample vial prior to acid injection. Powder was then reacted with 6.5 ml of 2N H_2SO_4. Coulometric titration is an analytical chemistry technique that is often used to determine the concentration of a chemical species by applying an electrical current to a solution. In this analysis, reaction with sulfuric acid serves to evolve the CO_2 gas from the sample, which is then swept into the coulometer cell. The carbon dioxide gas is absorbed into an ethanolamine solution. The resulting weak acid is then titrated by a strong base through the use of an electric current which drives the chemical reaction. The electrical current (measured in coulombs) that is required to reach the equivalence point (i.e. the point in which the amount of moles of acid is balanced by the amount of moles of base mixed into the solution) is proportional to the amount of dissolved carbon dioxide in the sample. The carbon dioxide gas originates from inorganic carbon that is held within carbonate minerals in the shale sample. Analysis of each sample was done over 13 minutes with a frequency of 1 reading per minute. Three "in-house" standards representing a mixture of pure silica sand and pure calcium carbonate at ratios of 90:10, 99:1 and 100:0, were used to calibrate the instrument. Because all 21 of these samples also were measured for $\delta^{13}C$, coulemetry-determined inorganic carbon content was then plotted with respect to IRMS beam area (a function of the amount of CO_2 generated during phosphoric acid digestion and the signal measured on the Faraday cups). Inorganic carbon content was then converted to wt% calcium carbonate via the stoichiometry of calcite. A linear fit curve allowed carbonate content for the remaining 33 shale samples to be then estimated, since all shale samples were measured on the IRMS (Figure 3.2).

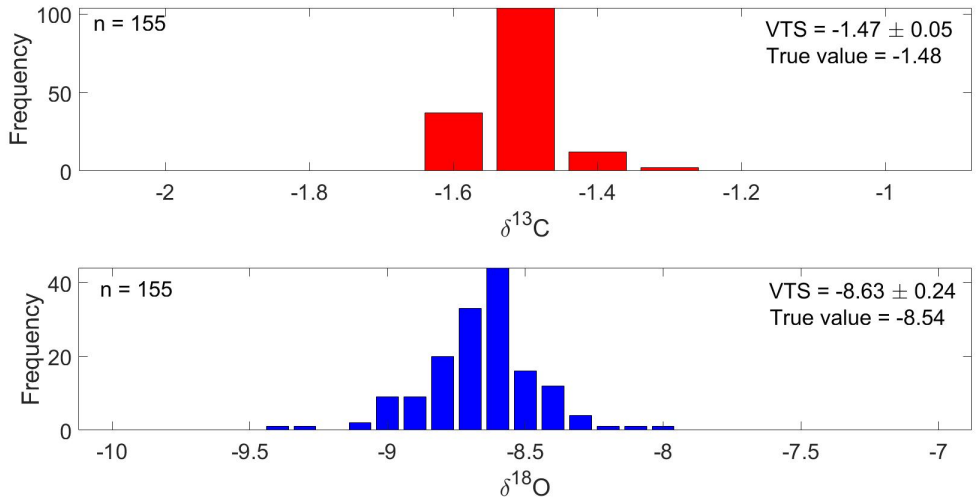

Figure 3.1: Histogram of in-house standard VTS (two-point corrected) measured in analytical sessions along with the 750 samples analyzed for this study.

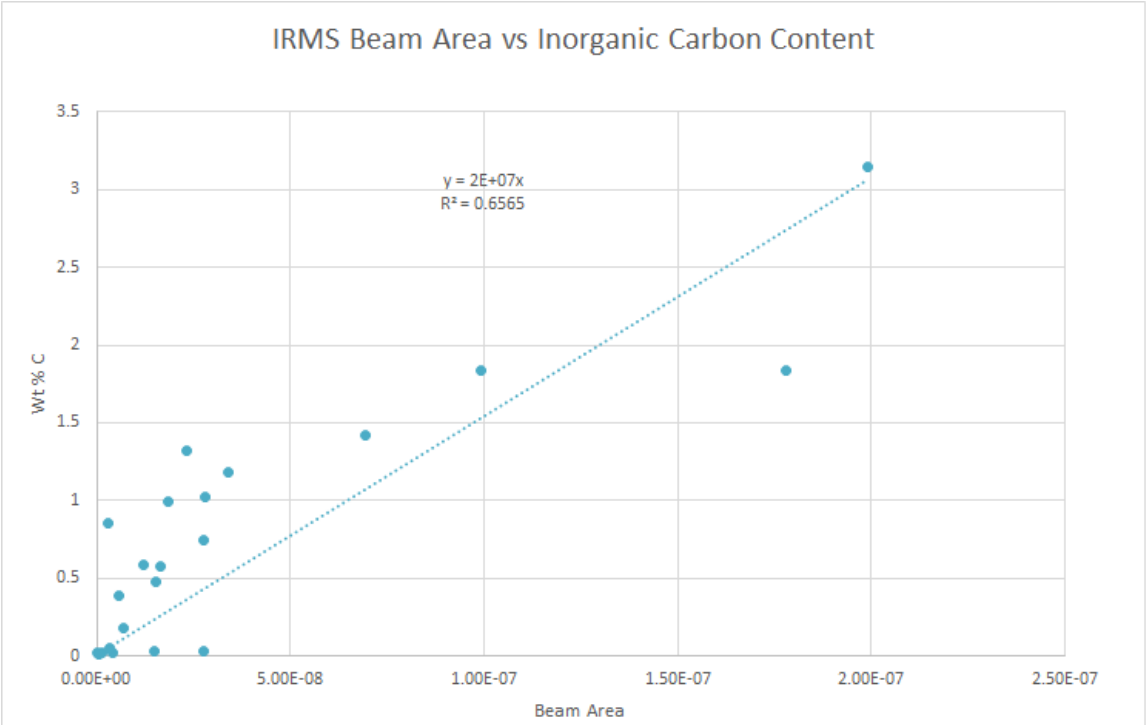

Figure 3.2: Plot of IRMS beam area as a function of coulometry-determined $wt\%$ inorganic carbon for 21 shale samples. The data are correlated from which a linear fit was made. This linear equation was then used to semi-quantitatively estimate the calcium carbonate content for the samples not measured via coulometry.

Chapter 4

Results

4.1 Lithofacies

The following is a summary of the lithofacies found in the examined Famennian formations of the WCSB. Facies are identified from field and petrographic observations and are based on lithology, grain size, fossil content, and sedimentary structures. Limestone lithologies have been described using Dunham's classification scheme [Dunham, 1962], dolostone lithologies have been described using Sibley and Gregg's classification scheme [Sibley and Gregg, 1987] and mudstone lithologies have been described using Potter's classification scheme [Potter et al., 2012]. I start with descriptions of facies representing the deep basinal environment, followed by the outer carbonate platform and finally the inner platform. Select facies characteristics are sometimes illustrated in figures. Figures that display thin section images are specified, in caption, whether they were taken in plain polarized light (PPL) or cross-polarized light (XPL). All facies are summarized in Table 4.1 (p. 43).

4.1.1 Basin

Lithofacies attributed to the deep basin depositional environment were sampled and studied from three separate cores: A-38-B/94-N-08 Besa River, 9-23-80-24 CNRL Tangent and 11-36-7-23W4 Gulf Mohawk. The two main formations representing the deep basin environment are the Besa River and the Exshaw formations. The identification of lithology was based on grain size, mineralogy and sedimentary textures. Lithofacies of the deep basin are characterised as fine-grained siliciclactics (shales and siltstones) hosting localized carbonate and pyrite. Carbonate minerals take the

(a)

(b)

(c)

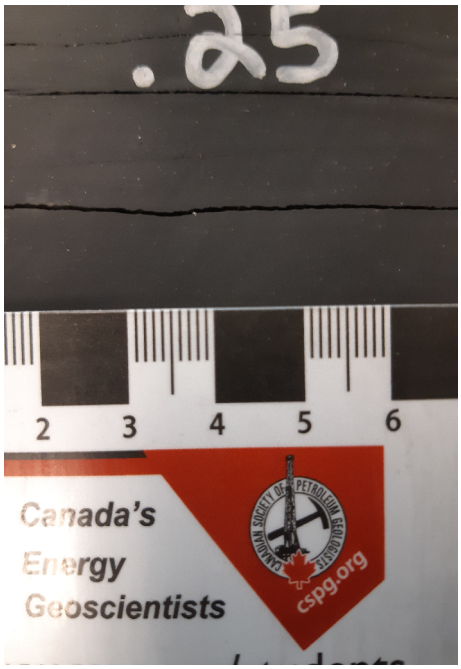

(d)

Figure 4.1: a: Laminated calcareous siltsone (B1), b: Pyrite aggregate, c: Pyrite lense, d: Unlaminated massive siltstone (B2). All images taken from the Besa River core section, which represents the deep basin depositional environment.

(a)

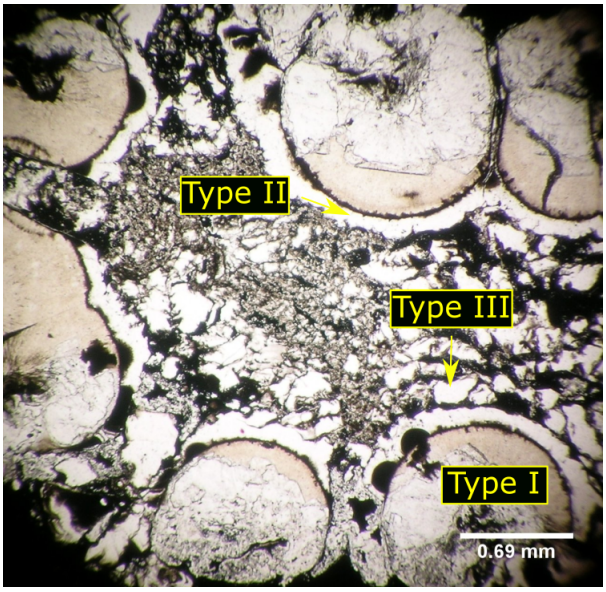

(b)

(c)

Figure 4.2: a: Carbonate concretion (B3) within Exshaw Formation, core A-38-B/94-N-08 Besa River, b: microscopic view (PPL) of the same concretion displaying three generations of cement. Type I = botryoidal cement, Type II = elongated fringe cement, Type III = blocky cement, c: Macroscopic carbonate concretion (B3) within the Exshaw Formation at Jura Creek, Alberta. This basinal facies overlies limestones of the Palliser Formation.

form as discrete laminations, concretions or are finely disseminated within the rock. Pyrite takes the form of lenses, aggregates and, occasionally, display a fromboidal morphology.

Besa River Formation

Facies are identified and described from core A-38-B/94-N-08 Besa River (Figure 2.8).

B1: Laminated calcareous siltstone This lithofacies consists of indurated, black (dark grey when weathered) siltstone with faint parallel laminations inferred to be composed of carbonate minerals based on effervescence. Individual minerals are too small for positive identification with a petrographic microscope. Minor occurrence of pyrite is observed either as disseminated grains or as isolated lenses (Fig. 4.1 a,b,c).

B2: Massive siltstone This lithofacies consists of a homogeneous, massive indurated black (dark grey when weathered) siltstone (Fig. 4.1 d). Minor occurrence of pyrite is observed either as disseminated grains or as isolated lenses. At sections Gulf Mohawk and CNRL Tangent (Figure 2.8), this lithofacies has a distinct brown colour and petroleum smell.

Exshaw Formation

The same lithologies are observed in the Exshaw Formation as in the Besa River. However, mudrocks from the Exshaw Formation do display a more pronounced fissility, and thus are referred to as shales. Pyrite content is higher relative to the Besa River Formation, including the presence of pyrite framboids.

B3: Carbonate Concretion Several carbonate concretions are observed within the Exshaw formation (Fig. 4.2 a, b). In core A-38-B/94-N-08 a lone concretion is observed (1.5 cm wide) and displays three distinct generations of carbonate cement (Figure 4.2 c). The first is characterized by botryoidal calcite (botryoidal texture is a mineral habit resembling a rounded cluster of grains); the second is characterized by elongated calcite cement fringing the calcite botryoids, and the final generation of cement is characterised by anhedral blocky cement filling the void spaces between botryoids. At Crowsnest Pass and Jura Creek, large macroscopic concretions were observed; however, the Exshaw Formation at these locations were not logged.

4.1.2 Outer Platform

Lithofacies that comprise the outer carbonate platform depositional environment are from the Sassenach and the Palliser formations. The Sassenach underlies the Palliser Formation and is confined to the Jasper sub-basin. In the Sassenach Formation, lithofacies have been identified from one field section (Snaring), while parts of the Palliser Formation were sampled from Snaring, Jura Creek, Nordegg and Crowsnest Pass field sections (Figure 2.8). Lithofacies were determined primarily by grain size and sedimentary textures.

Generally, depositional characteristics within the outer carbonate platform are heterogenous. The Sassenach is defined by subtidal limestones at its base, and an upper section defined by cyclical deposition of silty carbonates and fine-grained siliciclastics characteristic of a slope deposition which represents a transition from the deep basin to the carbonate platform. Factors controlling sediment deposition include storm activity, episodic siliciclastic influx and mass wasting.

The Palliser Formation is defined by alternating subtidal to lower peritidal sediment deposition. Depositional patterns are dominated by alterations between lime mudstone to packestone lithologies. Subtidal limestones are described as peloidal mudstones and wackestones with varying fossil content and occasional burrows. Peritidal limestones are characterised by peloidal wackestones and packestones. Unique features include stromatoporoid fossils, fenestrae and laminated microbialites. Similar to the Sassenach Formation, storms are a dominant depositional process within the Palliser. Dolostones occur sporadically and are a result of secondary processes throughout the Palliser Formation.

OP1: Skeletal - peloidal lime mudstone and wackestone These limestones are dark brown or grey and display no observable sedimentary structures. Allochems are predominantly comprised of peloids (grain size $\approx$ 0.05 mm to 0.1 mm) and peloid aggregates with trace amounts of fragmented gastropods, brachiopods and crinoids. Lime mudstone intraclasts (0.3 to 0.8 mm) are visible within the wackestones. Matrix composition is a mix of micrite (i.e. carbonate mud) and microspar with occasional coarse calcite crystals. Dissolution seams (Figure 4.3 a) and secondary calcite veining crosscut the rocks. Trace iron oxide alteration is observed in thin section. At Jura

Creek at one stratigraphic horizon, this facies incorporates a laminated microbialite (Figure 4.4). At Nordegg, a 15 m stratigraphic interval of this lithofacies is highly dolomitized, yet still retains its original fabric.

OP2: Laminated peloidal lime mudstone This lithofacies is medium to light grey coloured with wispy tan laminations. Allochems are composed of peloids and peloid aggregates (Figure 4.3 b). Bioclastic material is mainly composed of gastropods and other fragmented fossils too small to be identified. Matrix is composed of microspar; however, laminations appear to be defined by a greater abundance of micrite.

OP3: Bioturbated lime mudstone This lithofacies is similar to OP2, but matrix is more micritic in composition. Pervasive burrow mottling is identified in outcrop (Figure 4.5). In certain outcrop locations, limestone has a nodular shaped texture.

OP4: Slumped siliciclastic-carbonate This lithofacies consists of interbeds (3 to 6 cm) of calcareous siltstone and mudstone/wackestone. They contain dolomitized sandstone lenses and slump structures (Figure 4.6).

OP5: Siltstone-mudstone rhythmite This lithofacies is defined by successive units of alternating calcareous siltstone and lime mudstone beds (1 to 1.5 m thick). Beds are observed to be wavy parallel, with decreasing lamina thickness upward (from $\approx$ 30 cm at the base to $\approx$ 3 cm at top of a single bed. Silty beds display starved ripples, rip-up clasts and prominent crossbedding (Figure 4.7 a, b, c). In outcrop, differential weathering is evident between the siltstone and mudstone beds.

OP6: Siltstone with limestone nodules This lithofacies is defined by massive brown-grey siltstone with irregular nodules of lime mudstone (2 to 3 cm in diameter).

OP7: Massive Calcareous Siltstone This lithofacies consists of a light brown siltstone composed predominantly of quartz grains surrounded by a calcareous cement. Grain size may vary between very fine sand to silt. Some quartz grains (0.05 mm) display cloudy interiors in transmitted light. Pore spaces are pervasive throughout the sample (0.15 - 0.4 mm) as well as trace amounts of iron oxide weathering. Calcite veins can be found to crosscut the unit.

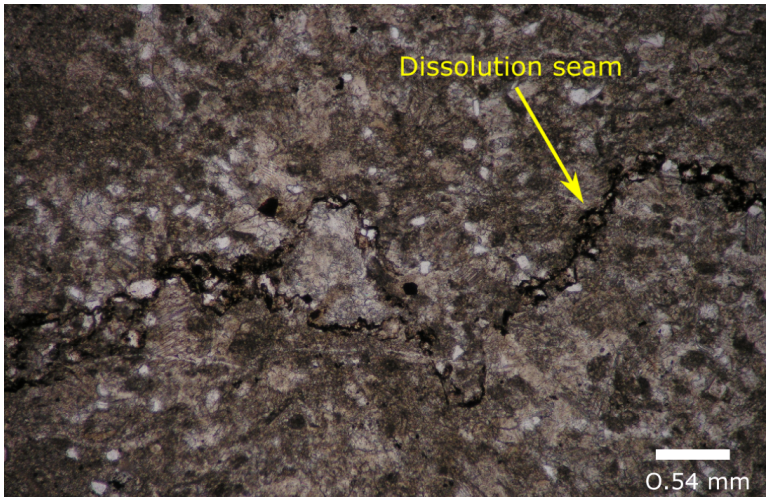

(a)

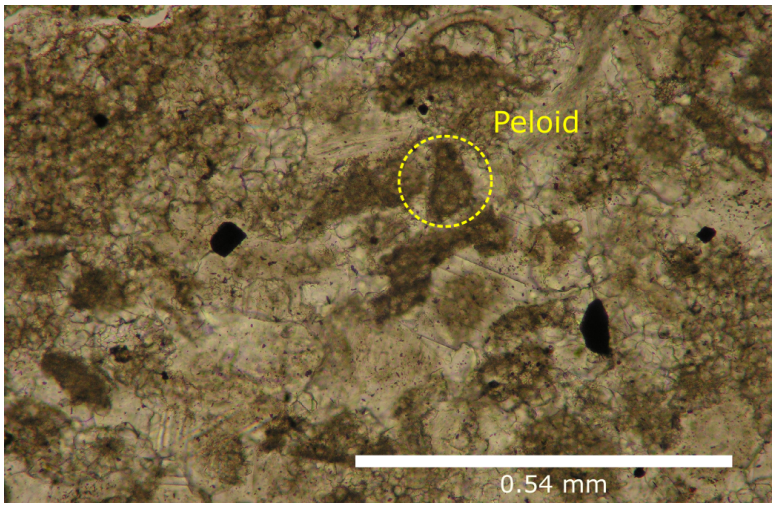

(b)

Figure 4.3: a: Pressure dissolution seams in lithofacies OP1, image in XPL. b: Peloids and peloid aggregates within a microspar matrix. Image in PPL for lithofacies OP2. Both images (a and b) represent facies from the outer platform environment and were sampled from the lower Sassenach Formation at the Snaring field section.

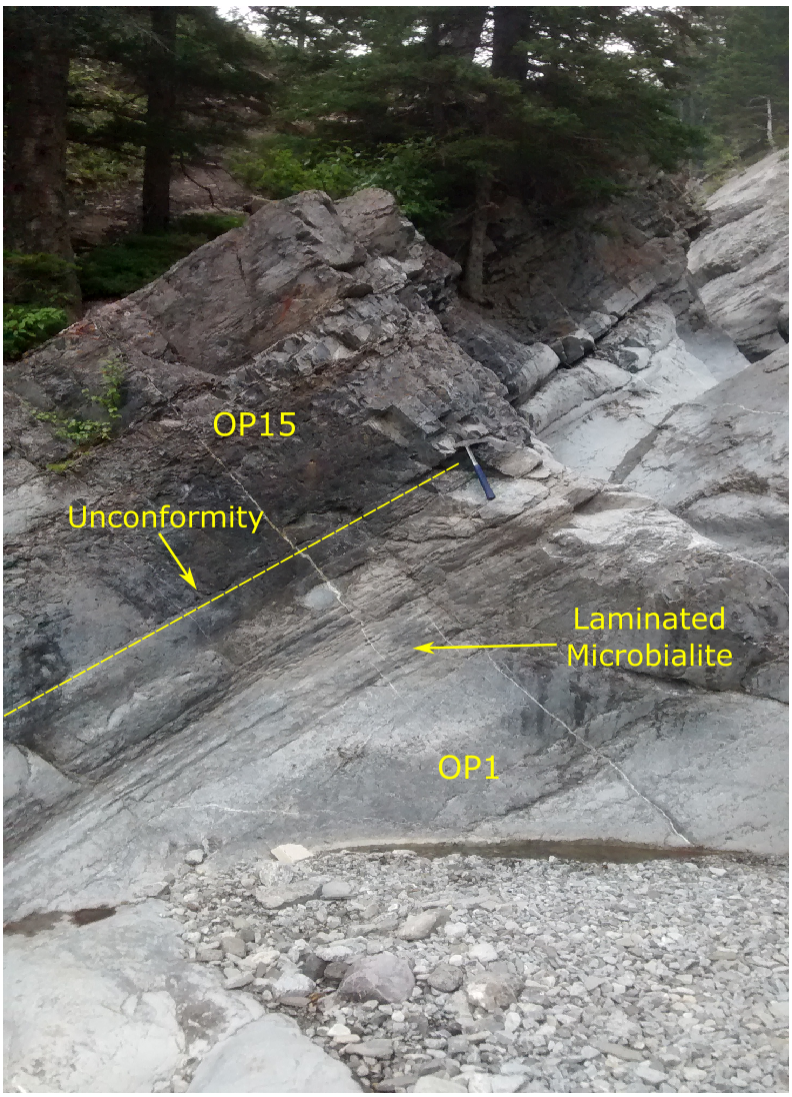

Figure 4.4: Upper part of the Costigan Member of the Palliser Formation underlying the Exshaw Formation. Within it contains the contact between lithofacies OP1 and OP15 at the topmost Jura Creek section. The contact is defined by a centimeter-scale laterally extensive undulatory erosional surface (i.e. an unconformity) [Richards and Higgins, 1988, Meijer-Drees et al., 1993, Peterhänsel et al., 2008]. Laminated microbialite is visible in outcrop within facies OP1.

Figure 4.5: Burrow mottling structure within lithofacies OP3 of the Palliser Formation at Jura Creek section. This facies is representative of the outer carbonate platform.

Figure 4.6: Soft sediment deformation within lithofacies OP4 of the Sassenach Formation representing the platform slope environment. Picture taken at the Snaring field location in Alberta.

(a)

(b)

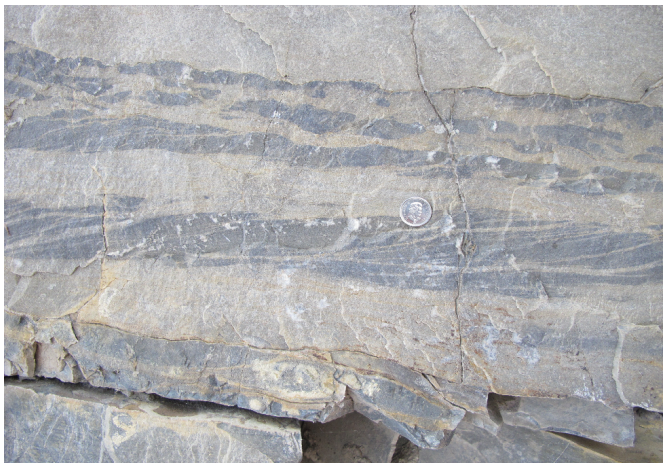

(c)

Figure 4.7: a: Lithofacies OP5 displaying thinning upwards rhythmic layering of limestone and siltstone beds. Differential layering clearly distinguishes the more resistant siltstone beds from the lime mudstone. b: Starved ripple texture observed within lithofacies OP5 c: Limestone crossbeds observed within lithofacies OP5. All photos were taken from the Snaring field location and represent facies characteristics of the outer platform environment within the Sassenach Formation. (Coin diameter = 23.81mm)

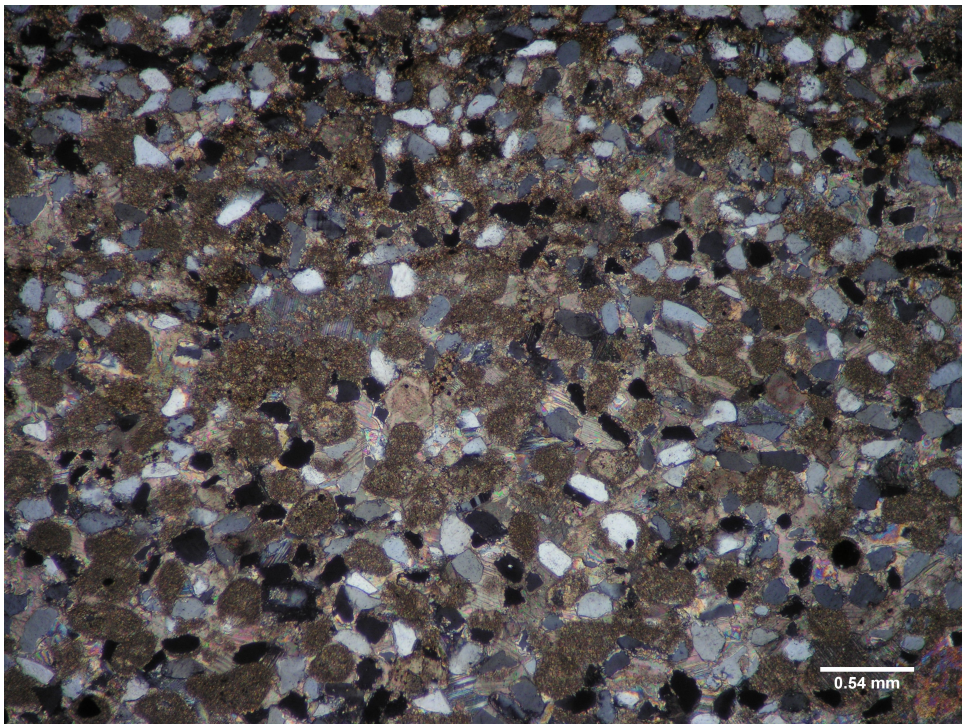

Figure 4.8: XPL image of lithofacies OP8 from the Sassenach Formation at Snaring section. Grey sub-rounded to sub-angular quartz grains are surrounded by a fine peloid-bearing carbonate matrix.

Figure 4.9: Outcrop image of lithofacies OP8 (from an outer platform environment) displaying banded layers of brown and dark brown silt. Picture of the Sassenach Formation taken at the Snaring study area.

OP8: Ribbon Rock This lithofacies consists of light brown to brown-grey massive calcareous siltstone. Grains are composed of disseminated subangular to subrounded, well sorted quartz (0.07 mm) (Figure 4.8). Certain samples contain pockets of interlocking quartz grains with oblong to convex grain contacts most likely originating from compaction. Matrix abundance is variable and is predominantly composed of microspar. Where carbonate cement is abundant, peloids are also visible. In outcrop, this facies is distinguished by buff grey coloured calcareous siltstone which is intersected by thin brown beds (1 cm thick), given the resemblance of "ribbons"(Figure 4.9). In thin section, layering is distinguished by the proportion of calcareous cement, with darker mud-rich beds containing more microspar cement than the light brown siltier beds.

OP9: Silty lime mudstone This peloid-bearing lime mudstone is similar to OP1; however, no skeletal material visible in hand specimen. Limestone is platy with ubiquitous silt partings.

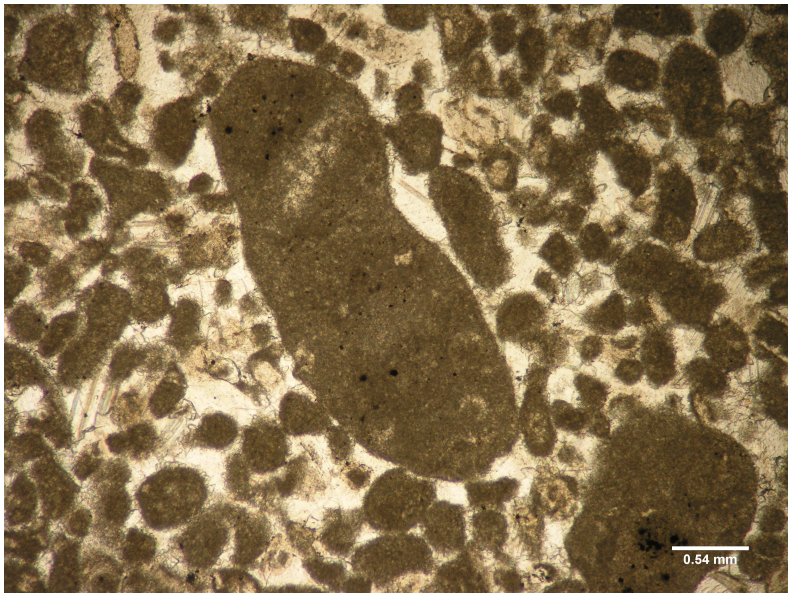

Figure 4.10: Plain polarized light image of lithofacies OP10 showing a biomicrite rip-up clast within a spar calcite matrix. Sample of the Palliser Formation taken from Jura Creek section from an outer carbonate platform environment.

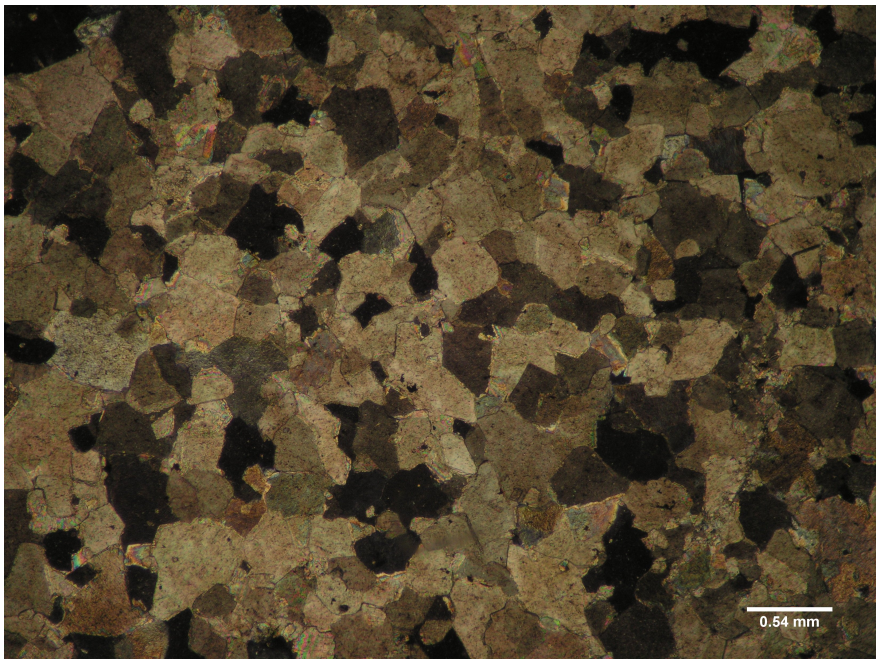

Figure 4.11: Interlocking, curved anhedral dolomite rhombs within lithofacies OP12. Sample of the lower Palliser Formation, taken from the Jura Creek section from an outer carbonate platform environment. Image taken in cross-polarized light (XPL).

OP10: Skeletal packestone This lithofacies consists of dark to medium grey limestone with allochems that are composed predominantly of bioclastic material, such as crinoid ossicles, brachiopods, gastropods and bryozoans. This lithofacies also includes peloids (0.1 mm) and intraclasts/rip-up clasts (0.1 to 0.6 mm) composed of biomicrite (i.e. skeletal mudstone) (Figure 4.10). Matrix is composed of sparry calcite with trace amounts of micrite. Stylolites also occur throughout this lithofacies.

OP11: Bioturbated packestone This lithofacies is similar to OP10, but displays pervasive burrows.

OP12: Massive dolostone This lithofacies consists of massive, light grey to brown carbonate rock dominated by interlocking anhedral dolomite rhombs (0.05 to 0.3 mm)(Figure 4.11). Dolomite has a nonplanar fabric and displays undulatory extinction in cross polarized light with no visible inter-crystal porosity.

OP13: Bioturbated wackestone This lithofacies is similar to OP1, however it includes pervasive burrows. At the Crowsnest Pass section, fenestrae (lens-shaped

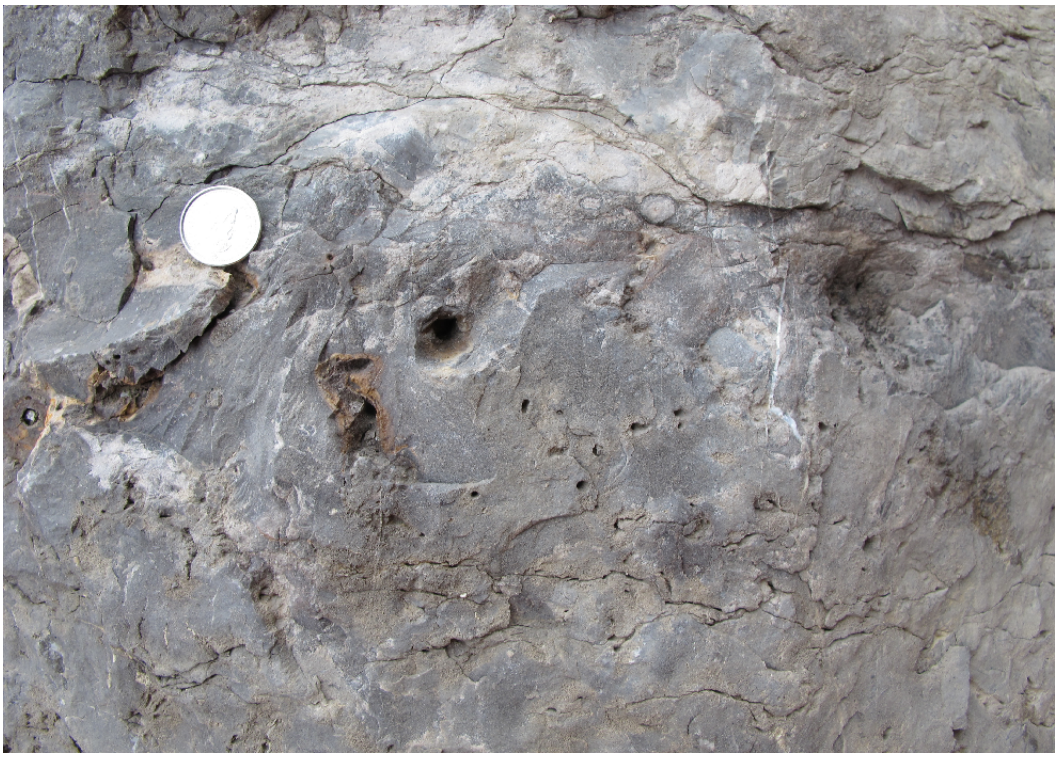

(a)

(b)

Figure 4.12: a: Fenestrae within lithofacies OP13. b: Laminated microbialite within lithofacies OP13. Both pictures taken at the Crowsnest Pass field section and represent facies from an outer carbonate platform environment. (Coin diameter = 23.81mm)

Figure 4.13: Encrusting stromatoporoids displaying domal mamelons within lithofacies OP14. Outcrop image taken at Jura Creek section. This lithofacies is part of an outer carbonate platform. (Coin diameter = 23.81mm)

pores that are larger than the normal intergranular spaces) and microbialite fabric is observed in outcrop (Figure 4.12 a, b).

OP14: Laminated wackestone/packestone with stromatoporoids This limestone facies is composed of allochems made up of peloids and bioclasts. Bioclastic material includes bivalves, crinoids, gastropods and bryozoans. Matrix composition is a mix of micrite and microspar. Low-relief domal stromatoporoids are visible as independent patches at centimetre scale in outcrop setting (Figure 4.13).

OP15: Cherty skeletal lime mudstone This lithofacies is similar in composition to OP1, but contains chert nodules (1 to 4 cm in diametre)(Figure 4.14), inferred to be a result of silicification during diagenesis.

OP16: Bioturbated dolostone This light brown dolostone displays a planar-e fabric with euhedral fine- to medium- grained dolomite rhombs in and adjacent to burrow structures with interstitial microspar cement (similar to Figure 4.15). In certain areas, the original fabric can be distinguished and resembles a burrowed skeletal wackestone. Elsewhere, nonplanar undulatory dolomite mosaics dominate, and com-

Figure 4.14: Chert nodules within a lime mudstone. Outcrop photo of the Palliser Formation, lithofacies OP15 taken at Nordegg field section. This lithofacies is from an outer carbonate platform environment.

pletely overprints the original fabric. Several rhombs feature cloudy interiors. Crystal sizes for both fabrics range between 0.03 and 0.08 mm.

OP17: Packestone and bioturbated lime mudstone rhythmite This lithofacies is defined by interbedded layers of massive packestones and burrowed lime mudstone. Contacts between these two lithofacies are gradual.

OP18: Laminated dolostone This lithofacies hosts two generations of dolomite cement. The first is similar to OP12 and is characterized by coarse anhedral dolomite with cloudy brown interiors. Surrounding the anhedral dolomite are fine grained euhedral rhombs. Peloids remain preserved. In outcrop, this lithofacies is distinguished by centimetre scale planar laminations (Figure 4.16).

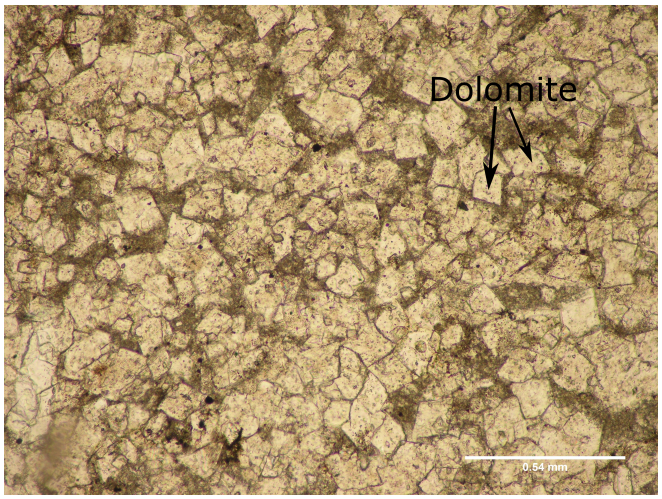

Figure 4.15: Euhedral dolomite fabric surrounded by a microspar intercrystalline matrix. Image taken in PPL of lithofacies OP16. Sample taken from the Palliser Formation at the Nordegg field section. This lithofacies is from an outer carbonate platform.

Figure 4.16: Dolostone displaying planar laminations representative of lithofacies OP19. Image of the Palliser Formation taken at Nordegg field section. This lithofacies is part of an outer carbonate platform.

4.1.3 Inner Platform

The inner carbonate platform depositional environment comprises the Wabamun Group. Previous studies subdivided the Wabamun Group into two formations: the Big Valley Formation and the Stettler Formation [Halbertsma and Meijer-Drees, 1987, Andrichuk, 1960, Wonfor and Andrichuk, 1956]. The Wabamun Group was studied in two core sections, CNRL Tangent (9-23-80-24) and Gulf Mohawk (11-36-7-23W4) (Figure 2.8). Lithofacies characteristics are distinct between these two sections. CNRL Tangent characterised by dolomite-bearing, nodular skeletal wackestones that often grade into skeletal packestones. Facies from CNRL Tangent are similar to those from the Upper Palliser Formation. Gulf Mohawk is characterised by vuggy, dolomitized oolitic grainstones and localized laminated microbialite. Facies from this section overlie evaporites of the lower Stettler and Crowfoot formations. Both sections are unconformably overlain by the Exshaw Formation.

IP1: Dolomitized, peloid, skeletal grainstone-packestone At Gulf Mohawk, this lithofacies is dominated by bioclastic allochems composed predominantly of crinoids and fractured brachiopods. Subordinate allochems, include: gastropods, bryozoan, rugose coral, foraminafers, calcispheres and green phylloid algae. Macroscopic irregular shaped coated grains are visible in hand specimen ($\approx$ 5mm), (Figure 4.17 a). Nuclei of coated grains consist of either microbial filaments or shell fragments (Figure 4.17 b, c). Matrix is predominately micrite. Zebraic silica replacement cement is also prevalent along with traces of iron oxide staining can also be found (Figure 4.17 d). Similar facies characteristics are found at CNRL Tangent section, however, cement is composed mainly of an equant drusy spar mosaic and contains glauconite grains which can be found within the uppermost Big Valley at this location (Figure 4.18).

IP2 - Nodular oolitic grainstone This lithofacies consists of massive, vuggy and nodular brown grainstone composed of ooids ($>$ 0.3 mm), skeletal fragments and peloids. Pore spaces are infilled with dolomite (Figure 4.19 a). Skeletal fragments are mainly composed of brachiopod shells. Brecciated intraclasts are also visible. Three generations of cementation are observed: (1) nodules which are predominantly micritic in composition. (2) allochems surrounded by a blocky isopachous spar cement and (3) coarse calcite observed in proximity to, and in some cases within, the allochems and signifies secondary pore filling cement (Figure 4.19 b). Trace amounts of iron oxide is also visible. Fenestral fabric is observed locally (Figure 4.19 c). Within

the Gulf Mohawk core, an interval measuring 1 m displays crinkly laminations interpreted as microbialite (Figure 4.19 d).

IP3- Recrystallized nodular wackestone This lithofacies is defined by nodular brown wackestone. Nodules incorporate a greater portion of coarser grained sediment. Dissolution seams appear throughout this lithofacies. Skeletal allochems are composed of crinoids and brachiopods and subordinate calcispheres. This facies is heavily recrystallized. Matrix is composed of blocky euhedral clusters of planar-c dolomite.

(a)

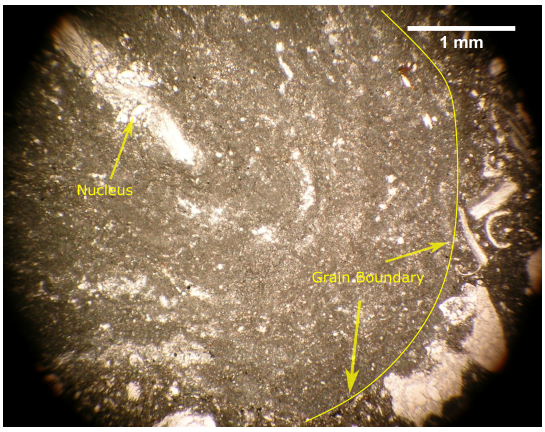

(b)

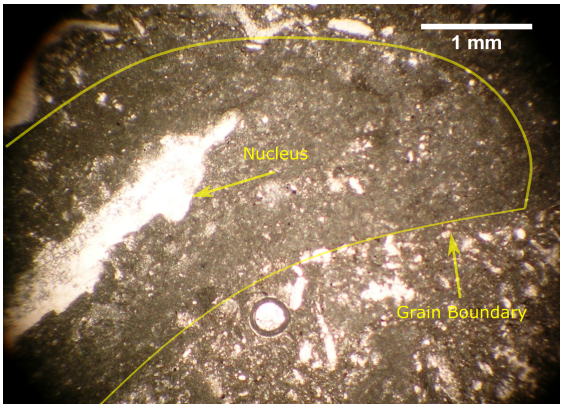

(c)

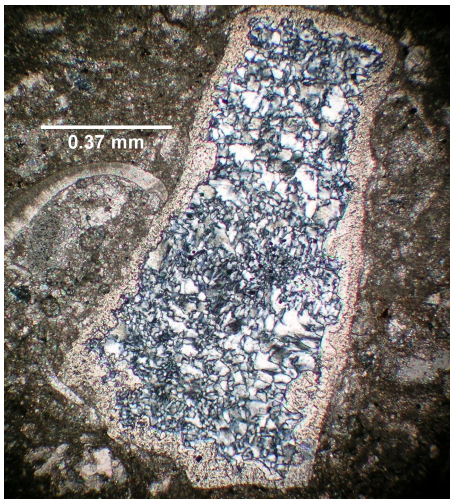

(d)

Figure 4.17: a: Slab section view of irregular shaped, laminated coated grains, b: microscopic view (PPL) of a rounded coated grain, c: Type I = microscopic view (PPL) of an irregularly shaped coated grain, d: Silica replacement texture within a crinoid ossicle. Image taken in XPL. Samples were collected from the Big Valley Formation and represent the inner carbonate platform environment.

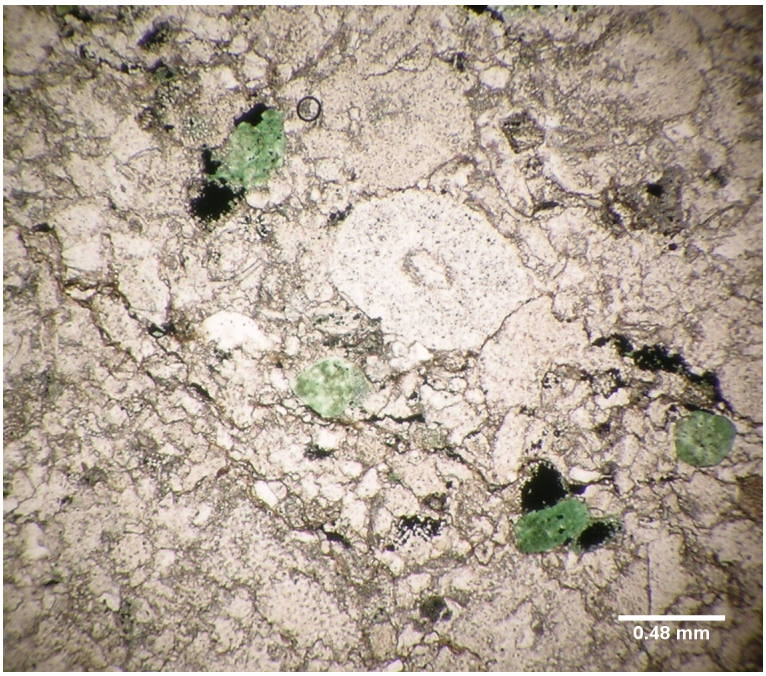

Figure 4.18: Plain polarized light image of green glauconite grains within a skeletal wackestone fabric of the Big Valley Formation at CNRL Tangent section. (Facies IP1 representing the inner carbonate platform environment.)

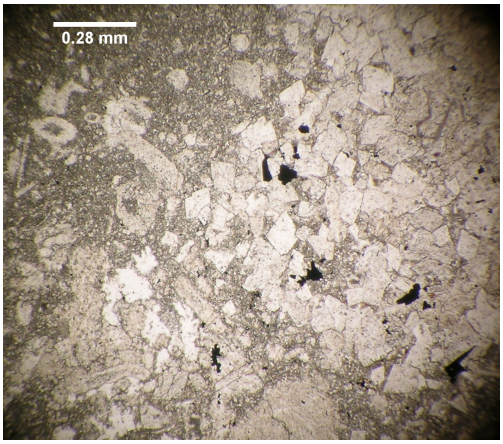

(a)

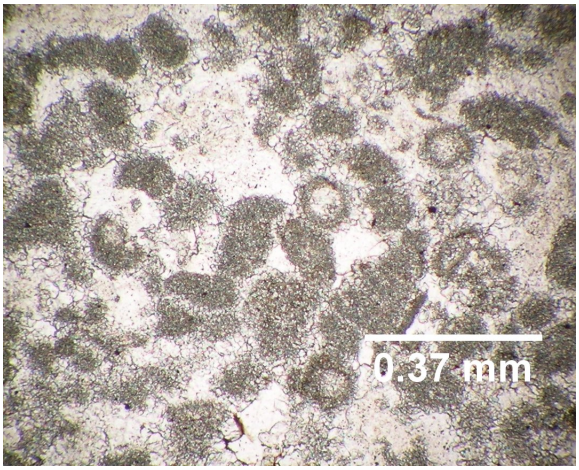

(b)

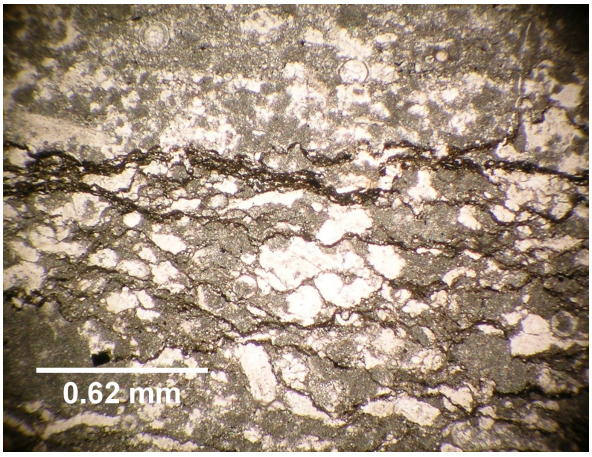

(c)

(d)

Figure 4.19: a: Microscope view (PPL) of euhedral dolomite rhombs within microspar grainstone matrix. Facies IP1 from the inner platform. b: Microscope view (PPL) of equant blocky isopachous cement surrounding allochems (facies IP2). Some of the allochems display broken and recrystallized interiors. c: Fenestrae fabric from IP2 in microscopic view (PPL) with disseminated dissolution seams. Fenestrae are irregularly shaped and filled with a spar cement. d: Core section photo of laminated microbialite texture from facies IP2. Picture (a) is from the CNRL Tangent core and represents the Big Valley Formation, whereas (b), (c) and (d) are from Gulf Mohawk and represents the Stettler Formation.

Facies	Lithology	Physical Features/Texture	Allochems/Fossils	Depositional Environment
B1	Calcareous Siltstone	Black colour, indurated, laminated, disseminated and lenticular pyrite		Deep basin
B2	Massive Siltstone	Black colour, indurated		Deep basin
B3	Carbonate Concretion	Three generations of cementation: Type I - Botryoidal cement Type II - Fringe cement Type III - Blocky cement		Deep basin, diagenetic origin
OP1	Lime mudstone/Wackestone	Dark brown grey to light grey colour, dissolution seams, secondary calcite veining, locally laminated microbialite bearing, locally dolomitized	Peloids, gastropods, brachiopods, crinoids, lime mudstone intraclasts	Outer carbonate platform
OP2	Lime mudstone	Medium to light grey coloured, wispy tan coloured laminations	Peloids, peloid aggregates, gastropods	Outer carbonate platform
OP3	Lime mudstone	Vertical burrows, medium to light grey coloured, wispy tan laminations	Peloids, pelloid aggregates, gastropods and other fragmented fossils	Outer carbonate platform
OP4	Calcareous Siltstone and Lime mudstone/Wackestone	Soft sediment deformation, slump structures, sandstone lenses		Outer carbonate platform
OP5	Calcareous Silstone and Lime mudstone	Interbedded, starved ripples, rip-up clasts, crossbedding		Outer carbonate platform
OP6	Siltstone	Brown grey colour, limestone nodules		Outer carbonate platform
OP7	Siltstone	Light brown colour, low porosity, calcite veining, iron oxide weathering	Detrital quartz	Outer carbonate platform
OP8	Calcareous Siltstone	Light brown to brown grey coloured, ribbon-like bedding	Detrital quartz, peloids	Outer carbonate platform
OP9	Lime mudstone	Silty partings, see OP1		Outer carbonate platform
OP10	Packstone	Dark to medium grey coloured, stylolites, occasional burrowing	Crinoids, brachiopods, gastropods, bryozoa, peloids, biomicrite intraclasts	Outer carbonate platform
OP11	Packstone	Dark to medium grey coloured, bioturbated	Crinoids, brachiopods, gastropods, bryozoa, biomicrite intraclasts	Outer carbonate platform
OP12	Dolostone	Light grey and brown coloured, massive	Interlocking anhedral dolomite rhombs	Outer carbonate platform
OP13	Wackestone	Burrowed, fenestral fabric, locally laminated microbialite bearing, see OP1	see OP1	Outer carbonate platform
OP14	Wackestone and Packstone	Buff coloured, stromatoporoids	Bivalves, crinoids, gastropods, bryozoa, peloids	Outer carbonate platform
OP15	Lime mudstone	Chert nodules, see OP1	see OP1	Outer carbonate platform
OP16	Dolostone	Burrowed	euhedral dolomite rhombs	Outer carbonate platform
OP17	Packstone and Lime mudstone	Massive packstone interbedded with burrowed mudstone		Outer carbonate platform
OP18	Dolostone	Laminated, Two generations of dolomite:(1) Anhedral, cloudy interiors (2) fine grained euhedral rhombs	Peloids	Outer carbonate platform
IP1	Grainstone and Packstone	Silica replacement, trace iron oxide weathering	Crinoids, gastropods, rugose coral, bryozoa, green phylloid algae, foraminifers, calcispheres, coated grains, glauconite	Inner carbonate platform
IP2	Grainstone	Porous, nodular texture, microbialite bearing	Ooids, peloids, brachiopods, brecciated intraclasts	Inner carbonate platform
IP3	Wackestone	Recrystallized, nodular, dissolutions seams	Crinoids, brachiopods, calcispheres, blocky euhedral dolomite	Inner carbonate platform

Table 4.1: Lithofacies characteristics of Besa River, Snaring, Jura Creek, Crowsnest Pass, CNRL Tangent and Gulf Mohawk sections.

4.2 Facies Association

All facies described are summarized in Table 4.1

4.2.1 Deep Basin

Besa River and Exshaw Formations

Core from A-38-B/94-N-08 Besa River (Figure 2.8 and Figure 4.20), located within the Liard Basin of Northeast BC, consists of a massive mudrock succession which extends from the Middle Devonian to the Early Carboniferous [Kabanov et al., 2019]. A portion of this core was logged and sampled (40 m in length), including the contact of the Upper Besa River to the Lower Exshaw formations. Because the two formations share similar lithologies, the contact was inferred based on a prior unpublished geological assessment conducted at the time of drilling by CNOOC Petroleum North America ULC. The bottom 20 m, which represents the Besa River Formation, consists of an alternating succession of laminated and unlaminated (i.e. massive) siltstone (facies B1 and B2). This succession continues into the Exshaw, however, with more pronounced fissility. The Exshaw Formation is regionally extensive across the WCSB (though with variable thickness), and is considered equivalent to the Lower Bakken Formation of the Williston Basin [Richards et al., 1990, Smith and Bustin, 2000]. Facies B1 was observed at Gulf Mohawk and CNRL Tangent interbedded with B2. Facies B2 was also observed at Nordegg, Jura Creek and Crowsnest Pass. Facies B3, which contains macroscopic carbonate concretions, was found in sections at Jura Creek and Crowsnest Pass.

4.2.2 Outer Carbonate Platform

Sassenach Formation

The Sassenach Formation outcrops prominently in the Jasper sub-basin of the Front Ranges, and is considered equivalent to, though lithologicaly distinct from the dolomitic upper Alexo Formation [Workum and Hedinger, 1992, Becker, 1997]. Here it was sampled and studied at a single location (Snaring, Figure 2.8 and Figure 4.21). Here, the Sassenach and lower Palliser formations outcrop fairly continuously over a distance of 390 m along Highway 16, adjacent to Morrow Peak. The base of the Sassenach at this location is underlain by argillaceaous carbonates and calcareous

shales of the Mount Hawk Formation. The contact between these two units, which represents the Frasnian-Famennian boundary, is conformable.

The basal portion of the section is composed of lime mudstone facies (OP1 to OP3) throughout the first 100 metres, above which is 25 meters of cover. Following the covered-interval, large-scale soft sediment deformation (OP4) occurs over the next 20 m interval. Deposition of this facies separates limestone facies from an overlying mixed siliciclastic-carbonate successions (OP5 - OP9). The Sassenach is 338 m thick at this locality, and its contact with the lower Palliser Formation is observed. The contact is gradual and conformable, but marks a transition back to more pure limestone facies.

Palliser Formation

Portions of the Palliser Formation were sampled from all four field locations (Figure 2.8). Jura Creek was the only section to contain the lower and upper contacts of the Palliser. Identification of the Morro and Costigan members were inferred based on previously published descriptions of the Palliser in the Front Ranges [Kaylor, 1988, Meijer-Drees et al., 1993, Richards et al., 1993, Peterhänsel et al., 2008].

Morro Member At Snaring (Figure 4.21), the lower Morro is sampled from the top of the Sassenach contact through to the succeeding 50.8 m of the Lower Palliser Formation. The Sassenach contact is overlain by skeletal mudstones (OP1) and burrowed mudstones (OP3) up to 35 m, eventually grading into coarser grained lithologies with the occurrence of variably burrowed to skeletal wackestones and packestones (OP11, OP1 and OP10).

At Jura Creek (Figure 4.23), the Lower Palliser is in contact with dolostones of the underlying Alexo Formation. The contact between the units is covered with overburden and was not observed. The first 20 m of this succession features massive dolostones (OP12) with dolomite abundances decreasing upwards. The following 100 m is broadly characterized by mixed skeletal and burrowed wackestones and packestones (OP1, OP11 and OP13). An 11 m thick unit of stromatoporoid-bearing packestones (OP14) is observed. The upper portion of the Morro Member features sharp alternations between skeletal packestones (OP10), cherty mudstones (OP15), burrowed dolostones (OP16), and other previously observed lithofacies (OP3 and

OP11). The final portion of uncovered Morro member is a ≈ 12 m section of packestone-mudstone rhythmites (OP17).

At Crowsnest Pass (Figure 4.24), the Upper Palliser up to the Exshaw contact was logged and sampled. Anticlinal folding and thrust faulting occur at this location [McClay and Insley, 1986], thus great care was needed to measure a contiguous stratigraphic section. Previous conodont stratigraphy work has correlated this section with the Upper Morro Member [Johnston et al., 2010]. The basal portion of this section is characterised by skeletal and burrowed limestones (OP1, OP3, OP13). However, lithofacies become less abundantly burrowed and concurrently, more fossil-rich and coarse-grained upsection (OP10). These units are overlain by a 10 m thick unit (from 41 m to 50 m from the datum) of stromatoporoid-bearing skeletal wackestones (OP14), followed by another succession of skeletal and burrowed wackestones - packestones (OP1, OP10 and OP13). Facies transitions become frequent from 73 m to 87.5 m. At this height, a thrust fault means that 6 m of the uppermost Morro Member could not be logged. However, the final 3.6 m of the Upper Palliser (potentially the entire Costigan Member, see below) was logged, including the contact with the overlying Exshaw.

Costigan Member At Jura Creek (Figure 4.23), only the uppermost 4.6 m of Costigan member is exposed. This section is defined by 4 m of massive lime mudstone (OP1) containing laminated microbialites. This unit has been previously been referred to as a stromatolitic boundstone [Kaylor, 1988, Peterhänsel et al., 2008], and is capped by a metre thick unit of cherty mudstone (OP15) which in turn is sharply overlain by the Exshaw Formation (Figure 4.4).

At Nordegg (Figure 4.22), a 40 m overturned section contains the Upper Palliser Formation up to the Lower Exshaw contact. Based on lithological characteristics, the Palliser here cannot be readily divided into members, however, previous conodont analysis has correlated this section to the Lower Costigan Member [Savoy et al., 1999]. The basal portion of the section (from 0 to 6 m) features massive unlaminated and laminated dolostones (OP12 and OP18), divided by a thin layer of lime mudstone (OP1). Dolostones gradually transition back into typical limestone lithofacies (OP1, OP11, OP13). This succession is finally capped by chert nodule bearing mudstones (OP15) which is in sharp contact with the overlying

Exshaw Formation.

At Crowsnest Pass (Figure 4.24), a section measuring 3.6 m, is composed of burrowed skeletal wackestones and mudstones (OP13 and OP15). Correlation with the Costigan Member is based, in part, on the presence of laminated microbialite, which is characteristic of that member. Previously reported conodont stratigraphy done at this section correlates these rocks to the Lower Costigan Member [Johnston et al., 2010].

4.2.3 Inner Carbonate Platform

Wabamun Group

Lithofacies representing the Wabamun Group were observed in two core sections: 11-36-7-23W4 (Gulf Mohawk) and 9-23-80-24W5 (CNRL Tangent) (Figure 2.8). The Wabamun Group is comprised of the Stettler Formation and Big Valley Formation, which are recognized broadly in the Alberta subsurface. These units underlie the Exshaw Formation. Previous authors have correlated the Wabamun Group to the Palliser Formation, with the Big Valley Formation correlating to the Upper Costigan Member, based on lithological characteristics and conodont fauna [Meijer-Drees et al., 1993, Johnston et al., 2010].

The logged CNRL Tangent section is 33 m thick (Figure 4.25). The basal portion of this section (i.e. 1764 to 1788 mbs) is characterized by recrystallized nodular wackestones (IP3). This facies is conformably overlain by partially dolomitized facies (IP1) representing the Big Valley Formation. This unit, in turn, is overlain unconformably by the Lower Exshaw Formation (B2).

The logged Gulf Mohawk section is 10 m thick (Figure 4.26). This was the thinnest section logged in this study. The basal portion of this section overlies the Frasnian Crowfoot Formation, characterised by evaporitic anhydrite and dolomites with pervasive collapse breccia structures. Depth 1961.5 to 1954.5 mbs is comprised entirely of nodular oolitic grainstone representing the Stettler Formation (IP2), the first 1.5 m of which is heavily dolomitized. Laminated microbialite structures are observed at 1958 mbs (Figure 4.20 d). This unit is overlain by skeletal grainstones of the Big Valley Formation (IP1). The final metre of this section (1952.55 to 1951.5

mbs) represents the Exshaw Formation (B2) which overlies unconformably the Big Valley Formation.

4.3 Stable Isotope Geochemistry

4.3.1 Carbon

All carbon isotope values are reported relative to the Vienna Pee Dee Belemnite standard (VPDB).

Besa River (Basin)

Vertical profiles in $\delta^{13}C$ show distinct point-to-point variability (Figure 4.20). Values of $\delta^{13}C$ range from -2.6‰ to 4.6‰, with a population average of -0.1‰ and standard deviation of 1.7‰. While sampling was done at an interval of 0.5 m, only 27 of 42 samples had enough $CaCO_3$ for a reliable isotopic measurement, resulting in the somewhat irregular data distribution displayed in vertical profile. The sampled carbonate concretion (B3) has a $\delta^{13}C$ value of 3.3‰. Values of $\delta^{13}C$ are variable throughout the entire Exshaw and are slightly more positive compared to the Besa River Formation (0.0‰ vs -0.2‰).

Snaring (Outer Platform)

Values of $\delta^{13}C$ from the Snaring section range from -0.92‰ to 2.3‰ with an average value of 1.3‰ for the Sassenach Formation (Figure 4.21). Values of $\delta^{13}C$ are relatively constant in the Sassenach Formation (standard deviation = 0.6‰); however, there is a slight negative trend from the base of the Sassenach towards the Palliser contact. Near the contact, at 333 m, there is a pronounced drop in $\delta^{13}C$ from 0.6‰ to -0.5‰ before returning to normal values. Samples from the lower Palliser have an average $\delta^{13}C$ of 0.3‰ with a standard deviation of ±0.4.

Nordegg (Outer Platform)

Values of $\delta^{13}C$ from the Nordegg section range from -3.3‰ to 1.9‰, with an overall average value of -0.2‰ (Figure 4.22). Variability and overall drop in $\delta^{13}C$ is greatest in the lower 7 m of the section, which coincides with dolomite-rich facies (average $\delta^{13}C$ = -1.6‰, standard deviation = 1‰). From 9 to 34 m $\delta^{13}C$ values are relatively

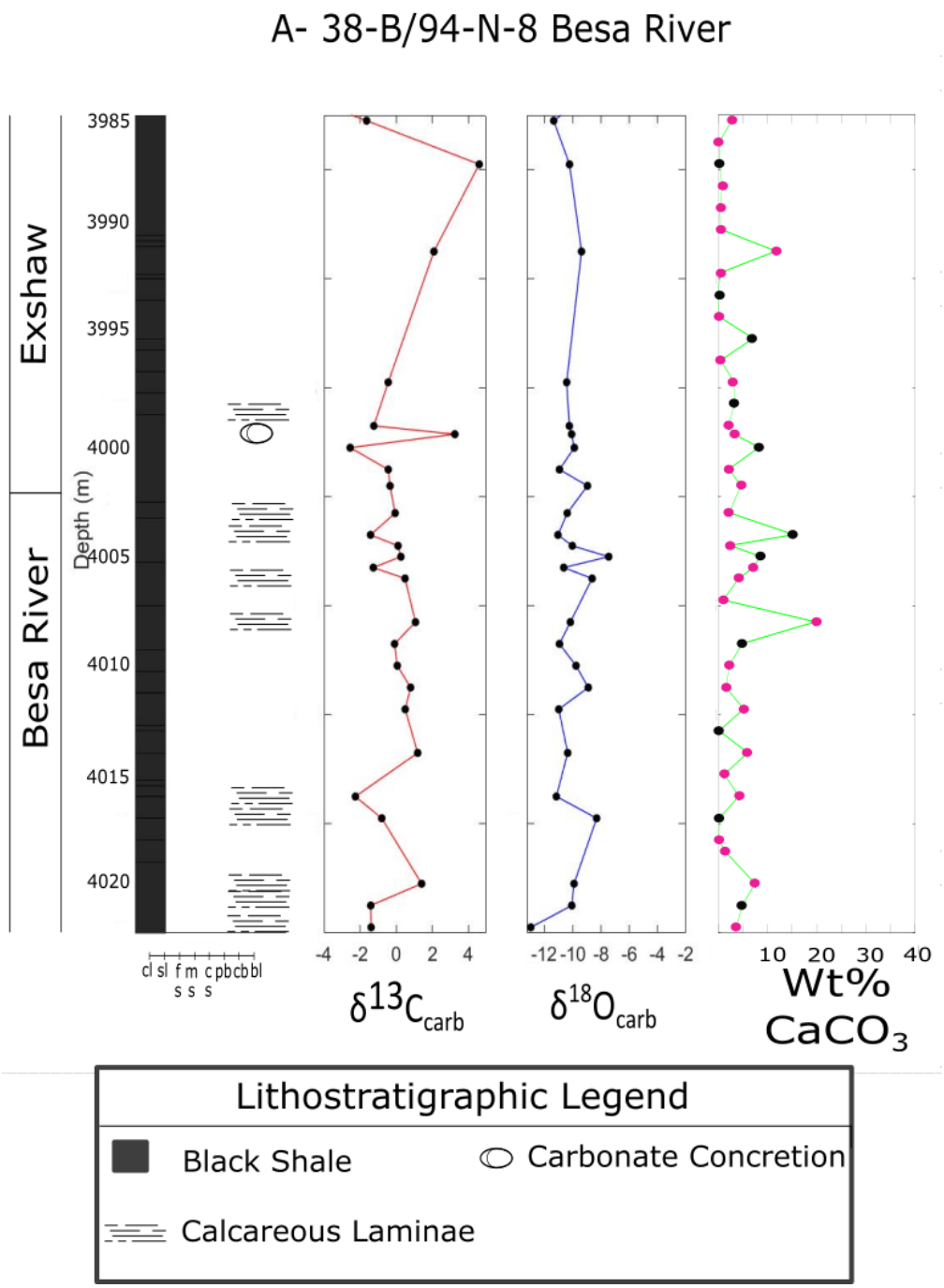

Figure 4.20: Stratigraphic column of the Besa River core. Lithostratigraphic classification is based on grain size: (cl) clay, (sl) silt, (fs, ms,cs) sand, (pb) pebble, (cb) cobble and (bl) boulder. Sedimentary structure symbols taken from [Zervas et al., 2009]. Isotope data are available in Table A.1, Appendix A. weight % $CaCO_3$ data are available in Table A.1, Appendix A. Black dots are coulometry measurements, magenta dots are inferred from IRMS beam area data (Figure 3.2).

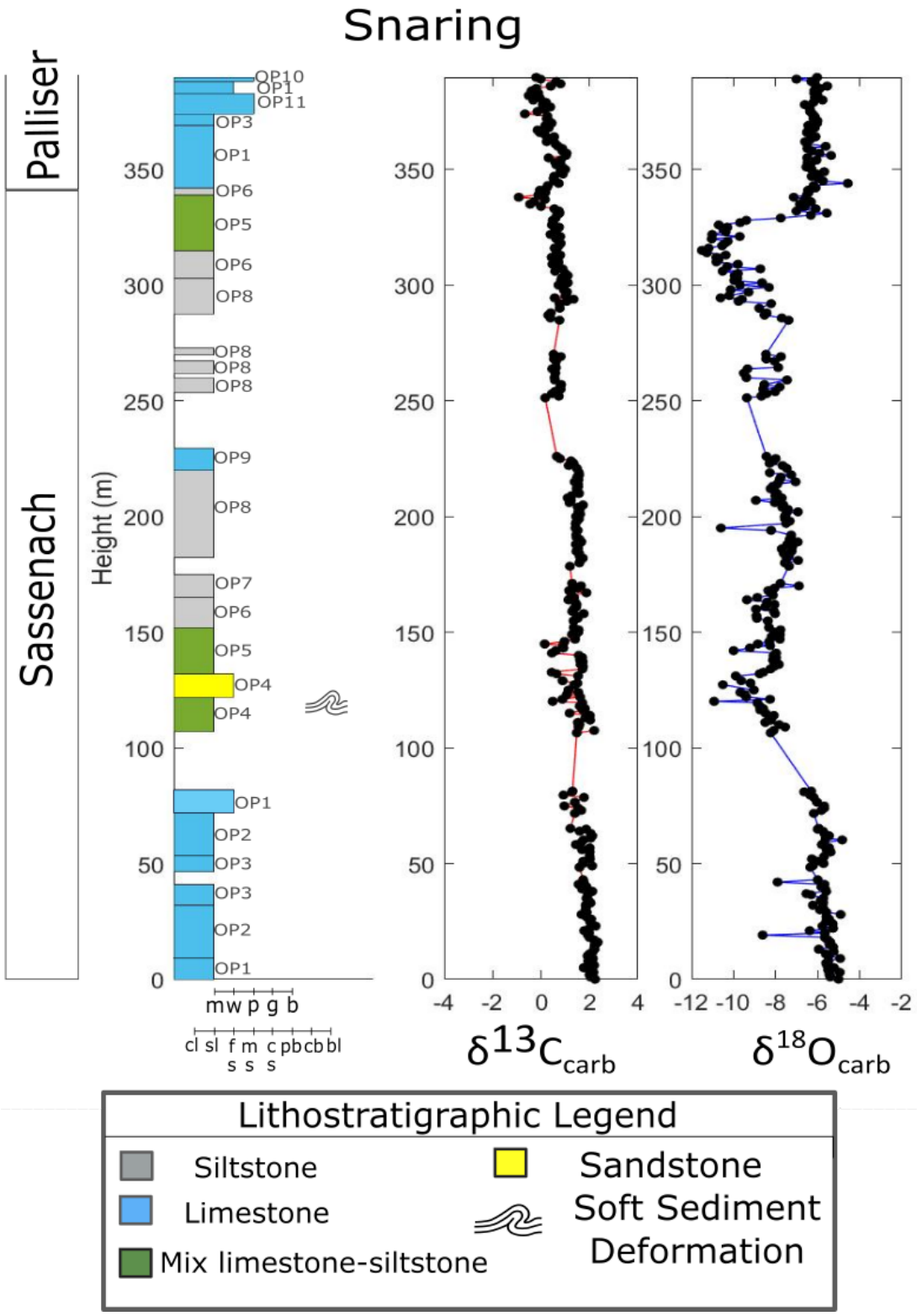

Figure 4.21: Stratigraphic column of the Snaring section. Two systems of lithostratigraphic classification are presented. The first is based on grain size: (cl) clay, (sl) silt, (fs, ms, cs) sand, (pb) pebble, (cb) cobble and (bl) boulder. The second, based on Dunham's classification [Dunham, 1962]: (m) lime mudstone, (w) wackestone, (p) packestone, (g) grainstone and (b) boundstone. Isotope data taken available in Table A.2, Appendix A.

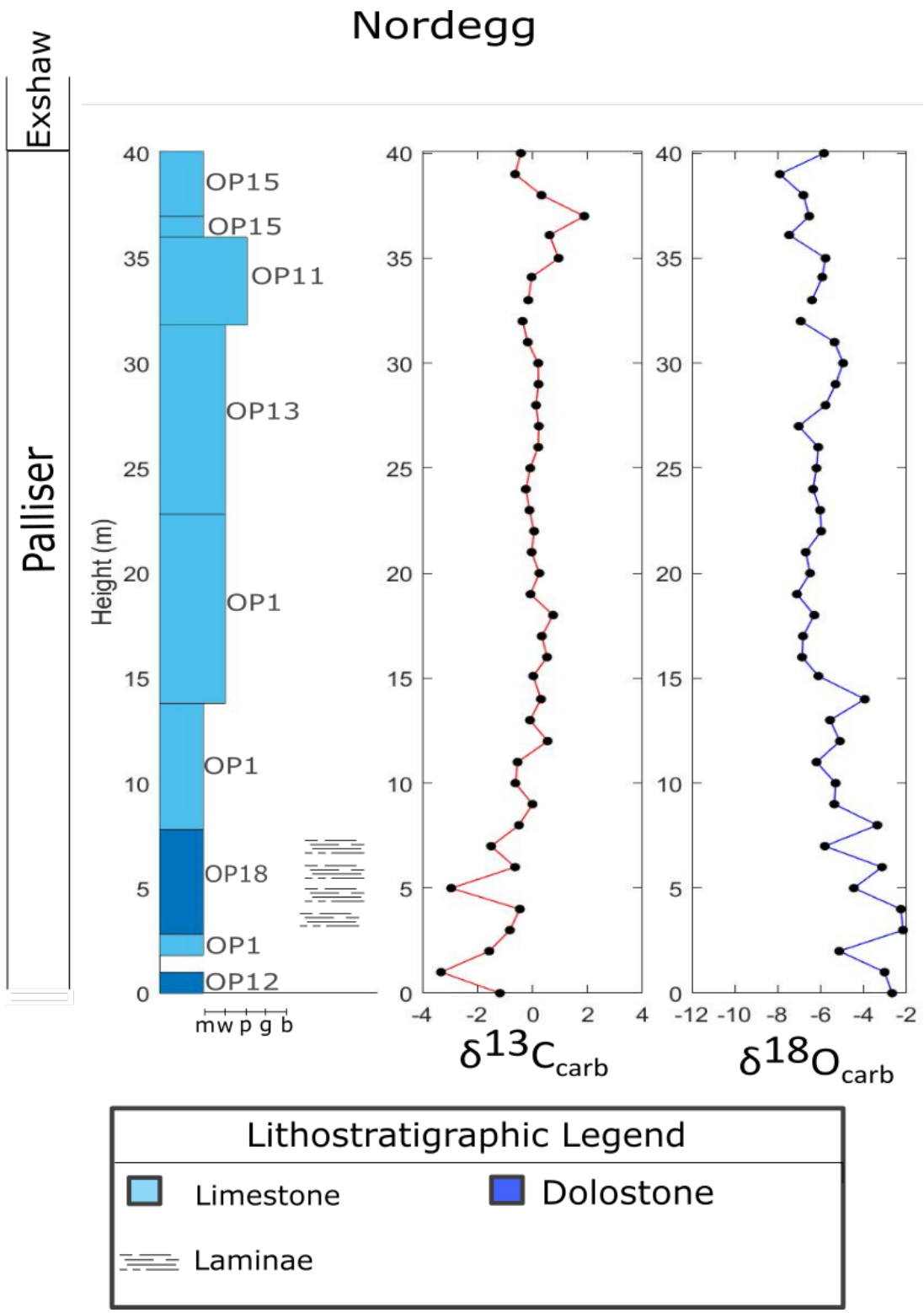

Figure 4.22: Stratigraphic column of the Nordegg section. The lithostratigraphic classification presented is based on Dunham's classification [Dunham, 1962]: (m) lime mudstone, (w) wackestone, (p) packestone, (g) grainstone and (b) boundstone. Sedimentary structure symbols taken from [Zervas et al., 2009]. Isotope data available in Table A.3, Appendix A.

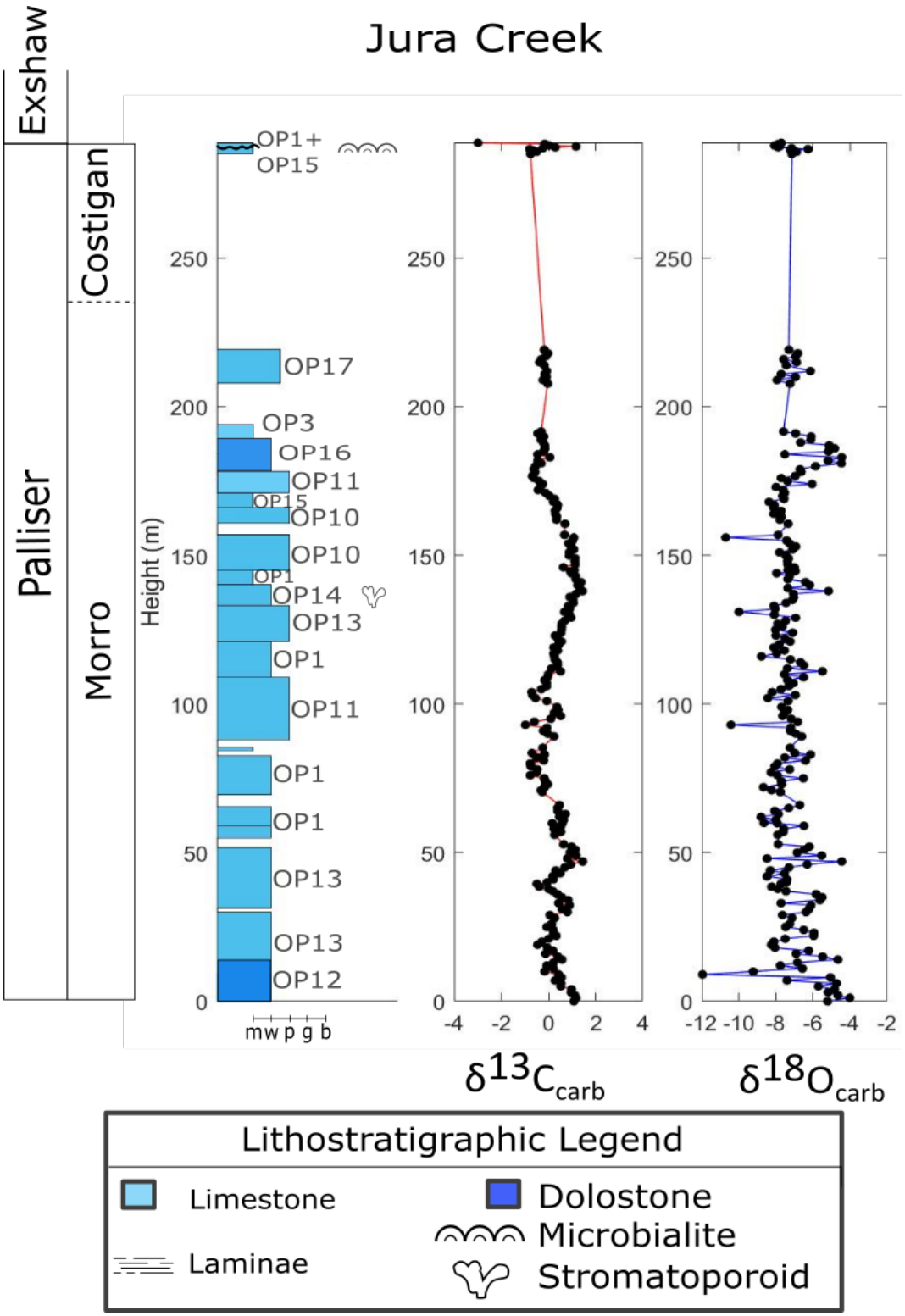

Figure 4.23: Stratigraphic column of the Jura Creek section. The lithostratigraphic classification presented is based on Dunham's classification [Dunham, 1962]: (m) lime mudstone, (w) wackestone, (p) packestone, (g) grainstone and (b) boundstone. Sedimentary structure symbols taken from [Zervas et al., 2009]. Isotope data taken from Table A.4, Appendix A. Dashed line signifies inferred contact.

constant (average = 0.1‰, standard deviation = 0.5‰). One outlier is observed at 37 m above the datum, and has a δ^{13}C of 1.9‰.

Jura Creek (Outer Platform)

Values of δ^{13}C from the Jura Creek section range from -3‰ to 1.5‰, with an overall average value of 0.2‰ (Figure 4.23). Variability in δ^{13}C within the section is of a similar magnitude as the Snaring section (standard deviation = 0.7‰). There is a slight increase in δ^{13}C from 108 to 141 m reaching a peak value of 1.4‰. At the contact between the Palliser and Exshaw, there is a prominent δ^{13}C outlier of -3‰. One lone concretion sampled within the Exshaw Formation (not shown in figure) has a measured δ^{13}C of -3.1‰.

Crowsnest Pass (Outer Platform)

Values of δ^{13}C for the Crowsnest Pass section range from -0.9‰ to 0.7‰, with an average value of -0.2‰ and a standard deviation of 0.3‰ (Figure 4.24). This section displays the least point-to-point variability in δ^{13}C amongst all sections.

CNRL Tangent (Inner Platform)

Limestone samples for the Tangent section have δ^{13}C values ranging from -0.1‰ to 2.5‰, with an average value of 0.4‰ and standard deviation of 0.5‰ (Figure 4.25). Shale samples have δ^{13}C values ranging from -0.6‰ to -0.1‰, with an average value of -0.3‰ and a standard deviation of 0.2‰. Values of δ^{13}C within this core section display little to no variability from depths 1788 m to 1762.5 m. There is a positive δ^{13}C excursion at 1761.5 m, defined by two data points, with a maximum value of 2.5‰. δ^{13}C measurements cease at 1757 m owing to a lack of carbonate content above the lowermost Exshaw Formation.

Gulf Mohawk (Inner Platform)

Dolostone samples for the Gulf Mohawk section have δ^{13}C ranging from -4.8‰ to -3.8‰, with an average value of -4.3‰ and a standard deviation of 0.4‰ (Figure 4.26). Limestone samples have δ^{13}C ranging from -8.4‰ to -1.95‰, with an average of -4.1‰ and a standard deviation of 1.7‰. Shale samples have δ^{13}C ranging from -3.2‰ to -1.9‰, with an average value of -2.6‰ and a standard deviation of 0.6‰.

A negative $\delta^{13}C$ excursion down to -8.4‰, defined by two data points, is observed at the Big Valley - Exshaw contact.

4.3.2 Oxygen

All oxygen isotope values are reported relative to the Vienna Pee Dee Belemnite standard (VPDB).

Traditionally, the measurement of stable oxygen isotopes has been used as a geochemical proxy for seawater temperature through geologic history (i.e. paleothermometry) [Anderson and Arthur, 1983]. These stable isotope ratio measurements are made on samples of biogenic calcite and aragonite that are thought to be in isotopic equilibrium with seawater at the time of precipitation, and reflect the $\delta^{18}O$ and temperature of the fluid from which they form [Epstein et al., 1951, Craig et al., 1965, Shackleton, 1967, Fairbanks et al., 1997].

The accuracy of $\delta^{18}O$ paleothermometry measurements is dependent on the preservation of carbonate samples. Average $\delta^{18}O$ of marine sediments throughout the Phanerozoic, but especially the Paleozoic, show a negative trend with increasing age [Veizer and Hoefs, 1976]. This negative trend has been interpreted by some as a primary signal reflecting lower $\delta^{18}O$ values of seawater in the early Earth [Veizer et al., 1997, Wallmann, 2001, Kasting et al., 2006], and/or perhaps of higher seawater temperatures at this time [Karhu and Epstein, 1986, Knauth and Lowe, 2003, Tartèse et al., 2016]. Alternatively, this trend has been attributed to an artifact of secondary post-depositional alteration between isotope exchange reactions with meteoric water [Keith and Weber, 1964, Hudson, 1977, Banner and Hanson, 1990] or the resetting of $\delta^{18}O$ values in carbonate rock at higher temperatures [Bernard et al., 2017]. Thus, the measurement of oxygen stable isotopes within carbonate rocks can also provide insight into the diagenetic history of the rock.

Here, $\delta^{18}O$ is monitored as a proxy for meteoric diagenesis. Owing to the high elemental abundance of oxygen relative to carbon in water, fluid-rock exchange reactions will readily re-set the oxygen isotope system. Meteoric fluids, which are depleted in ^{18}O, will recrystallize limestone and replace the original $\delta^{18}O$ value

with a lower one. The δ^{13}C values of carbonates will also be lowered as a result of biologically derived CO_2 soil gas as meteoric fluids percolates through the substrate [Allan and Matthews, 1982]. Thus, covariation towards lower δ values between carbon and oxygen isotopes is often an indicator for meteoric diagenesis [Magaritz, 1983, Banner and Hanson, 1990].

Besa River (Basin)

Values of δ^{18}O range from -13‰ to -7.5‰, with an average value of -10.1‰ and standard deviation of 4.5‰ (Figure 4.20). No covariance between δ^{13}C and δ^{18}O is observed in this section (Figure 4.27).

Snaring (Outer Platform)

Sassenach δ^{18}O values range from -11.5‰ to -4.9‰, with an average value of -7.7 ‰ and a standard deviation of 1.6‰ (Figure 4.21). Palliser δ^{18}O values range from -7.0‰ to -4.6‰, with an average of -6.2‰ and a standard deviation of 0.4‰. Variability in $\delta^{18}O$ values is larger in the Sassenach Formation relative to the Palliser. There is a sharp shift towards higher δ^{18}O values near the Palliser contact, from -11‰ towards -6‰. This noticeable increase seems to correlate with a sharp depletion in δ^{13}C, from 0.6‰ to -0.5‰.

Nordegg (Outer Platform)

Dolostone δ^{18}O values range from -5.8‰ to -2.1‰, with an average of -3.6‰ and a standard deviation of 1.3‰(Figure 4.22). Limestone δ^{18}O values range from -7.9‰ to -3.4‰, with an average value -6.1‰ and a standard deviation of 0.9‰. Dolostone lithofacies δ^{18}O values are noticeably more variable and higher relative to limestone lithofacies. Correlation between carbon and oxygen isotopes remains weak across the whole section (Figure 4.27).

Jura Creek (Outer Platform)

Dolostone δ^{18}O values range from -12‰ to -4‰, with an average of -6.3‰ and a standard deviation of 1.7‰(Figure 4.23). Limestone δ^{18}O values range from -10.4‰ to -4.5‰, with an average value of -7.3‰ and a standard deviation of 0.9‰. One lone concretion sampled from within the overlying Exshaw (not shown in figure) has a

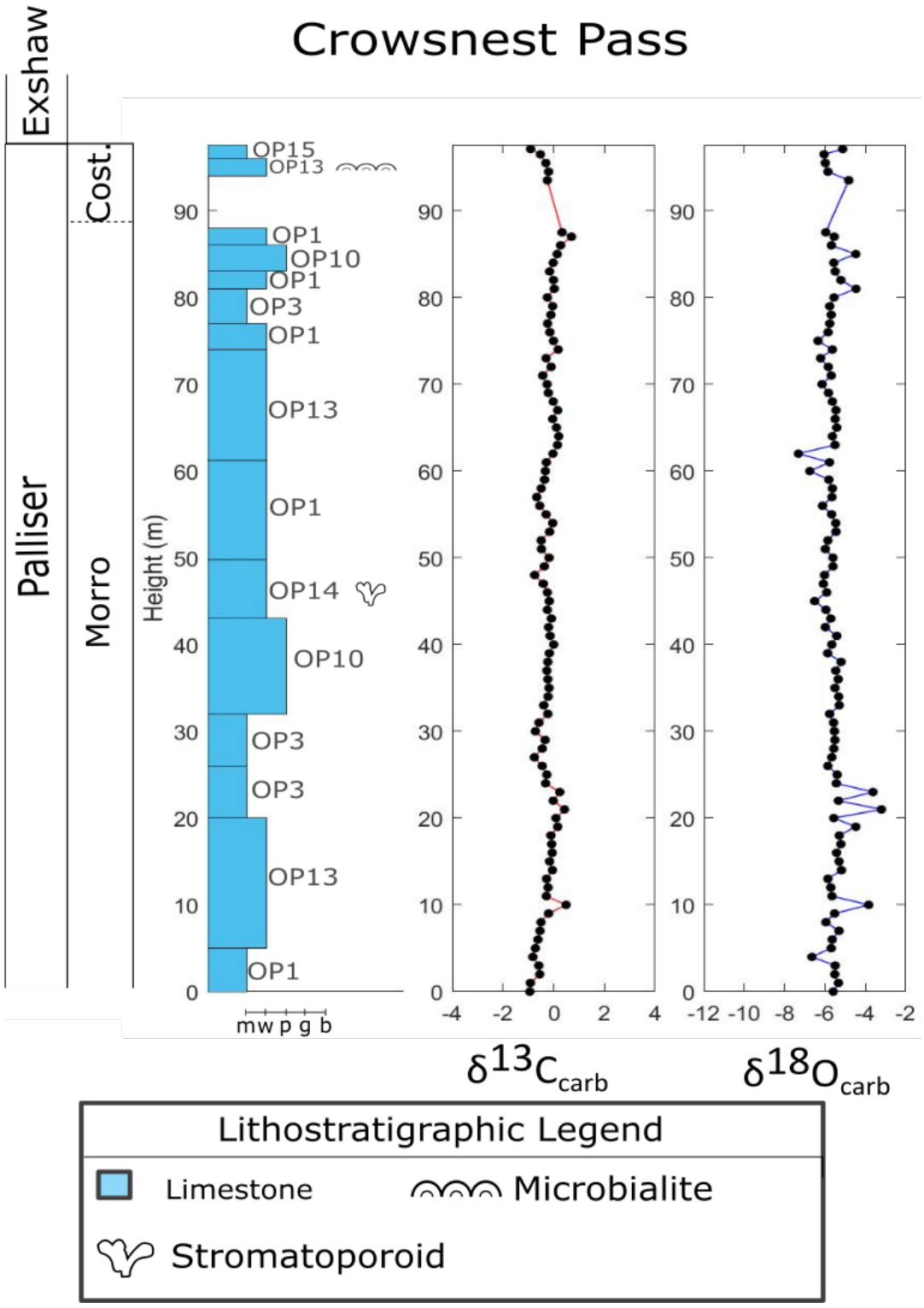

Figure 4.24: Stratigraphic column of the Crowsnest Pass section. The lithostratigraphic classification presented is based on Dunham's classification [Dunham, 1962]: (m) lime mudstone, (w) wackestone, (p) packestone, (g) grainstone and (b) boundstone. Sedimentary structure symbols taken from [Zervas et al., 2009]. Isotope data available in Table A.5, Appendix A. The Costigan Member is here abbreviated to "Cost."

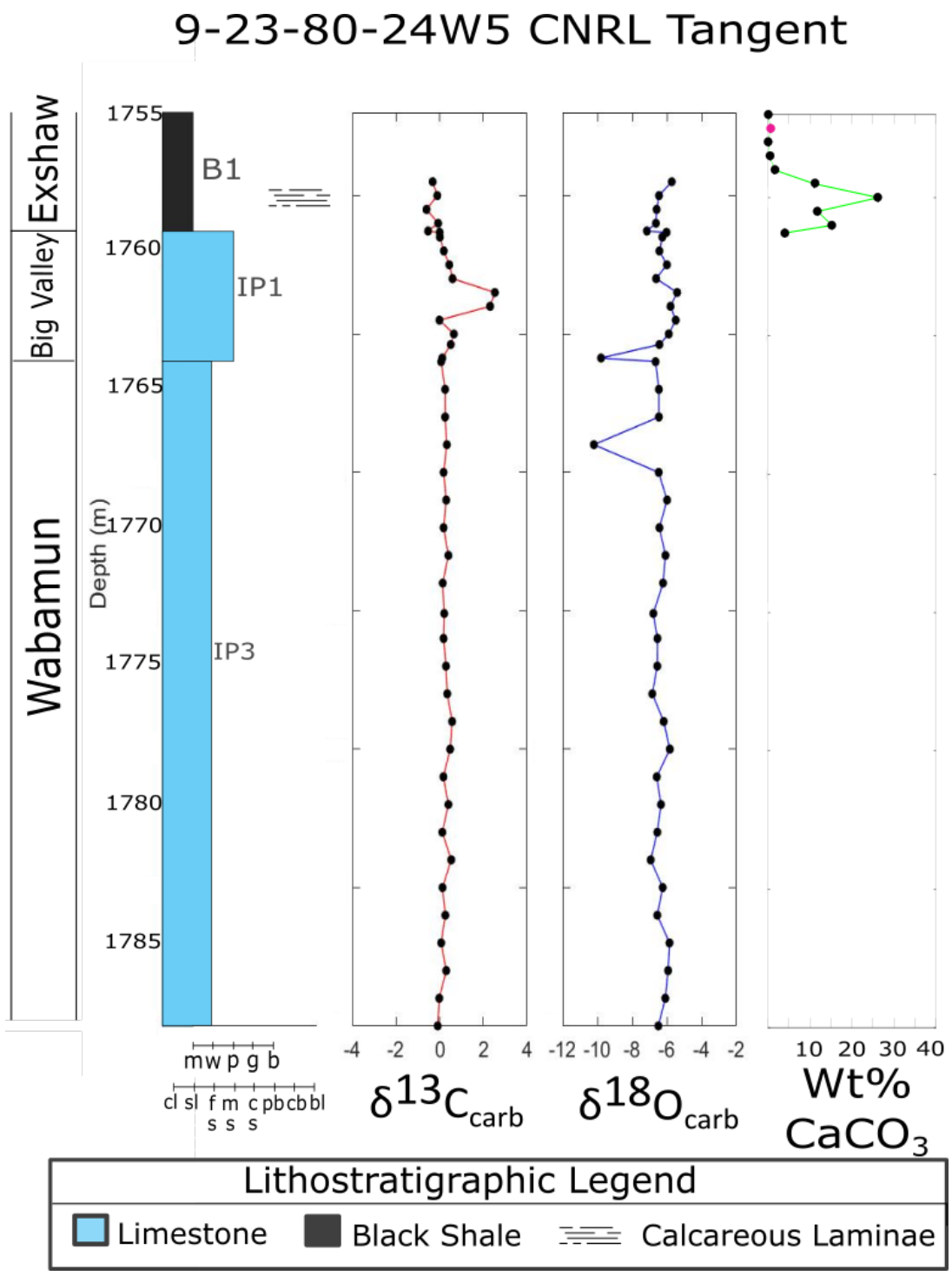

Figure 4.25: Stratigraphic column of the CNRL Tangent core. Two systems of lithostratigraphic classification are presented. The first is based on grain size: (cl) clay, (sl) silt, (fs, ms,cs) sand, (pb) pebble, (cb) cobble and (bl) boulder. The second, based on Dunham's classification [Dunham, 1962]: (m) lime mudstone, (w) wackestone, (p) packestone, (g) grainstone and (b) boundstone. Isotope data available in Table A.6, Appendix A. Shale weight % $CaCO_3$ data available in Table A.6, Appendix A. Black dots are coulometry measurements, magenta dots are inferred from Figure 3.2.

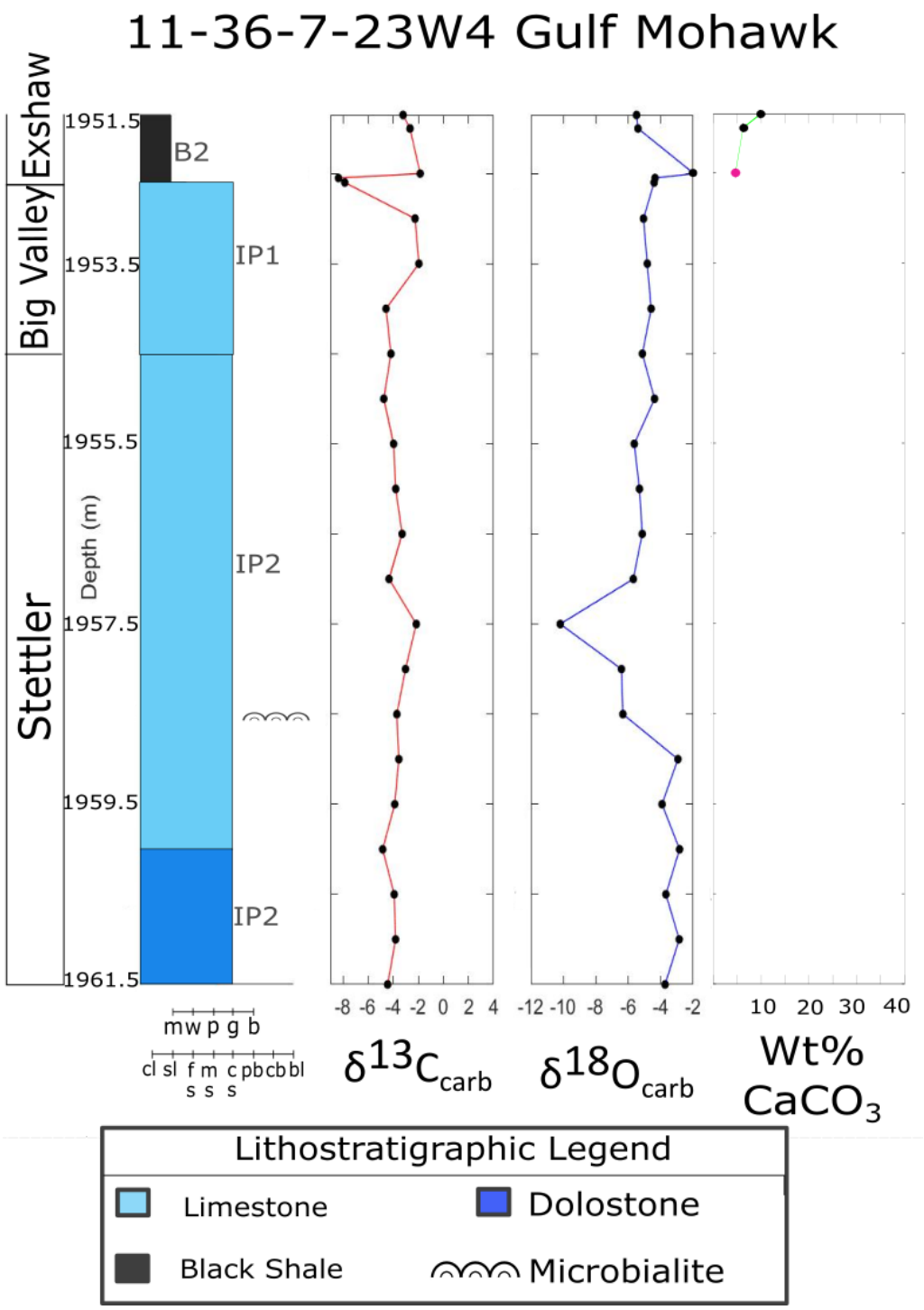

Figure 4.26: Stratigraphic column of the Gulf Mohawk core. Two systems of lithostratigraphic classification are presented. The first is based on grain size: (cl) clay, (sl) silt, (fs, ms,cs) sand, (pb) pebble, (cb) cobble and (bl) boulder. The second, based on Dunham's classification [Dunham, 1962]: (m) lime mudstone, (w) wackestone, (p) packestone, (g) grainstone and (b) boundstone. Isotope data available in Table A.7, Appendix A. Shale weight % $CaCO_3$ data available in Table A.7, Appendix A. Black dots are coulometry measurements, magenta dots are inferred from Figure 3.2.

measured δ^{18}O composition of -8.2‰. Two prominent δ^{18}O excursions are observed in this section. A negative outlier at 9 m with a value of -12‰, and positive outliers at around 185 m with a values of -4.5‰. However, there is no overall covariance with δ^{13}C in this section (Figure 4.27).

Crowsnest Pass (Outer Platform)

Values of δ^{18}O range from -7.3‰ to -3.2‰, with an average of -5.6‰ and a standard deviation of 0.6‰ (Figure 4.24). δ^{18}O displays no trend with stratigraphic height and no covariance with δ^{13}C (Figure 4.27).

CNRL Tangent (Inner Platform)

Limestone δ^{18}O values range from -9.8‰ to -5.4‰, with an average of -6.5‰ and a standard deviation of 0.9‰(Figure 4.25). Shale δ^{18}O values range from -7.2‰ to -5.7‰, with and average of -6.5‰ and a standard deviation of 0.5‰. Values of δ^{18}O show little stratigraphic trend, with the exception of negative outliers at depth 1767 m (-10.2‰) and at depth 1763.47 m (-9.8‰). There is no covariance observed with δ^{13}C (Figure 4.27).

Gulf Mohawk (Inner Platform)

Dolostone δ^{18}O values range from -3.7‰ to -2.0‰, with an average of -3.3‰ and a standard deviation of 0.4‰ (Figure 4.26). Limestone δ^{18}O values range from -10.2‰ to -2.9‰, with an average value of -5.3‰ and a standard deviation of 1.6‰. Shale δ^{18}O values range from -5.5‰ to -2‰, with an average value -4.3‰ and a standard deviation of 1.4‰. Several patterns within this section can be distinguished. The lower 3 m of the sections has higher δ^{18}O values and corresponds with dolostone and several limestone lithofacies. This is followed by a negative δ^{18}O outlier of -10.2‰ at a depth of 1957.5 m. Afterwards, throughout the rest of the Stettler and into the Big Valley Formations δ^{18}O remains more or less constant at an average value of -5.0‰. At the contact between the upper Big Valley and lower Exshaw, there is a sharp trend towards relatively high δ^{18}O, attaining a value of -2.0‰. This spike correlates with a sharp decrease in δ^{13}C (Figure 4.27).

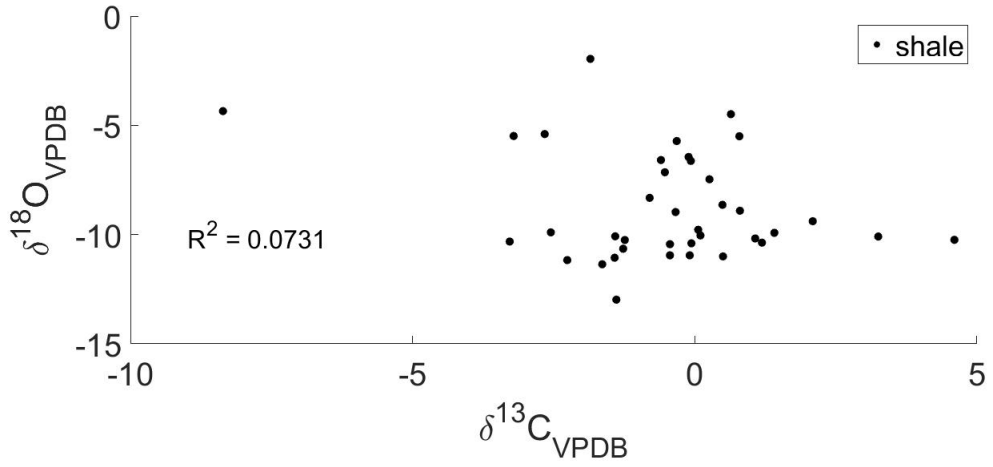

(a)

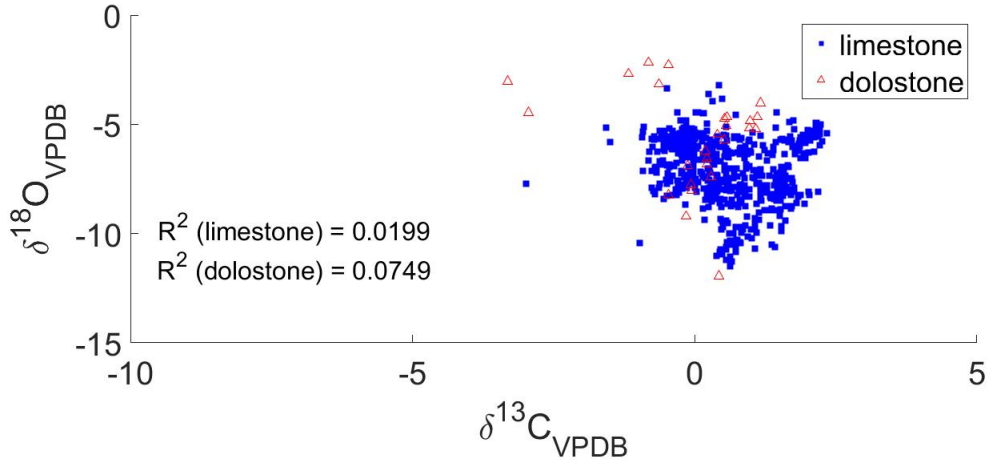

(b)

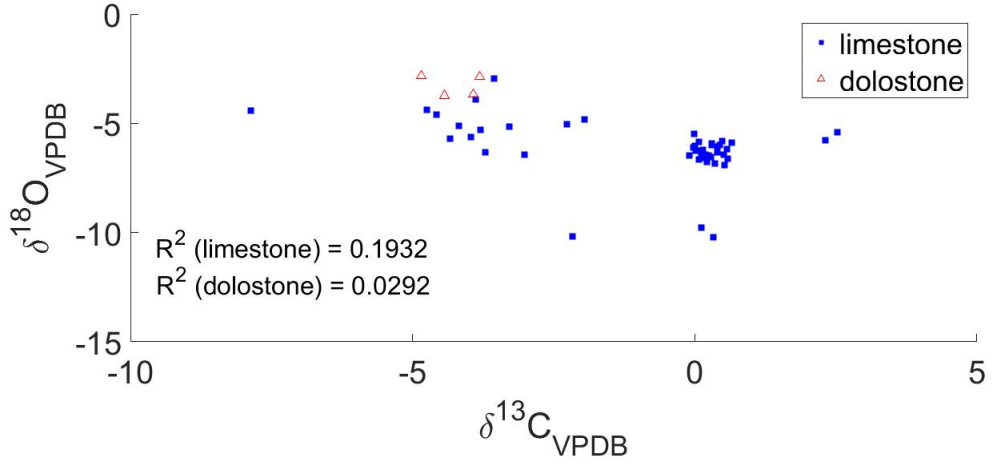

(c)

Figure 4.27: δ^{13}C vs δ^{18}O cross-plots representing each of the three depositional environments a: Basin, b: Outer carbonate platform, and c: Inner carbonate platform.

4.4 Shale Geochemistry

Using coulometric titration, the total weight percent of disseminated calcium carbonate ($CaCO_3$) was measured from 21 out of 54 black shale samples representing the Besa River and Exshaw formations and excludes any concretions or carbonate veins. Owing to the long processing time for coulometric titration, only a portion of the total amount of samples were selected, at random, and measured. From these direct measurements and inferred measurements were extrapolated by using the method described in Chapter 3 (Figure 3.2). These inferred measurements are meant to represent a rough, semi-quantitative estimate for calcium carbonate content. Sample measurements were then plotted in vertical profile for each section hosting black shale lithofacies. The aim is to quantify the amount of calcium carbonate that is held within basinal siliciclastic units. Samples were collected from cores A-38-B/94-N-8 Besa River, 09-23-80-24W5 CNRL Tangent and 11-36-7-23W4 Gulf Mohawk (Figure 2.8).

4.4.1 Besa River

Pronounced variability in wt% $CaCO_3$ is observed throughout this core section. Measured values range from 0.06% to 15.28%, with an average of 4.80% and a standard deviation of 4.6%. Inferred values range from 0.09% to 19.67%, with an average value of 3.53% and a standard deviation of 3.94%. Three noticeable positive outliers occur: depth 4008 m with a value of 19.67% (inferred), depth 4004 m with a value of 15.28% (direct) and depth 3991 m with a value of 11.65% (inferred). These spikes do not seem to correlate with areas that display visible laminations within the mudrocks. The majority of the samples have a low $CaCO_3$ content (i.e. $< 5\%$). Measurement of sample at 3999 m depth corresponds to the shale groundmass surrounding the carbonate concretion, and not the concretion itself.

4.4.2 CNRL Tangent

Values of wt% $CaCO_3$ range from 0.19% to 26.25%, with an average of 7.87%. All values from this section represent measured values with the exception of one inferred value of 0.62%. Samples from this section all originate from the Exshaw Formation. $CaCO_3$ content is greatest near the Big Valley contact with the largest spike occurring at depth 1785 m. $CaCO_3$ then quickly descends to low values.

4.4.3 Gulf Mohawk

Gulf Mohawk represents the smallest core section and thus contains only three samples: two measured values (6.25% and 9.85%, with an average of 8.05%) and one inferred value of 4.63%. $CaCO_3$ content increases upsection from the Big Valley contact.

Chapter 5

Discussion

5.1 Depositional History

Previous paleoenvironmental research has supported an epeiric sea facies model for carbonate deposition within the WCSB during the latest Devonian [Stoakes, 1992, Meijer-Drees et al., 1993, Halbertsma et al., 1994, Peterhänsel et al., 2008]. Within this framework, an attempt to link lithofacies characteristics with depositional processes and environments is described. This analysis is followed by a discussion of paleoenvironmental evolution, formation by formation, with the goal of providing a regional sequence stratigraphic model. Globally, the Late Devonian is characterised by peak sea-level highstand in the early Frasnian, followed by a gradual dip in sea-level throughout the Famennian [Haq and Schutter, 2008] (Fig. 5.1). Nonetheless, several transgressions have been documented throughout the Famennian, often associated with glacial eustatic events [Johnson et al., 1985, Sandberg et al., 2002]

5.1.1 Besa River and Exshaw Formation

Core from site A-38-B/94-N-8 Besa River is located within the Liard Basin and represents the westernmost sub-basin of the WCSB (Figure 2.8). Lithofacies found within this section (B1 and B2) are characteristic of the deep marine environment. This interpretation is based upon the abundance of well sorted, fine-grained siliciclastic sediment, a lack of turbidites and other gravity flow deposits, and a lack of bioturbation - all of which suggests a low energy deep marine depositional environment. Across sections representing the carbonate platform (both inner and outer), the Exshaw black shale is found to overlie carbonate lithofacies and is separated by a

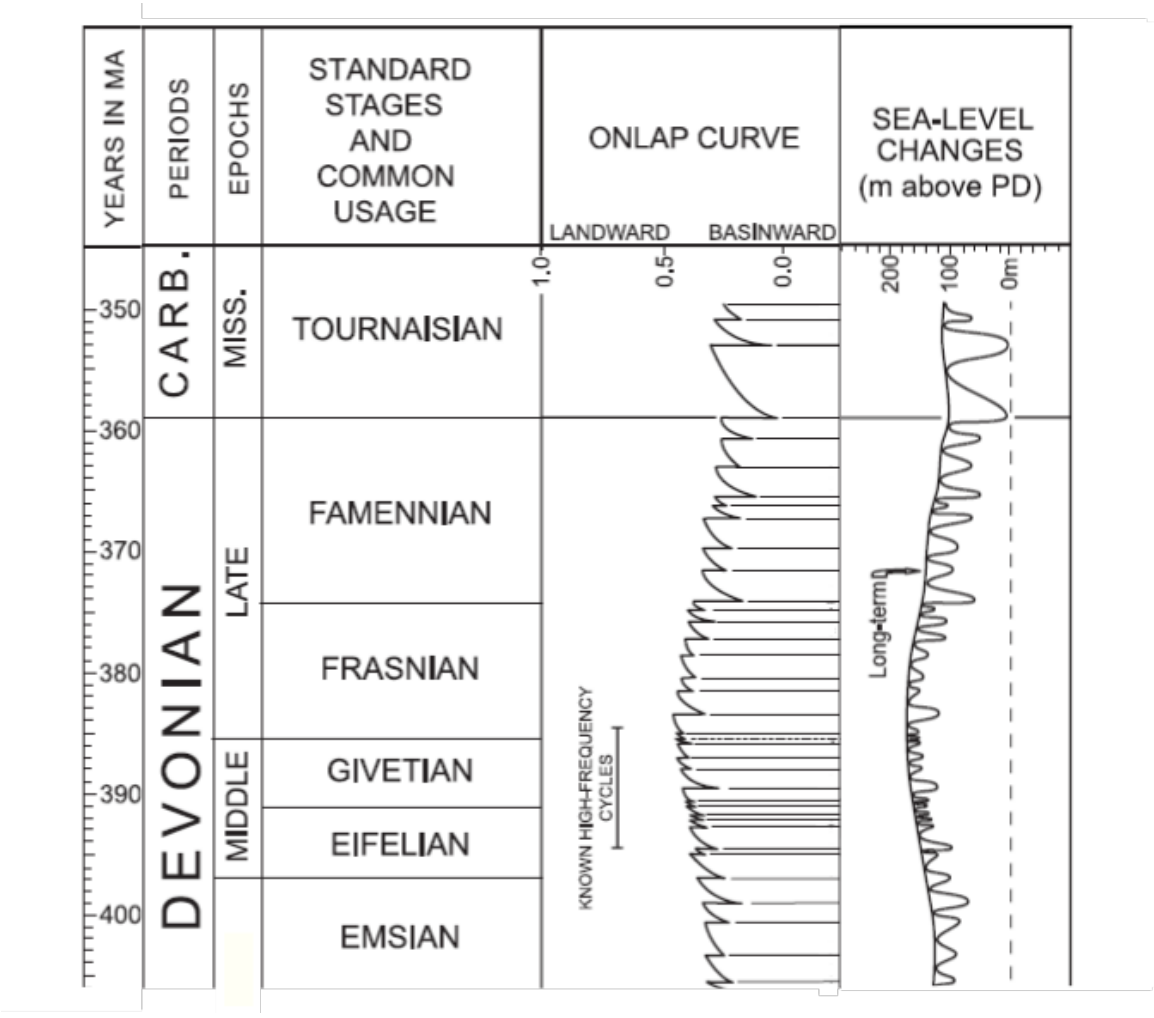

Figure 5.1: Middle Devonian to Early Carboniferous sea-level changes. Left side of the figure are the stratigraphic subdivisions plotted relative to an absolute time scale. Onlap curve is a measure of relative shoreline position estimated from reference sections (not including sections from this study). Sequence boundaries are determined primarily from fossil biozonations (see [Haq and Schutter, 2008]). Sea-level change curve is both a measure of long-term trend and short-term fluctuations. Dashed vertical line at 0 m represents modern sea-level. Sea-level curves are calibrated to modern sea-level. Modified from [Haq and Schutter, 2008].

disconformity. The deposition of deep marine siliciclastics overtop of shelf carbonates strongly suggests a marine transgression. The organic-rich nature of the Exshaw, as well as the presence of framboidal pyrite, suggests deposition under euxinic conditions [Ferri et al., 2011, Kabanov et al., 2019].

5.1.2 Sassenach Formation

The Sassenach Formation broadly conforms to an overall deepening upwards succession in a proximal shallow-water setting, defined by lower energy subtidal carbonate facies in the lower member to cyclic offshore slope facies with significant siliciclastic input in the upper member. Facies OP1 to OP3 within the lower 100 m of the Snaring section (Figure 4.21) represents subtidal deposition of lime mudstones and wackestones, but with deposition occurring above storm wave base as evidenced by alternating burrowed and well-laminated beds. The following 25 m represents a covered interval, which may be a unit of shale overlying the limestones, based on observations of the Sassenach elsewhere in the WCSB [Becker, 1997]. Deposition was then perturbed by a relatively thick interval of soft-sediment deformation (OP4), marked by a sudden influx of detrital silt and sand, probably resulting from an up-dip slope failure. This interpretation is supported by large, metre-scale slump structures and patchy sandbodies. Slope failure may have been in response to early Famennian outboard tectonic activity resulting in mass wasting [Becker, 1997], or large storms. The transition from subtidal shelf carbonates to potential slope siliciclastics would signify the initiation of a transgressive sequence. Overlying facies OP4 are rhythmites (OP5) defined by swirly bedding and pods of fine to medium grained sand, suggesting storm deposition followed by periods of quiescence with lower sedimentation rates, or alternatively, distal fan turbidites. Lime mudstone to wackestone rip-up clasts in the coarser-grained beds further support episodic high-energy deposition. These facies are overlain by carbonate-nodule bearing siltstones, inferred also to be mass wasting deposits (i.e. debrites), most likely from a slope margin. The succession then passes into laminated siltstones, which form the largest portion of the Sassenach Formation, readily identified in outcrop by its “ribbon-like” appearance (OP8). Centimetre-scale bedding, parallel to crossbedded laminations suggests rapid deposition because of the lack of bioturbation, either by storm events or turbidity currents. Overall, this part of the succession can be attributed to an offshore slope environment.

The uppermost part of the Sassenach shows a return to carbonate nodule bearing siltstone and rhythmite facies. Here, rhythmites (OP5) host starved ripples and crossbeds, suggesting either a shoaling caused by sea-level fall or increased uplift rates. At Snaring, the Sassenach is in contact with the Lower Palliser, which features a gradual transition into slightly dolomitized skeletal lime mudstone facies. Limestone lithofacies of the Palliser constitute the final 50 m of this section (Figure 4.21). The contact which separates the two formations is inferred to represent either a change in basin fill deposition, owing to the migration of siliciclastic sediment source away from this depocentre, or a transgressive flooding allowing for the re-establishment of the carbonate factory. Thus, the Sassenach can be interpreted to represent a deepening sequence (OP1-OP4) followed by a shoaling (OP5) resulting from basin fill or relative drop in base-level. The formation then culminates with a possible transgressive surface that marks the beginning of the Palliser.

The provenance of clastic sediments within the the Sassenach has previously been attributed to a western source related to the Antler orogeny, based on the westward coarsening and thickening sedimentary basin [Savoy and Mountjoy, 1995, Becker, 1997]. Moreover, a decrease in ε_{ND} values and relative increase in Zr content from the base of the Sassenach to the top of the formation suggest older source material and a closer proximity to the siliciclastic source compared to the underlying Frasnian-aged Perdrix and Mount Hawk formations (which were sourced from younger, northeastern sourcelands). This evidence was interpreted by the authors to represent tectonic uplift of older source material and subsequent erosion and deposition into the Jasper Basin, potentially coinciding with the Antler orogeny [Stevenson et al., 2000]. However, recent research, partly based on detrital zircon provenance, postulate a northern source for the Sassenach, related to the Ellesmerian and Innuitian orogens, with clastics been transported southward along the Cordilleran miogeoclinal margin [Garzione et al., 1997, Lemieux et al., 2011, Gehrels and Pecha, 2014, Hauck et al., 2017].

5.1.3 Palliser Formation

The Palliser Formation is thought to have been deposited following the overall early Famennian transgression characterised here by the Sassenach Formation [Meijer-Drees et al., 1993, Sandberg et al., 2002]. The base of the Morro Member,

which encapsulates the Lower Palliser Formation, is characterized by transitions between pelleted skeletal mudstone, wackestone and packstone lithologies with variable bioturbation, overall indicative of a subtidal to a lower peritidal marine depositional environment. The frequent presence of biomicrite intraclasts within these facies may be inferred to be from storm-related erosive activity. While the most complete section of the Morro Member was measured at Jura Creek (Figure 4.23), portions of the Upper Morro were also observed at Crowsnest Pass (Figure 4.24). At Jura Creek, the section begins at the base of the Morro Member at its contact with the Alexo Formation, mudstones that are pervasively dolomitized. Between 120 and 135 metres above datum (Figure 4.23), stromatoporoidal-bearing limestones interbedded with wackestones and packestones occur. Similar facies were also observed at Crowsnest Pass (Figure 4.24). The presence of biostromal stromatoporoid assemblages suggest a shallow subtidal environment, which promoted the development of patch reefs. What follows above these reefs is a variable succession of skeletal and burrowed pack-, wacke- and mudstones. Burrow fill was often dolomitized. The uppermost Morro Member, at Jura Creek is characterized by interbeds of massive packstone and burrowed mudstone (OP17). This alternating pattern of deposition is interpreted to be controlled by storm activity, with coarse-grained material deposited during storms. These deposits are then covered by fine-grained carbonate muds during periods of quiescence, which would then allow time and substrate for burrowing by bioturbators. Alternatively, depositional cyclicity may be a response to changing carbonate accumulation rates [Peterhänsel et al., 2008].

The Costigan Member was identified and sampled at Jura Creek, Nordegg and Crowsnest Pass. At Crowsnest Pass (Figure 4.24), the Upper Morro and Costigan members are observed. Here, lithofacies characterized by burrowed and non-burrowed skeletal wacke- and mudstones with bioclastic material dominated by brachiopods and crinoids. The lack of any distinct sedimentary structures precludes the interpretation for any specific depositional environment, other than a shallow marine platform. These lithofacies are overlain by skeletal packstone and stromatoporoidal-bearing wackestones which signal the emergence of patch reefs. This unit is followed by an alternating pattern of burrowed versus non-burrowed skeletal wackestones and mudstones, similar to observations made at Jura Creek. Conodont biostratigraphy has correlated this section with the Upper Morro and Lower Costigan members [Johnston et al., 2010]. The uppermost 5 m of this section displays lithofacies more

in common with the Upper Costigan Member: coarser-grained lithofacies found interbedded with fenestral limestones, laminated microbialites and a thin unit of cherty mudstone, right below the Exshaw Formation contact. These observations suggest variability in depositional conditions. The presence of microbialites, typically found in restricted marine environments in the photic zone, suggests regression relative to the Lower Costigan, followed by flooding represented by the cherty mudstone.

At Jura Creek, the uppermost 5 m of the Costigan Member is found to be in contact with the Exshaw Formation. Here, two separate lithofacies are evident. Cherty mudstones overlie mudstones/wackestones with distinct laminated microbialites, seperated by an undulating disconformity (Figure 4.4). The presence of microbialite-bearing lime mudstone strongly suggests shallow quiet water deposition, possibly in a restricted marine environment, thus indicating a regression within the Costigan Member. The overlying unit of cherty mudstone is inferred to represent an open marine setting. Therefore, the Costigan Member at this location may also record the presence of a lower regression deposit followed by an upper transgression. The undulatory disconformity between the microbialites and the cherty mudstones would then signify a subaeral exposure surface. This interpretation is further corraborated by other studies conducted at Jura Creek [Richards and Higgins, 1988, Peterhänsel et al., 2008, Johnston et al., 2010].

The base of the Nordegg section (the first $\approx$ 15 m) consists of dolostone and dolomitized laminated mudstones (Figure 4.22). The presence of fine-grained lithofacies, combined with occasional parallel laminations, argues for a distal subtidal open-marine depositional environment below storm wave base. An alternative interpretation would be a more proximal, but restricted and storm-protected, marine setting. Approaching the Exshaw contact, lithofacies become coarse grained and the skeletal content increases as characterised by bioturbated to massive packstones and mudstones. The presence of open-marine bioclastic material, as well as rip-up clasts, suggest that deposition occurred somewhere along an open shelf environment but below fair weather base owing to a lack of wave-form sedimentary structures. Based on conodont biostratigraphy this section has been correlated with both the Lower and Upper Costigan members [Savoy et al., 1999].

Previous work has argued for several transgressive-regressive (T-R) cycles within

the Palliser Formation [Peterhänsel et al., 2008], but these were not always evident during logging. Indeed, depositional heterogeneity, especially within the Upper Costigan, suggest variations in either local paleobathymetry allowing for potentially restricted water circulation in certain parts of the platform, or localized storm events influencing sediment distribution. Variable lithostratigraphy is not surprising considering the large geographic distances separating study areas (Figure 2.8). Overall, the Palliser Formation contains abundant peloids and bioclastic material, most notably crinoids and stromatoporoids, and the evidence of bioturbation is consistent with a middle carbonate platform setting that may have been locally subaerially exposed towards the top of the formation. This interpretation is in contrast with the underlying Sassenach Formation, which features lithologies controlled by high energy storm events and abundant siliciclastic input more akin to a distal slope setting.

5.1.4 Wabamun Group

The Famennian Wabamun Group occurs in the subsurface of north-central and southern Alberta (Figure 2.8). Owing to its large extent, the Wabamun displays distinct inter-regional lithofacies characteristics. The Wabamun in southern Alberta is dominated by evaporitic and dolomitic successions, while the Wabamun elsewhere in the province displays limestone-rich, shallow water platform deposits. A notable feature is the Peace River Arch, where a paleotopographic high fostered the development of fringing reef platforms. These reefs are divided into five seperate carbonate members: Dixonville, Whitelaw, Normandville, Lower Cardinal Lake and Upper Cardinal Lake members, recognizable in geophysical logs as sonic potential (SP) reversals and bounded by shale marker beds [Halbertsma and Meijer-Drees, 1987, Dix, 1990].

The Gulf Mohawk core is interpreted to represent the most interior region of the carbonate platform sampled in this study. Here, carbonate deposition is at its thinnest and overlies dolostone and evaporite strata of the Lower Stettler Formation, which have previously been interpreted to represent cyclic sabkha deposition [Fuller and Porter, 1969]. The Upper Stettler represents the lower 7 m of this section, and is composed of oolitic grainstones, possibly representing a shoal complex or intertidal channel deposit. The presence of microbial mats suggests an upper intertidal to supratidal depositional environment. The Upper Stettler is conformably overlain by the Big Valley Formation, which displays more open marine

facies characteristics. Here, the Big Valley is highly fossiliferous and coarse-grained, and underlies the Exshaw black shale. The transition from restricted supratidal lithofacies of the Upper Stettler towards open-marine lithofacies of the Big Valley followed by black shale is interpreted as representing a marine transgression.

The CNRL Tangent section lies within north central Alberta (Figure 2.8). Here, both the Upper Stettler and the Big Valley Formations are present. Unlike at Gulf Mohawk, the Stettler Formation is thicker and lies further away from the continental margin (relative to Gulf Mohawk) and lacks any observable evaporitic or biostromal facies. Light brown skeletal wackestones display a nodular texture with pervasive dissolution seams. Several hardgrounds are observed and are evident in thin section based on distinct cement horizons that truncate allochems. This suggests alternating periods of starved sedimentation, which can occur during extended periods of wave or current action associated with transgressive system tracts [Schlager, 2005]. Dolomitization is prevalent in this section, with certain layers being almost completely recrystallized and others featuring less abundant dolomite. An in-depth study on the nature of dolomitization was not undertaken, and thus, the origin of diagenesis can only be speculated.

The Upper Stettler is overlain by a dark fossiliferous packstone-grainstones of the open marine Big Valley Formation. Lithofacies characteristics are similar to those found in the Gulf Mohawk section, with the exception of glauconite grains found in the uppermost Big Valley (Figure 4.18). The presence of glauconite grains is often associated with transgressive deposits in a shelf setting where sedimentation rates are low and with minimal clastic sediment input [Odin and Fullagar, 1988, Harris and Whiting, 2000, Miller et al., 2004, Wigley and Compton, 2006]. However, recent research has suggested that glauconite may form in a variety of depositional settings, and thus, how it is incorporated into any sequence stratigraphic framework must be treated with caution [Amorosi, 2012, Banerjee et al., 2016]. Black shales of the Exshaw Formation directly overly the Big Valley Formation, separated by an unconformity, marking a marine transgression well into the interior of the platform and a clear transition from the shallow subtidal environment to deeper water anoxic conditions.

5.1.5 Summary

Owing to the large size of the WCSB, depositional facies are highly variable. This can be attributed in part to local paleobathymetry and depositional processes. Thus, only a general sequence stratigraphic framework is presented.

Core section A-38-B/94-N-8 Besa River shows no distinct change in lithofacies across the Famennian and retains characteristics of the deep basinal depositional environment throughout. The outer carbonate platform is represented by the Sassenach Formation and the Morro and Costigan members of the Palliser Formation. The Sassenach at Snaring, which overlies the Frasnian-Famennian boundary, is characterized by an initial deepening upwards succession consisting of subtidal limestones at its base towards high energy mixed siliclastic-carbonate deposits representing the slope environment, which then gradually shoals upward to the Palliser contact. The Sassenach is then overlain by subtidal carbonates of the Morro Member, marking possibly another phase of marine transgression. Considerable depositional heterogeneity is observed within the Palliser Formation, with previous research proposing several transgressive-regressive (T-R) cycles [Peterhänsel et al., 2008, Johnston et al., 2010]. Jura Creek, which displays the most complete section of the Palliser, is characterised by alternating subtidal skeletal-peloidal mudstones and wackestone, with localized packstones and subtidal to lower peritidal stromatoporoid-bearing facies. Positive identification of distinct T-R cycles could not be confirmed with certainty. However, the Lower Costigan Member may in fact contain a minor regression prior to an overall marine transgression that culminated with deposition of the Exshaw black shale. Such a relationship is also observed at Crowsnest Pass. Within the inner platform environment, especially at Gulf Mohawk, there is a clear lithological transition from evaporites of the Lower Stettler and underlying Frasnian-aged Crowfoot to peritidal and subtidal facies of the upper Stettler to open marine facies of the Big Valley Formation, signifying a deepening upwards (i.e. transgressive) sequence. Sedimentological evidence for a regressive episode within the Big Valley Formation, which is correlative to the Costigan Member, is lacking. One possible explanation for the discrepancy in systems tracts of the Upper Palliser between the outer and inner platform, may be due to a forced regression in outer platform deposition reflecting the uplift of a peripheral bulge along the Fifth Meridian [Johnston et al., 2010]. Sediment deposition across the entirety of the platform climaxed with black shale

deposition, which marked the drowning of the carbonate platform.

Causes for the abrupt transition to black shales remain contentious and require a more in-depth study then is presented here. Greater outcrop and core study along with the incorporation of biostratigraphy datasets may help decipher this issue. A plausible reason could be that these facies transitions, especially near the Devonian-Carboniferous boundary, reflect eustatic changes as a result of glaciations. This conclusion is supported by Famennian-aged glacial deposits in South America which suggest glaciation of Gondwana [Veevers and Powell, 1987, Isaacson et al., 2008] and by the variance in miospore assemblages and land plant diversity which suggest cyclical climatic gradients [Streel et al., 2000]. Alternatively, eustastic sea-level changes has been previously attributed to mid-oceanic thermal uplift and submarine volcanism depophases whereby increased rates of sea-floor spreading (possibly related to the spreading of the Paleotethys Ocean or the Viluy rift) decreases the volume of deep ocean basins, resulting in sea-level rise up onto continental blocks [Johnson et al., 1985, Bond and Wignall, 2008, Golonka, 2020]. It has also been proposed that WCSB relative sea-level changes are a result of mantle flow induced epeirogeny, in which subsidence and crustal rebound occur as accumulating subduction zone slab material penetrates an endothermic phase change zone within the mantle, possibly linked to the accretion of Pangea [Pysklywec and Mitrovica, 2000, Flowers et al., 2012, Hardebol et al., 2012]. However, such a process would only apply to large-scale trends in sea-level, which may not be appropriate for resolving small scale T-R cycles observed in the Palliser/Wabamun. Nonetheless, the cause of facies variations within the WCSB remains contentious.

5.2 Stable Isotope and Carbonate Geochemistry analysis

The proposal of the authigenic sink hypothesis was developed with the focus of explaining sustained periods when $\delta^{13}C$ remained $>>0‰$ in the Mesoproterozoic and Neoproterozoic, despite putatively low levels of atmospheric O_2 [Schrag et al., 2013]. A critical assumption of this hypothesis is that the burial of authigenic carbonate with low $\delta^{13}C$ values in marine siliciclastic units could drive the carbon isotope

composition of seawater (and hence, platformal carbonates that record seawater DIC composition) to higher $\delta^{13}C$ values. The Famennian was chosen as a suitable time period to assess this hypothesis owing to sedimentological conditions suitable for the precipitation of authigenic carbonate (e.g. crash in carbonate depositional systems (Figure 2.6) and ocean anoxia), the latter of which would also have been present in the Precambrian. Throughout all sections representative of the carbonate platform (Figures 4.21, 4.22, 4.23, 4.24, 4.25, 4.26), $\delta^{13}C$ values do not exceed beyond the accepted range for Devonian seawater (Figure 5.2). Furthermore, $\delta^{13}C$ also approximates modern values [Zachos et al., 2001], which is particularly significant considering today's elevated O_2 levels ($\approx$ 20% by volume (modern) vs. $\approx$ 8% to 16% by volume (Late Devonian) [Berner, 2006, Lenton et al., 2016]). Variability in $\delta^{13}C$ is low and the average value is 0.2‰ across all platform sections (with the exception of Gulf Mohawk, Figure 5.2), and is well below the highest values observed in the Neoproterozoic ($\approx$ 10‰, see Figure 2.1). Several positive carbon excursions, however, do occur in Nordegg and CNRL Tangent sections, at 37 m and 1761.5 mbs respectively (Figure 4.22 and 4.25). Both occur within the Upper Costigan/Big Valley and thus can be correlated together. Conodonts from within the Upper Costigan/Big Valley fall within the Lower *expansa* to *praesculata* [Johnston et al., 2010].

The presence of positive carbon isotope excursions within these conodont zones may be attributed to the regional Dasberg event, a smaller-scale episode of faunal overturn preceding the more widely known global Hangenberg event [Hartenfels and Becker, 2009, Myrow et al., 2011, Cole et al., 2015]. This excursion, referred to as the ALFIE (A Late Famennian Isotope Excursion), has been documented in stratigraphic sections of the western United States and has been postulated to represent enhanced carbon burial linked to a warmer period interrupting the overall global cooling trend that characterized the Late Devonian-Early Carboniferous [Sandberg et al., 2002, Myrow et al., 2011]. Sedimentologically, the Dasberg event is characterized by a marine regression, followed by the development of an unconformity and subsequent transgressive deposition of black shales, similar to sections found in the WCSB [Sandberg et al., 2002, Hartenfels and Becker, 2009] (Figures 4.23 and 4.24). Excursions linked to the Hangenberg event were not observed, which is not surprising given that none of the formations contain conodont biozones that hold the Hangenberg isotope excursion (e.g upper *praesculta*, *ckl* or

kockeli).

The Gulf Mohawk core section is a notable outlier (Figure 4.26). This section displays an overall depleted carbon isotope signature (average $\delta^{13}C$ = -4.1‰). Furthermore, a prominent negative carbon isotope excursion (-8.4‰) occurs at 1952.5 mbs, right below the Exshaw contact. While $\delta^{18}O$ and $\delta^{13}C$ values do not correlate, there is abundant petrographic evidence for recrystallization and dolomitization (Figure 4.19 a, b). The most likely explanation for ^{13}C depletion, therefore, is from the input of isotopically light C from the respiration of organic matter. In this scenario, both terrestrial and marine organic matter would have accumulated in the proximal platform environment, and combined with the increased residence time and poor mixing of inner shelf waters with the open ocean, could have resulted in low $\delta^{13}C$ values in the water column. This explanation has been previously applied to modern low $\delta^{13}C$ values in marine carbonates found in Florida Bay, which is a depositional environment that is analogous to Famennian carbonates of the WCSB [Lloyd, 1964, Patterson and Walter, 1994].

However, sustained organic matter respiration in a restricted setting does not explain the sharp decrease in $\delta^{13}C$ values and concurrent increase in $\delta^{18}O$ values at the Exshaw boundary. This signature may be explained through meteoric diagenesis across a subaerial exposure surface during sea-level lowstand, with ^{13}C depletion occurring through the incorporation of ^{12}C enriched soil gas carbon as meteoric waters percolate through the vadose zone, and ^{18}O enrichment occurring by intense evaporation which would preferentially enrich near-surface porewaters.

Variability in $\delta^{18}O$ across the carbonate platform seems to be controlled by burial diagenesis. Comparatively high $\delta^{18}O$ values (-4‰ to -2.2‰, average = -3.1‰) occur across several sections (e.g. Gulf Mohawk and Nordegg) and appear to correlate with zones of dolomitization. Dolomite fabrics in corresponding lithofacies (IP2, OP18, OP16) are idiotopic and tend to fill in burrow structures where present, these dolomites are presumed to have formed at lower burial depths. Conversely, dolomite associated with lithofacies OP12 at Jura Creek, is characterized (at least partially) by lower $\delta^{18}O$ values (-12‰ to -4‰, average = -6.3‰). The dolomite fabric within this facies is non-planar, xenotopic and completely overprints the original fabric. The discrepancy between these two dolomite fabrics and their $\delta^{18}O$

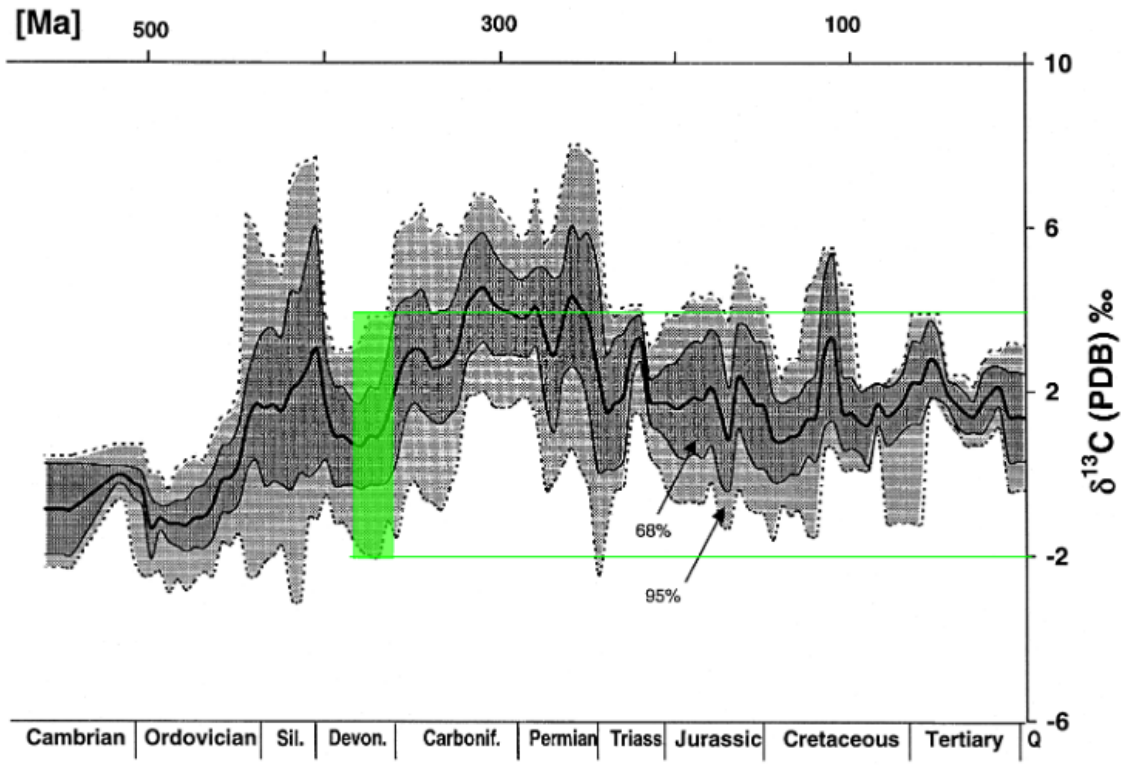

Figure 5.2: δ^{13}C across the Phanerozoic. Green box incorporates the Mid- to Late-Devonian period. Measurements conducted on brachiopod, belemnite and conodont specimens. Modified from [Veizer et al., 1999]

values may be related to the degree of saturation of the dolomitizing fluid and its temperature [Sibley and Gregg, 1987]. Non-planar xenotopic dolomite tends to crystallize above the critical saturation and critical roughening temperature, typically found at deep burial depths, suggesting a burial diagenetic origin for this dolomite fabric. Increased temperatures also leads to smaller fractionations between carbonate minerals and the precipitating fluid, thus explaining the low $\delta^{18}O$ values. A previous study of dolomites within the Wabamun Group determined that matrix dolomites and saddle dolomites with values ranging from -5.7‰ to -12.4‰ tend to form at deeper burial conditions ($\approx$ 800 to 2000 m, with a geothermal gradient of 30°C per km) [Mountjoy and Halim-Dihardja, 1991]. Conversely, planar, idiotopic dolomite tends to form below these high temperatures, suggesting that replacement dolomite formed at shallower burial depths and in areas of high permeability, thus leading to comparatively higher $\delta^{18}O$ values reflecting lower equilibration temperatures. Burial diagenesis may also have had an effect on $\delta^{18}O$ at Snaring (Figure 4.21). Here, mixed carbonate-siliciclastic units display more negative $\delta^{18}O$ values relative to pure carbonate units. Reasons for this difference remain unclear but possibly also relates to $\delta^{18}O$ values resetting at different burial depths depending upon lithofacies. It is worth mentioning that despite the large variability in $\delta^{18}O$ values at this section, $\delta^{13}C$ values between the Sassenach Formation and the lower Palliser are not offset from one another (Figure 4.21). This observation suggests that the process(es) responsible for $\delta^{18}O$ variance does not similarly affect the carbon isotope system, despite the Sassenach being a mixed carbonate-siliclastic unit and the Palliser a more pure carbonate.

Low $\delta^{18}O$ values (mean $\delta^{18}O$ = -10.1‰) were measured within the Besa River and Exshaw formations in the deep basin (Figure 4.20) which may also be explained by resetting at higher burial temperatures. This conclusion is corroborated by thermal maturation studies on the Besa River Formation which calculated maximum burial temperatures of 380°C to 530°C [Potter et al., 1993, Ferri et al., 2012]. In contrast, shales deposited on the carbonate platform, and presumably buried to shallower depths, display comparatively higher $\delta^{18}O$ values (mean $\delta^{18}O$ at Tangent = -6.5‰; mean $\delta^{18}O$ at Gulf Mohawk = -4.3‰, Figures 4.25 and 4.26). Despite evidence for $\delta^{18}O$ resetting at high burial temperatures, there is no evidence for ^{13}C-depleted carbonates within these siliciclastic formations. Owing to the fact that most diagenetic fluids contain relatively low amounts of dissoved CO_2, the

carbon isotope system tends to be rock-buffered, and fractionations are insensitive to temperature. However, carbonate content in these shales is low (average = 0.55 wt% inorganic C), meaning these samples are poorly buffered compared to carbonate rocks. Nonetheless, the breakdown of organic matter at deep burial depths (which is temperature dependent), often results in the formation of fossil fuel deposits (e.g. petroleum and methane), which display very low δ^{13}C values, ranging from -20‰ to -80‰ [Deines, 1980]. These values are far lower than the δ^{13}C values observed in shale-hosted carbonates across all study sections. Thus, it can be posited that these δ^{13}C values were not affected by burial diagenesis.

As opposed to platformal carbonates, according to the authigenic carbonate hypothesis, low δ^{13}C values in carbonates are expected to be found in basinal shales. The Besa River section, the only section representing the deep basin, shows no evidence of pronounced ^{13}C depletion in disseminated carbonate within the shale (mean δ^{13}C value = -0.1‰, Figure 5.3), and the carbonate concretion sampled was measured to have a δ^{13}C of 3.3‰. Carbonate concretions are classic examples of authigenic carbonate. Therefore, this enrichment is particularly striking. Conversely, the carbonate concretion sampled at Jura Creek has an average value of -3.1‰. A possible explanation for this discrepancy is that the concretion in the Besa River section formed within a localized zone of methanogenesis. Indeed, the Exshaw Formation at this location displays a slightly higher δ^{13}C values relative to the underlying Besa River Formation (Exshaw average is = 0.0‰ vs -0.2‰ in the underlying Besa River Formation). As described by Claypool and Kaplan [1974], when sulfate pore water concentrations become exhausted, sulfate-reducing bacteria are replaced by methane-producing bacteria. The production of isotopically depleted methane gas results in net ^{13}C enrichment of pore waters. Very high δ^{13}C values are not found in disseminated $CaCO_3$ in the Exshaw Formation at CNRL Tangent nor at Gulf Mohawk. Additionally, δ^{13}C from carbonate within the Besa River Formation (and the Exshaw at CNRL Tangent and Gulf Mohawk) approximate to seawater values, implying that these carbonate cements were predominantly derived from seawater DIC, rather than oxidized organic matter.

Another critical assumption of the authigenic carbonate hypothesis [Schrag et al., 2013], is that the burial flux of authigenic carbonate is comparable to mass burial fluxes of marine carbonate and organic carbon. To test the

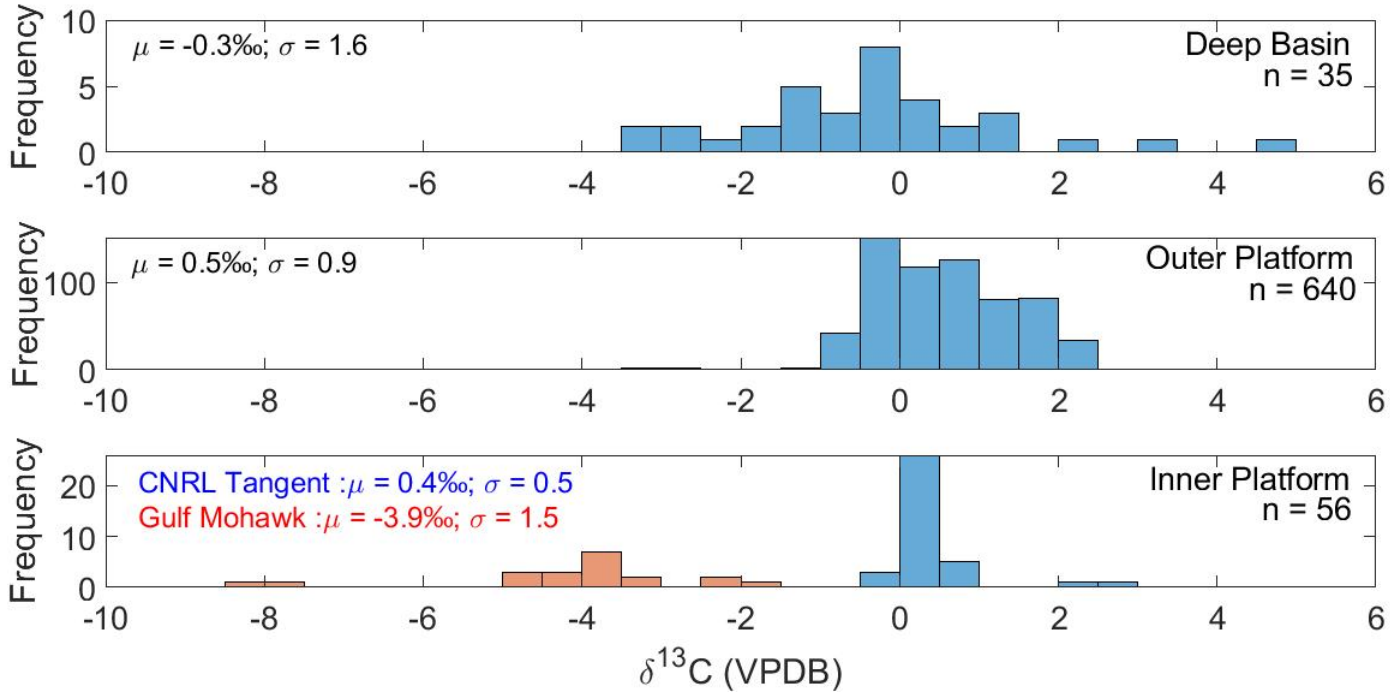

Figure 5.3: Histogram of δ^{13}C values of carbonate samples for all depositional environments. Samples of siliciclastics that did not have a sufficient carbonate content to be measured confidently by IRMS were excluded from the sample number count.

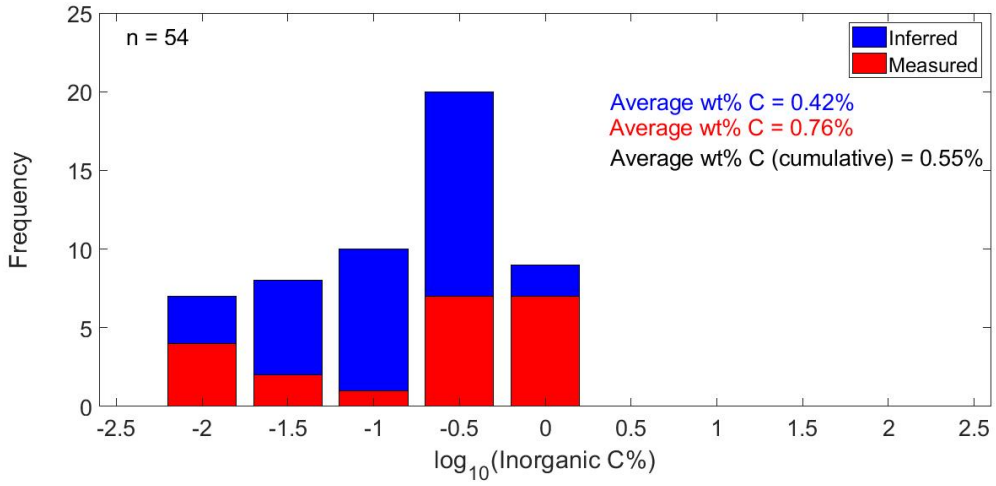

Figure 5.4: Histogram of inorganic carbon content of all shale samples.

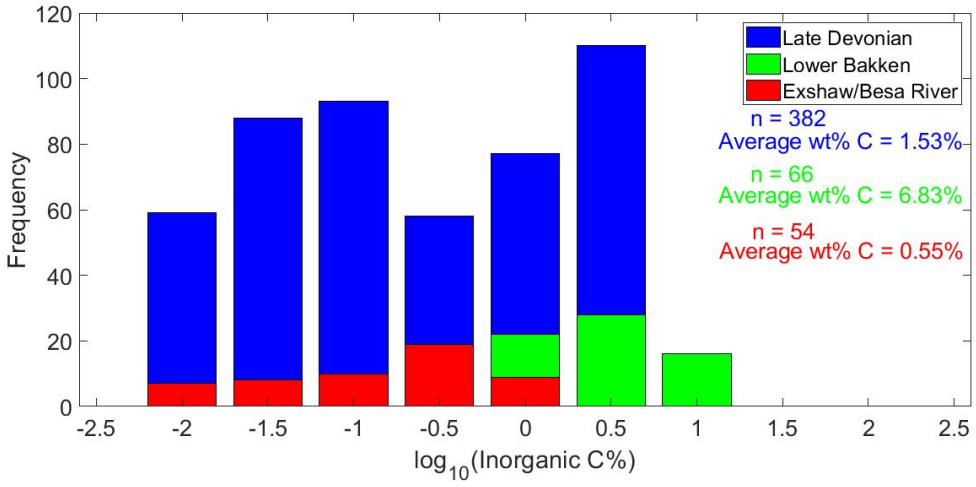

Figure 5.5: Histogram of inorganic carbon content of samples from this study relative to Late Devonian shales and the Lower Bakken Formation. Exshaw and Besa River values are taken from this study (here converted to weight percent inorganic carbon rather than calcium carbonate), while Late Devonian shale and Lower Bakken data is sourced from [Barnes et al., 2019] and the USGS Geochemical database [USGS, 2008] and represent North American formations exclusively. A table of Late Devonian shale formations used in this compilation is given in Appendix B.

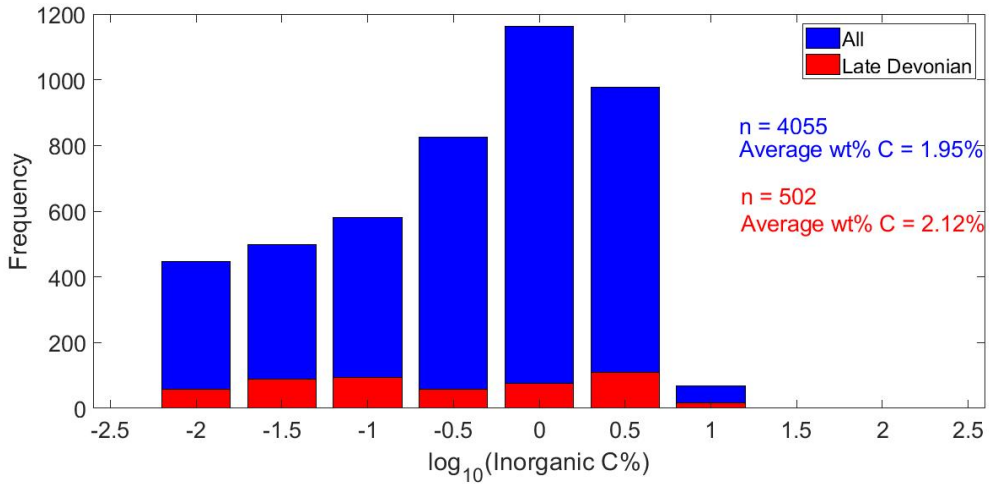

Figure 5.6: Histogram of inorganic carbon content of samples from all Late Devonian shales (including the Lower Bakken, Exshaw and Besa River formations) compared to all shales across geologic history. For information on Late Devonian data, see the caption for Figure 5.5. "All" data is also from the USGS database [USGS, 2008] and includes shale formations from North America and range in age from the Late Precambrian to the Pliocene.

strength of the authigenic sink, weight percent inorganic carbon was measured from Famennian black shales (Figure 5.4). Visible authigenic carbonate was apparent as concretions and fine laminations within the Besa River and Exshaw Formations. Wt% inorganic C values are highly variable, ranging from negligible amounts to as high as 3% (CNRL Tangent section, Figure 4.25 (drafted as wt% $CaCO_3$ in the figure)). Mean wt% inorganic C (both directly measured and inferred from IRMS peak sizes) for all sections is 0.55% (the average for measured is 0.76% and for inferred was 0.42%). These amounts, however, are low when compared to other North American black shales from the Late Devonian, including the Lower Bakken (average wt% inorganic C = 2.31 , 2 tandard errors (2 S.E.) of the mean = 0.32) (Figure 5.5) suggesting that local burial conditions, possibly relating to either changes in porosity, variable organic matter content, or fluctuating redox conditions altering the saturation state of pore waters, may have limited the amount of precipitated authigenic carbonate. Thus, it cannot be assumed that these samples are representative of the Late Devonian as a whole. Indeed, inorganic carbon content is significantly lower relative to the coeval Lower Bakken Formation, which was deposited in an adjacent intracratonic sedimentary basin. This result suggests that the burial flux of authigenic carbonate tend to be greater in ancient intracratonic settings relative to epeiric seaways. Exploring explanations for this observation should be a focus of future studies.

Comparing the inorganic carbon content (assumed to be sourced from authigenic carbonate precipitation) of Late Devonian shales with compiled data from North American shales across the Late Precambrian and Phanerozoic (assumed to be representative of average shale content throughout geologic history), Late Devonian shales have higher amounts of carbonate (average = 2.12, includes samples from the Exshaw and Besa River, 2 S.E. = 0.30) relative to other shales (average wt% inorganic C = 1.95%, 2 S.E. = 0.08) (Figure 5.6). Mean values of the Late Devonian shales and the rest of North American shales overlap at the 2 S.E. level, however, and therefore, do not support the notion of an expanded authigenic carbonate sink during the Late Devonian within Laurentian deposits. What is more significant, however, is that regardless of the burial flux of authigenic carbonate, the average $\delta^{13}C$ of carbonate in shales, within the WCSB, is not significantly different from that of seawater and is comparable to platform carbonate $\delta^{13}C$ values (Figure 5.2 and 5.3). These observations further imply that the precipitation of au-

thigenic carbonate did not have a significant effect on δ^{13}C of late Devonian seawater.

5.3 Famennian Paleoceanography: Implications for the Authigenic Sink

Sedimentological and geochemical results confirm paleoenvironmental conditions conducive to the presence of an active authigenic sink during the Famennian. The precipitation of calcium carbonate, in association with pyrite, within organic-rich black shales in an anoxic basin strongly suggests that alkalinity was produced by sulfate reducing bacteria and therefore should have resulted in authigenic carbonates with low δ^{13}C values. However, relatively positive δ^{13}C values from carbonates in siliciclastic rocks representing the deep basin and outer platform suggests that this carbonate was sourced from oceanic dissolved inorganic carbon rather than degraded organic matter. Similar findings have been reported from other studies on authigenic carbonate hosted formations across the Paleozoic [Saitoh et al., 2015, Gaines and Vorhies, 2016, Barnes et al., 2019]. One explanation for this discrepancy between model expectations and the data are shifts in the depth of the redoxcline, which increases the upward diffusive transport of remineralized organic carbon into the water column, where it is then mixed and diluted by a larger and isotopically distinct DIC reservoir. In other words, low δ^{13}C DIC originates from the anaerobic respiration of organic matter near the sediment-water interface, in an anoxic deep-ocean setting. Porewater depleted in ^{13}C is then mixed with a much larger flux of oceanic DIC resulting in authigenic carbonate with a carbon isotope composition that approximates that of normal seawater [Saitoh et al., 2015].

Utilizing the results from this study, a quantitative estimate of the isotopic response to authigenic carbonate burial can be made using the equation for isotope mass balance from [Schrag et al., 2013]:

$$\delta^{13}C_{DIC} = \delta^{13}C_{in} + f_{org}[\epsilon_p - \epsilon_{mc} - f_{ac}(\epsilon_{ac} - \epsilon_{mc})] + f_{ac}(\epsilon_{ac} - \epsilon_{mc}) \qquad (5.1)$$

where $\delta^{13}C_{DIC}$ and $\delta^{13}C_{in}$ represent the carbon isotope composition of dissolved inorganic carbon and the weathering flux, respectively, and f_{org} and f_{ac} represent the

fraction of organic carbon burial (relative to total carbon burial) and authigenic carbonate burial (relative to total carbonate burial), respectively. Epsilon values represent the various fractionation factors (p: photosynthetic isotope effect; mc: marine carbonate relative to seawater; and ac: authigenic carbonate relative to seawater). Using the average authigenic carbonate content found in mudrocks from this study (4.6% $CaCO_3$, converted from weight percent inorganic carbon) and an average terrigenous sediment flux (1.7×10^{16} g/year, [Schrag et al., 2013]), the burial flux of authigenic carbonate (F_{ac}) can be determined as a function of what proportion of terrigenous sediment is deposited as calcareous shale. Assuming values for the burial flux of carbonate (F_{carb}) [Kump and Arthur, 1999], the fraction of authigenic burial can be determined:

$$f_{ac} = \frac{F_{ac}}{F_{carb} + F_{ac}} \tag{5.2}$$

For ϵ_{ac}, this fractionation factor between authigenic carbonate and marine DIC is calculated from the difference between mean δ^{13}C of the basin (presumed to be authigenic) with mean δ^{13}C of platform carbonates (representative of marine carbonates):

$$\epsilon_{ac} = \epsilon_{mc} - (\delta^{13}C_{basin} - \delta^{13}C_{platform}) \tag{5.3}$$

With both values for f_{ac} and ϵ_{ac} determined, a model is produced to illustrate the effect authigenic carbonate burial, based on data from the WCSB, had on δ^{13}C DIC (Figure 5.7). Model results illustrate that as the fraction of authigenic carbonate burial (f_{ac}) increases (represented by an increase in the proportion of calcareous shale deposition), δ^{13}C DIC decreases. This result occurs because the empirically-determined fractionation factor between authigenic carbonate and marine DIC (ϵ_{ac} = -1.15‰) is not large, and similar to the fractionation factor between marine carbonate and organic matter carbon (ϵ_{mc}). Thus, the fraction of organic carbon burial (f_{org}) remains the most significant control on δ^{13}C DIC. Furthermore, because of the sign of the fractionation factor, an increase in the burial flux of authigenic carbonate will result in δ^{13}C DIC that is lower (because f_{org} is decreased as organic carbon is converted to authigenic carbonate). In this way, an increase in the burial of authigenic carbonate can be considered equivalent essentially to an increase in the burial of marine carbonate.

However, if calcareous shale deposition were to increase, would f_{org} actually go down, as implied by the blue line in Figure 5.7? To address this question, the ratio of organic

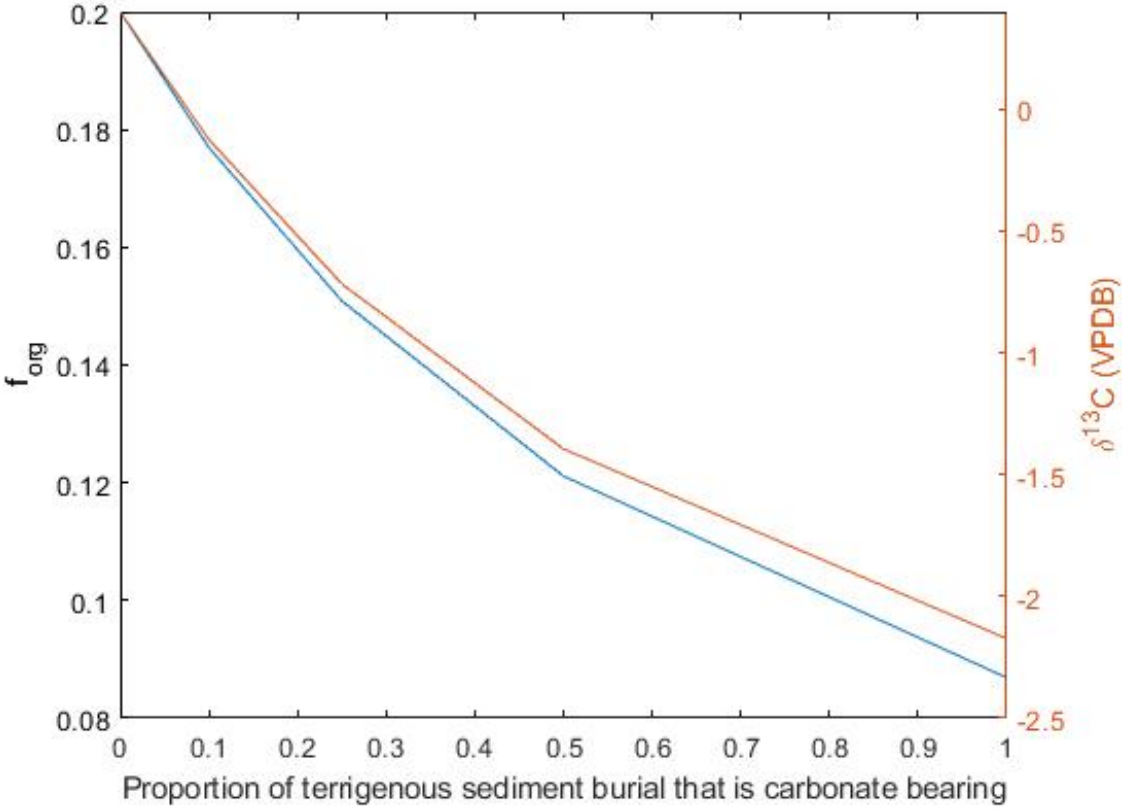

Figure 5.7: The effect of authigenic carbonate burial on $\delta^{13}C_{DIC}$. The blue line illustrates that with increasing proportion of calcareous shale deposition (i.e. f_{ac}), the fraction of organic carbon burial (f_{org}) decreases. Simultaneously, as the proportion of shale deposition increases, $\delta^{13}C$ decreases as well (red line). Model results clearly illustrate that the burial of authigenic carbonate has no enrichment effect on $\delta^{13}C$ - in fact, the opposite is predicted. Model parameters found in Appendix C.

carbon (OC) to inorganic carbon (IC) in shales is instructive. While organic carbon content was not measured in samples for this study, OC:IC calculated from North American shales across the geologic record and the Late Devonian tend to have ratios greater than 1 (Figure 5.8). Average values (calculated as average (OC) / average (IC)), are 3.72 for Late Devonian shales and 2.25 for all other shales in the USGS database. An important implication of the OC:IC ratios is that an increase in shale deposition most notably increases the burial flux of organic carbon, compared to any burial of authigenic carbon. This implication contradicts model results (Figure 5.7) which state that the fraction of organic carbon buried (f_{org}) will decrease as calcareous shale deposition increases. These data suggest that despite the presence of an authigenic sink, shales predominantly bury organic carbon - even in Late Devonian shales, which despite showing a very slight increase in carbonate content (2.12 % inorganic C vs. 1.95%) have a higher OC/IC ratio compared to the long-term average (3.72 vs. 2.25).

Findings from this study also present an intriguing possibility with respect to the effect of diagenetic alteration of carbonate rocks on δ^{13}C DIC. Results from Gulf Mohawk (Figure 4.26) illustrate significant decrease in δ^{13}C values. This depletion in ^{13}C has been attributed, herein, to organic matter respiration and increased water-mass residence times in a restricted marginal marine setting [Patterson and Walter, 1994]. In this scenario, the carbon budget within a water mass that is cut-off from regular sea water is affected strongly by organic matter respiration. This oxidation of organic matter releases CO_2 with low δ^{13}C values into the water column. The carbonate that is precipitated out of this ^{13}C depleted sea water will record a low δ^{13}C value such as the ones observed at Gulf Mohawk [Lloyd, 1964, Patterson and Walter, 1994]. Could significant amounts of low δ^{13}C carbonates deposited in restricted basins sufficiently drive δ^{13}C DIC positive excursions? To explore this hypothesis, a model was generated by re-utilizing the same mass balance equation used above (equation 5.1) with the replacement of the authigenic sink (f_{ac}, ϵ_{ac}) with a sink for oxidized carbon matter incorporated into carbonates (referred to as the "oxidized carbon" carbonate sink, as described by f_{ox} and ϵ_{ox}), (Figure 5.9).

$$\delta^{13}C_{DIC} = \delta^{13}C_{in} + f_{org}[\epsilon_p - \epsilon_{mc} - f_{ox}(\epsilon_{ox} - \epsilon_{mc})] + f_{ox}(\epsilon_{ox} - \epsilon_{mc}) \tag{5.4}$$

The proportion f_{ox} was given as a range from 0 to 1 of total carbonate burial. The

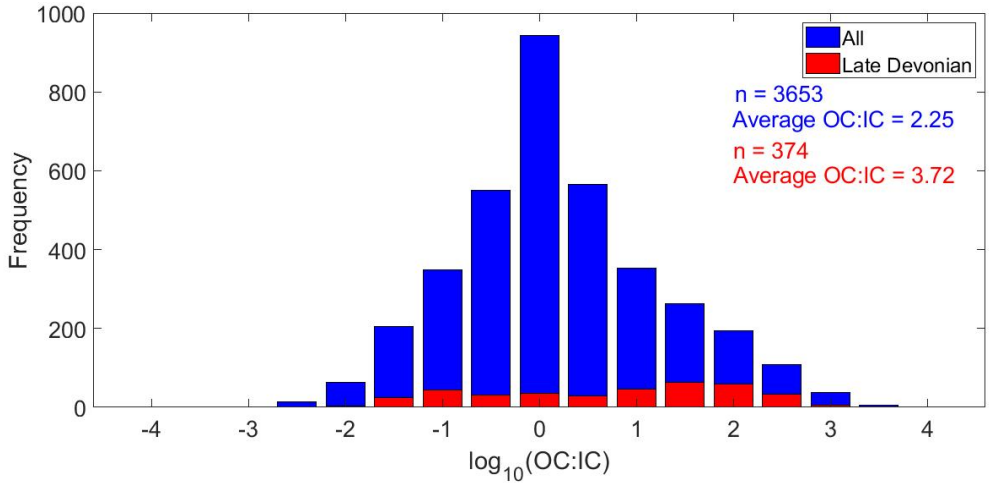

Figure 5.8: Histogram of organic carbon (OC) content relative to inorganic carbon (IC) in shales. "All" refers to shales from the USGS database [USGS, 2008] and excludes Late Devonian shale formations. Late Devonian shales are also from the USGS database [USGS, 2008]. Average values are calculated as average (OC) / average (IC). Note that certain samples did not have data for both organic carbon wt% and inorganic carbon wt%, thus resulting in sample counts which are lower than Figure 5.6.

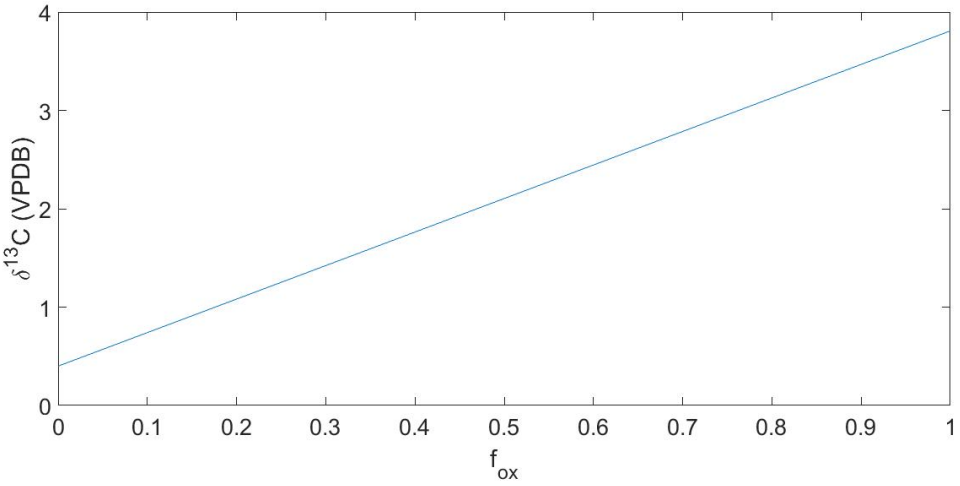

Figure 5.9: $\delta^{13}C_{DIC}$ as a function of f_{ox}. With expansion of the "oxidized carbon" carbonate sink, model results show ^{13}C enrichment of the DIC reservoir. f_{org} is held constant at modern values (0.2).

fractionation factor (ϵ_{ox}) was calculated in a similar way to ϵ_{ac}; however, it considers the difference between platform δ^{13}C and δ^{13}C from the restricted inner platform. Model results clearly demonstrate that increased sequestration of these low δ^{13}C carbonates would be able to generate excursions as high as nearly 4‰. While model results confirm the plausibility of the oxidized sink in driving δ^{13}C DIC excursions, how prominent would it have been throughout geological history?

The oxidized carbon carbonate sink cannot be reconciled with positive Precambrian excursions because this sink relies on surface oxidants, and abundant organic matter in restricted marginal marine-terrestrial settings, which may not have been realized until the establishment of land plants [Jones et al., 2015]. Furthermore, as the model shows, a scenario in which all carbonate is buried as oxidized carbon carbonate ($f_{ox} = 1$) would not drive $\delta^{13}C_{DIC}$ to high enough excursions as those observed in the Proterozoic on its own (e.g. >10‰). However, high values of f_{ox} might explain Phanerozoic excursions when O_2 levels were higher. The prominence of an oxidized carbon carbonate sink would also be greater in times of eustatic sea-level fall, thereby expanding the area and occurrence of restricted marine environments and allowing for a greater amount of oxidized carbon carbonate to be buried. The influence of the oxidized carbon carbonate sink may also be compounded by the addition of ^{13}C-depleted carbonate cements resulting from meteoric diagenesis. Previous modelling efforts have demonstrated that the increased weathering of carbonates from meteoric fluids, during eustatic sea-level fall, could acts as an important sink of ^{13}C-depleted carbon [Dyer et al., 2015]. It is therefore recommended that further investigation be carried out targeting excursions known to be associated with eustatic lowstands to verify the viability of this proposed carbon sink.

The authigenic hypothesis [Schrag et al., 2013] was based partly on observations of modern authigenic carbonate with low δ^{13}C values. Studies from modern seafloor sediments have supported the plausibility of authigenic carbonate as a sink for carbon [Sun and Turchyn, 2014, Mitnick et al., 2018, Bradbury and Turchyn, 2019], though relegated to coastal settings where the delivery of organic matter is high, and with bacterial processes being primarily regulated by methane oxidation rather than sulfate. While the Late Devonian may have been a period of high authigenic carbonate burial, this study demonstrates that the influence of authigenic carbonate on the carbon isotope composition of the global DIC pool was minimal. It would also

seem that $\delta^{13}C$ response to authigenesis can be easily overprinted by local factors, as evidenced by potential methanogenesis occurring within the Exshaw (Figure 4.20) or increased oxidation within restricted depositional settings (Figure 4.26). Thus, caution must be taken when interpreting global trends in the marine carbon cycle. A combination of local depositional, diagenetic factors and specialized oceanographic conditions, may obscure the actual cause of isotope excursions in deep time.

Chapter 6

Conclusions

The focus of this research is to test whether the burial of authigenic carbonate within marine siliciclastic formations could produce large carbon isotope excursions, observed in the geologic record. Authigenic carbonate is hypothesized to precipitate in anoxic conditions within sediment pore spaces or at the sediment-water interface, with alkalinity produced by sulfate reducing anaerobic bacteria resulting in carbonate that have low δ^{13}C values. The sustained burial of ^{13}C depleted carbonate is predicted to enrich $\delta^{13}C_{DIC}$, a signal that would be preserved in coeval platformal carbonates. Though present in today's environment, it is assumed to be more prevalent during geologic time intervals characterized by low atmospheric O_2.

This case study investigated platform carbonates and basinal shales of Late Devonian age. The Late Devonian is characterized by globally pervasive ocean anoxia and a crash in global carbonate depositional systems that coincided with a drowning of epeiric carbonate platforms - conditions which may have been ideal for the establishment of a authigenic carbonate sink quantitatively important to the global carbon cycle. Sedimentary formations of this age are found within the WCSB. Consideration of the authigenic sink hypothesis in light of newly acquired geochemical and sedimentological data has led to the following conclusions:

1. Depositional facies within the the WCSB are highly variable, with each depositional environment displaying a unique set of sedimentary characteristics. The deep basin is represented by siltstones and black shales of the Besa River and Exshaw formations. Authigenic carbonate is present in the form of macroscopic concretions and laminations and disseminated carbonate crystals, visible

in thin section. The abundance of pyrite, including framboidal pyrite, suggests a record of sulfate-reducing microbial activity. The outer carbonate platform is represented by slope lithofacies of the mixed siliciclastic-carbonate Sassenach Formation and overlying, platform lithofacies of the open marine Palliser Formation. The inner platform is characterized by a facies change from peritidal to subtidal/open marine carbonates interpreted as a deepening upward succession. The proximal inner platform, represented by section Gulf Mohawk, represents an evaporitive restricted marine setting. Petrographic evidence suggest extensive recrystallization and dolomitization at this location.

2. Average wt% inorganic carbon within mudrocks was measured to not be elevated relative to average shale composition (0.55% relative to 1.95%, Figure 5.5 and 5.6). However, a compilation of inorganic carbon data from Late Devonian black shales (including samples from this study) were found to be elevated relative to average shale composition from North American mudrocks across geologic history, though not statistically significant (Late Devonian = 2.12%, 2 S.E. = 0.30; Average shale = 1.95%, 2 S.E. = 0.08). Furthermore, the OC/IC ratio is higher for the Late Devonian compared to average shale (Figure 5.8, 3.25 vs. 2.25) implies that Late Devonian shales predominantly buried organic carbon rather than authigenic carbonate.

3. Low values of δ^{13}C were not observed in authigenic carbonates in the basinal facies, and δ^{13}C values of platformal carbonates were found to be within the accepted range for Devonian (and modern) seawater, suggesting that authigenic carbonate bearing siliciclastic formations are insufficiently depleted to influence the marine DIC carbon isotope signal.

4. Carbonate cements were observed in the restricted inner platform setting. Low values of δ^{13}C have been attributed to increased rates of respired organic matter in the water column. It is plausible that an increase in burial of low δ^{13}C carbonates within restricted marine basins may act as a lever on seawater isotope composition. This proposed carbon sink may have been prevalent during times of eustatic lowstands where large areas of the continental shelf become exposed or cut-off from seawater circulation.

The sedimentological and geochemical results presented herein suggest that despite environmental conditions encouraging the precipitation of authigenic carbonates

within basinal siltstone and shale formations, the authigenic sink did not have a pronounced effect on carbon isotope mass-balance during the Late Devonian. Authigenic carbonates recording normal seawater $\delta^{13}C$ values imply porewater mixing with a larger DIC pool which would have occurred at or near the sediment-water interface. It is further interesting to note that these findings are in contrast to $\delta^{13}C$ values from authigenic carbonates precipitated on the modern seafloor which can be highly depleted in ^{13}C despite occurring in relatively more oxygenated oceans [Mitnick et al., 2018]. This implies that conditions that enable the precipitation of authigenic carbonate are diverse and as a result so might their $\delta^{13}C$ values. Thus, the authigenic sink cannot necessarily be discounted as an explanation for Precambrian carbon isotope excursions but rather thorough investigation must done on a "case-by-case" basis to ascertain oceanographic conditions to accurately judge the carbon isotope response to authigenic carbonate deposition.

The conclusions extrapolated from this work can be further refined by expanding geochemical datasets to other locations to attempt interbasinal correlations to better judge the global response to authigenic carbonate deposition. Further testing of this hypothesis would also be aided by techniques that can more precisely measure the global flux of authigenic carbonate precipitation within marine siliciclastic formations. Accurate and precise measurement of the authigenic flux can be supported by the use of novel geochemical proxys for authigenesis such as the measurement of uranium concentrations which is thought to be elevated in zones of active sulphate reduction [Zhao et al., 2016]. The production of more refined seawater mixing models is also necessitated to evaluate the relative proportions of DIC and ^{13}C depleted porewaters required to drive observed carbon isotope excursions. Finally, the presence of low $\delta^{13}C$ buried in restricted marine settings warrants more investigation. Case studies from moments in Earth History defined by exceptionally low global sea-levels (such as the late Mississippian and late Permian) may provide evidence that an expanded oxidized carbon carbonate sink had an influence on carbon isotope excursions.

Bibliography

[Algeo et al., 1995] Algeo, T. J., Berner, R. A., Maynard, J. B., Scheckler, S. E., et al. (1995). Late Devonian oceanic anoxic events and biotic crises:"rooted" in the evolution of vascular land plants. *GSA today*, 5(3):45–66.

[Allan and Matthews, 1982] Allan, J. and Matthews, R. (1982). Isotope signatures associated with early meteoric diagenesis. *Sedimentology*, 29(6):797–817.

[Allen et al., 2014] Allen, M. R., Barros, V. R., Broome, J., Cramer, W., Christ, R., Church, J. A., Clarke, L., Dahe, Q., Dasgupta, P., Dubash, N. K., et al. (2014). Ipcc fifth assessment synthesis report-climate change 2014 synthesis report. *Intergovernmental Panel on Climate Change: Geneva, Switzerland*.

[Amorosi, 2012] Amorosi, A. (2012). The occurrence of glaucony in the stratigraphic record: distribution patterns and sequence-stratigraphic significance. *International Association of Sedimentologists Special Publications*, 45:37–54.

[Anderson and Arthur, 1983] Anderson, T. F. and Arthur, M. A. (1983). Stable isotopes of oxygen and carbon and their application to sedimentologic and paleoenvironmental problems. *Stable Isotopes in Sedimentary Geology*, 10:1–151.

[Andrichuk, 1960] Andrichuk, J. M. (1960). Facies analysis of Upper Devonian Wabamun group in west-central Alberta, Canada. *AAPG Bulletin*, 44(10):1651–1681.

[Bambach et al., 2004] Bambach, R. K., Knoll, A. H., and Wang, S. C. (2004). Origination, extinction, and mass depletions of marine diversity. *Paleobiology*, 30(4):522–542.

[Banerjee et al., 2016] Banerjee, S., Bansal, U., and Thorat, A. V. (2016). A review on palaeogeographic implications and temporal variation in glaucony composition. *Journal of Palaeogeography*, 5(1):43–71.

[Banner and Hanson, 1990] Banner, J. L. and Hanson, G. N. (1990). Calculation of simultaneous isotopic and trace element variations during water-rock interaction with applications to carbonate diagenesis. *Geochimica et Cosmochimica Acta*, 54(11):3123–3137.

[Barnes et al., 2019] Barnes, B. D., Husson, J. M., and Peters, S. E. (2019). Authigenic Carbonate Burial in the Late Devonian–Early Mississippian Bakken Formation (Williston Basin, USA). *Sedimentology*, 67(4):2065–2094.

[Becker et al., 2016] Becker, R. T., Kaiser, S. I., and Aretz, M. (2016). Review of chrono-, litho-and biostratigraphy across the global Hangenberg Crisis and Devonian–Carboniferous Boundary. *Geological Society, London, Special Publications*, 423(1):355–386.

[Becker, 1997] Becker, S. (1997). *Depositional Environments, Provenance and Sequence Stratigraphy of the Type Sassenach Formation, Jasper, Alberta*. PhD thesis, McGill University Libraries.

[Bergman et al., 2004] Bergman, N. M., Lenton, T. M., and Watson, A. J. (2004). COPSE: a new model of biogeochemical cycling over Phanerozoic time. *American Journal of Science*, 304(5):397–437.

[Bernard et al., 2017] Bernard, S., Daval, D., Ackerer, P., Pont, S., and Meibom, A. (2017). Burial-induced oxygen-isotope re-equilibration of fossil foraminifera explains ocean paleotemperature paradoxes. *Nature communications*, 8(1):1–10.

[Berner et al., 2000] Berner, R., Petsch, S., Lake, J., Beerling, D., Popp, B., Lane, R., Laws, E., Westley, M., Cassar, N., Woodward, F., et al. (2000). Isotope fractionation and atmospheric oxygen: implications for Phanerozoic O_2 evolution. *Science*, 287(5458):1630–1633.

[Berner, 1998] Berner, R. A. (1998). The carbon cycle and carbon dioxide over Phanerozoic time: the role of land plants. *Philosophical Transactions of the Royal Society of London. Series B: Biological Sciences*, 353(1365):75–82.

[Berner, 2006] Berner, R. A. (2006). GEOCARBSULF: a combined model for Phanerozoic atmospheric O2 and CO2. *Geochimica et Cosmochimica Acta*, 70(23):5653–5664.

[Berner and Kothavala, 2001] Berner, R. A. and Kothavala, Z. (2001). GEOCARB III: a revised model of atmospheric CO_2 over Phanerozoic time. *American Journal of Science*, 301(2):182–204.

[Berner et al., 1970] Berner, R. A., Scott, M. R., and Thomlinson, C. (1970). Carbonate Alkalinity in the Pore Waters of Anoxic Marine Sediments 1. *Limnology and Oceanography*, 15(4):544–549.

[Bjerrum and Canfield, 2004] Bjerrum, C. J. and Canfield, D. E. (2004). New insights into the burial history of organic carbon on the early Earth. *Geochemistry, Geophysics, Geosystems*, 5(8).

[Bond and Wignall, 2008] Bond, D. P. and Wignall, P. B. (2008). The role of sea-level change and marine anoxia in the Frasnian–Famennian (Late Devonian) mass extinction. *Palaeogeography, Palaeoclimatology, Palaeoecology*, 263(3-4):107–118.

[Bradbury and Turchyn, 2019] Bradbury, H. J. and Turchyn, A. V. (2019). Reevaluating the carbon sink due to sedimentary carbonate formation in modern marine sediments. *Earth and Planetary Science Letters*, 519:40–49.

[Brasier and Shields, 2000] Brasier, M. and Shields, G. (2000). Neoproterozoic chemostratigraphy and correlation of the Port Askaig glaciation, Dalradian Supergroup of Scotland. *Journal of the Geological Society*, 157(5):909–914.

[Brasier et al., 1996] Brasier, M., Shields, G., Kuleshov, V., and Zhegallo, E. (1996). Integrated chemo-and biostratigraphic calibration of early animal evolution: Neoproterozoic–early Cambrian of southwest Mongolia. *Geological Magazine*, 133(4):445–485.

[Burns and Matter, 1993] Burns, S. and Matter, A. (1993). Carbon isotopic record of the latest Proterozoic from Oman. *Eclogae Geologicae Helvetiae*, 86(2):595–607.

[Caplan and Bustin, 1999] Caplan, M. L. and Bustin, R. M. (1999). Devonian–Carboniferous Hangenberg mass extinction event, widespread organic-rich mudrock and anoxia: causes and consequences. *Palaeogeography, Palaeoclimatology, Palaeoecology*, 148(4):187–207.

[Catling and Claire, 2005] Catling, D. C. and Claire, M. W. (2005). How Earth's atmosphere evolved to an oxic state: a status report. *Earth and Planetary Science Letters*, 237(1-2):1–20.

[Claeys et al., 1992] Claeys, P., Casier, J.-G., and Margolis, S. V. (1992). Microtektites and mass extinctions: evidence for a Late Devonian asteroid impact. *Science*, 257(5073):1102–1104.

[Claypool and Kaplan, 1974] Claypool, G. E. and Kaplan, I. (1974). The origin and distribution of methane in marine sediments. In *Natural gases in marine sediments*, pages 99–139. Springer.

[Cole et al., 2015] Cole, D., Myrow, P., Fike, D., Hakim, A., and Gehrels, G. E. (2015). Uppermost Devonian (Famennian) to Lower Mississippian events of the western US: Stratigraphy, sedimentology, chemostratigraphy, and detrital zircon geochronology. *Palaeogeography, Palaeoclimatology, Palaeoecology*, 427:1–19.

[Coleman and Raiswell, 1993] Coleman, M. and Raiswell, R. (1993). Microbial mineralization of organic matter: mechanisms of self-organization and inferred rates of precipitation of diagenetic minerals. *Philosophical Transactions of the Royal Society of London. Series A: Physical and Engineering Sciences*, 344(1670):69–87.

[Colpron and Nelson, 2009] Colpron, M. and Nelson, J. L. (2009). A Palaeozoic Northwest Passage: Incursion of Caledonian, Baltican and Siberian terranes into eastern Panthalassa, and the early evolution of the North American Cordillera. *Geological Society, London, Special Publications*, 318(1):273–307.

[Copper, 1994] Copper, P. (1994). Ancient reef ecosystem expansion and collapse. *Coral Reefs*, 13(1):3–11.

[Copper, 2002] Copper, P. (2002). Reef development at the Frasnian/Famennian mass extinction boundary. *Palaeogeography, Palaeoclimatology, Palaeoecology*, 181(1-3):27–65.

[Copper and Scotese, 2003] Copper, P. and Scotese, C. R. (2003). Megareefs in Middle Devonian supergreenhouse climates. *Special Papers-Geological Society of America*, pages 209–230.

[Craig et al., 1965] Craig, H., Gordon, L. I., et al. (1965). Deuterium and oxygen 18 variations in the ocean and the marine atmosphere. pages 277–374. Consiglio nazionale delle richerche, Laboratorio de geologia nucleare Pisa.

[Cramer et al., 2008] Cramer, B. D., Saltzman, M. R., Day, J. E., and Witzke, B. J. (2008). Record of the Late Devonian Hangenberg global positive carbon-isotope excursion in an epeiric sea setting: carbonate production, organic-carbon burial and paleoceanography during the Late Famennian. In *Special Paper - Geological Association of Canada*, volume 48, pages 103–118.

[Curtis, 1987] Curtis, C. (1987). Mineralogical consequences of organic matter degradation in sediments: inorganic/organic diagenesis. In *Marine Clastic Sedimentology*, pages 108–123. Springer.

[Dahl and Arens, 2020] Dahl, T. W. and Arens, S. K. (2020). The impacts of land plant evolution on Earth's climate and oxygenation state–An interdisciplinary review. *Chemical Geology*, 547:119665.

[Deines, 1980] Deines, P. (1980). The isotopic composition of reduced organic carbon. In Fritz, A. P. and Fontes, J. C., editors, *Handbook of Environmental Isotope Geochemistry*, volume 1, pages 329–406. Elsevier, Amsterdam.

[deWitt and McLaren, 1950] deWitt, R. and McLaren, D. (1950). Devonian sections in the Rocky Mountain's between Crowsnest Pass and Jasper, Alberta: Geol. Surv. Canada, Paper 50-23. *Miette Platform Evolution*, 409.

[Dix, 1990] Dix, G. R. (1990). Stages of platform development in the Upper Devonian (Frasnian) Leduc Formation, Peace River Arch, Alberta. *Bulletin of Canadian Petroleum Geology*, 38(1):66–92.

[Dunham, 1962] Dunham, R. J. (1962). Classification of carbonate rocks according to depositional textures. In *Classification of Carbonate Rocks*, pages 108–121. AAPG Special Volumes.

[Dyer et al., 2015] Dyer, B., Maloof, A. C., and Higgins, J. A. (2015). Glacioeustasy, meteoric diagenesis, and the carbon cycle during the Middle Carboniferous. *Geochemistry, Geophysics, Geosystems*, 16(10):3383–3399.

[Emerson et al., 1997] Emerson, S., Quay, P., Karl, D., Winn, C., Tupas, L., and Landry, M. (1997). Experimental determination of the organic carbon flux from open-ocean surface waters. *Nature*, 389(6654):951.

[Emerson and Hedges, 2008] Emerson, S. R. and Hedges, J. (2008). The global carbon cycle: interactions between the atmosphere and ocean. In *Chemical oceanography and the marine carbon cycle*. Cambridge University Press, New York.

[Epstein et al., 1951] Epstein, S., Buchsbaum, R., Lowenstam, H., and Urey, H. C. (1951). Carbonate-water isotopic temperature scale. *Geological Society of America Bulletin*, 62(4):417–426.

[Fagerstrom, 1994] Fagerstrom, J. A. (1994). The history of Devonian-Carboniferous reef communities: extinctions, effects, recovery. *Facies*, 30(1):177–191.

[Fairbanks et al., 1997] Fairbanks, R., Evans, M., Rubenstone, J., Mortlock, R., Broad, K., Moore, M., and Charles, C. (1997). Evaluating climate indices and their geochemical proxies measured in corals. *Coral Reefs*, 16(1):S93–S100.

[Ferri et al., 2011] Ferri, F., Hickin, A. S., and Huntley, D. H. (2011). Besa River Formation, western Liard Basin, British Columbia (NTS 094N): geochemistry and regional correlations. *Geoscience Reports*, pages 1–18.

[Ferri et al., 2012] Ferri, F., Hickin, A. S., and Reyes, J. (2012). Horn river basin–equivalent strata in Besa River Formation shale, northeastern British Columbia (NTS 094K/15). *Geoscience Reports*, pages 1–15.

[Fike et al., 2006] Fike, D., Grotzinger, J., Pratt, L., and Summons, R. (2006). Oxidation of the Ediacaran ocean. *Nature*, 444(7120):744.

[Filipiak and Racki, 2010] Filipiak, P. and Racki, G. (2010). Proliferation of abnormal palynoflora during the end-Devonian biotic crisis. *Geological Quarterly*, 54(1):1–14.

[Flowers et al., 2012] Flowers, R. M., Ault, A. K., Kelley, S. A., Zhang, N., and Zhong, S. (2012). Epeirogeny or eustasy? Paleozoic–Mesozoic vertical motion of the North American continental interior from thermochronometry and implications for mantle dynamics. *Earth and Planetary Science Letters*, 317:436–445.

[Freeman and Hayes, 1992] Freeman, K. H. and Hayes, J. (1992). Fractionation of carbon isotopes by phytoplankton and estimates of ancient CO_2 levels. *Global Biogeochemical Cycles*, 6(2):185–198.

[Fuller and Porter, 1969] Fuller, J. and Porter, J. (1969). Evaporite formations with petroleum reservoirs in Devonian and Mississippian of Alberta, Saskatchewan, and North Dakota. *AAPG Bulletin*, 53(4):909–926.

[Gaines and Vorhies, 2016] Gaines, R. R. and Vorhies, J. S. (2016). Growth mechanisms and geochemistry of carbonate concretions from the Cambrian Wheeler Formation (Utah, USA). *Sedimentology*, 63(3):662–698.

[Garzione et al., 1997] Garzione, C. N., Patchett, P. J., Ross, G. M., and Nelson, J. (1997). Provenance of Paleozoic sedimentary rocks in the Canadian Cordilleran miogeocline: a Nd isotopic study. *Canadian Journal of Earth Sciences*, 34(12):1603–1618.

[Gehrels and Pecha, 2014] Gehrels, G. and Pecha, M. (2014). Detrital zircon U-Pb geochronology and Hf isotope geochemistry of Paleozoic and Triassic passive margin strata of western North America. *Geosphere*, 10(1):49–65.

[Geyman and Maloof, 2019] Geyman, E. C. and Maloof, A. C. (2019). A diurnal carbon engine explains ^{13}C-enriched carbonates without increasing the global production of oxygen. *Proceedings of the National Academy of Sciences*, 116(49):24433–24439.

[Golonka, 2020] Golonka, J. (2020). Late Devonian paleogeography in the framework of global plate tectonics. *Global and Planetary Change*, 186:103129.

[Grotzinger et al., 2011] Grotzinger, J. P., Fike, D. A., and Fischer, W. W. (2011). Enigmatic origin of the largest-known carbon isotope excursion in Earth's history. *Nature Geoscience*, 4(5):285.

[Grotzinger and James, 2000] Grotzinger, J. P. and James, N. P. (2000). Precambrian Carbonates: Evolution of Understanding. In *Carbonate Sedimentation and Diagenesis in the Evolving Precambrian World*. SEPM Society for Sedimentary Geology.

[Grotzinger and Knoll, 1995] Grotzinger, J. P. and Knoll, A. H. (1995). Anomalous carbonate precipitates: is the Precambrian the key to the Permian? *Palaios*, pages 578–596.

[Halbertsma and Meijer-Drees, 1987] Halbertsma, H. and Meijer-Drees, N. (1987). Wabamun limestone sequences in north-central Alberta. In *Devonian Lithofacies and Reservoir Styles in Alberta.*, pages 21–37. CSPG Special Publications.

[Halbertsma et al., 1994] Halbertsma, H., Mossop, G., Shetsen, I., et al. (1994). Devonian Wabamun Group of the western Canada sedimentary basin. *Geological Atlas of the Western Canada Sedimentary Basin*, 4:203–220.

[Hallock and Schlager, 1986] Hallock, P. and Schlager, W. (1986). Nutrient excess and the demise of coral reefs and carbonate platforms. *Palaios*, pages 389–398.

[Halverson et al., 2005] Halverson, G. P., Hoffman, P. F., Schrag, D. P., Maloof, A. C., and Rice, A. H. N. (2005). Toward a Neoproterozoic composite carbon-isotope record. *GSA Bulletin*, 117(9-10):1181–1207.

[Halverson and Hurtgen, 2007] Halverson, G. P. and Hurtgen, M. T. (2007). Ediacaran growth of the marine sulfate reservoir. *Earth and Planetary Science Letters*, 263(1-2):32–44.

[Halverson et al., 2004] Halverson, G. P., Maloof, A. C., and Hoffman, P. F. (2004). The Marinoan glaciation (Neoproterozoic) in northeast Svalbard. *Basin Research*, 16(3):297–324.

[Haq and Schutter, 2008] Haq, B. U. and Schutter, S. R. (2008). A chronology of Paleozoic sea-level changes. *Science*, 322(5898):64–68.

[Harde, 2017] Harde, H. (2017). Scrutinizing the carbon cycle and CO_2 residence time in the atmosphere. *Global and Planetary Change*, 152:19–26.

[Hardebol et al., 2012] Hardebol, N. J., Pysklywec, R., and Stephenson, R. (2012). Small-scale convection at a continental back-arc to craton transition: Application to the southern Canadian Cordillera. *Journal of Geophysical Research: Solid Earth*, 117(B1).

[Harris and Whiting, 2000] Harris, L. and Whiting, B. (2000). Sequence-stratigraphic significance of Miocene to Pliocene glauconite-rich layers, on-and offshore of the US Mid-Atlantic margin. *Sedimentary Geology*, 134(1-2):129–147.

[Hartenfels and Becker, 2009] Hartenfels, S. and Becker, R. T. (2009). Timing of the global Dasberg Crisis–implications for Famennian eustasy and chronostratigraphy. *Palaeontographica Americana*, 63:71–97.

[Hauck et al., 2017] Hauck, T. E., Pană, D., and DuFrane, S. A. (2017). Northern Laurentian provenance for Famennian clastics of the Jasper basin (Alberta, Canada): A Sm-Nd and U-Pb detrital zircon study. *Geosphere*, 13(4):1149–1172.

[Hayes and Waldbauer, 2006] Hayes, J. M. and Waldbauer, J. R. (2006). The carbon cycle and associated redox processes through time. *Philosophical Transactions of the Royal Society B: Biological Sciences*, 361(1470):931–950.

[Higgins et al., 2009] Higgins, J. A., Fischer, W., and Schrag, D. (2009). Oxygenation of the ocean and sediments: consequences for the seafloor carbonate factory. *Earth and Planetary Science Letters*, 284(1-2):25–33.

[Hoffman and Schrag, 2002] Hoffman, P. F. and Schrag, D. P. (2002). The snowball Earth hypothesis: testing the limits of global change. *Terra nova*, 14(3):129–155.

[Hudson, 1977] Hudson, J. (1977). Stable isotopes and limestone lithification. *Journal of the Geological Society*, 133(6):637–660.

[Husson et al., 2012] Husson, J. M., Maloof, A. C., and Schoene, B. (2012). A syndepositional age for Earth's deepest $\delta^{13}C$ excursion required by isotope conglomerate tests. *Terra Nova*, 24(4):318–325.

[Irwin et al., 1977] Irwin, H., Curtis, C., and Coleman, M. (1977). Isotopic evidence for source of diagenetic carbonates formed during burial of organic-rich sediments. *Nature*, 269(5625):209–213.

[Isaacson et al., 2008] Isaacson, P., Díaz-Martínez, E., Grader, G., Kalvoda, J., Babek, O., and Devuyst, F. (2008). Late Devonian–earliest Mississippian glaciation in Gondwanaland and its biogeographic consequences. *Palaeogeography, Palaeoclimatology, Palaeoecology*, 268(3-4):126–142.

[Ishikawa et al., 2008] Ishikawa, T., Ueno, Y., Komiya, T., Sawaki, Y., Han, J., Shu, D., Li, Y., Maruyama, S., and Yoshida, N. (2008). Carbon isotope chemostratigraphy of a Precambrian/Cambrian boundary section in the Three Gorge area, South China: prominent global-scale isotope excursions just before the Cambrian Explosion. *Gondwana Research*, 14(1-2):193–208.

[Johnson, 1970] Johnson, J. (1970). Taghanic onlap and the end of North American Devonian provinciality. *Geological Society of America Bulletin*, 81(7):2077–2106.

[Johnson et al., 1985] Johnson, J., Klapper, G., and Sandberg, C. A. (1985). Devonian eustatic fluctuations in Euramerica. *Geological Society of America Bulletin*, 96(5):567–587.

[Johnston et al., 2010] Johnston, D. I., Henderson, C. M., and Schmidt, M. J. (2010). Upper Devonian to Lower Mississippian conodont biostratigraphy of uppermost Wabamun Group and Palliser Formation to lowermost Banff and Lodgepole formations, southern Alberta and southeastern British Columbia, Canada: implications for correlations and sequence stratigraphy. *Bulletin of Canadian Petroleum Geology*, 58(4):295–341.

[Johnston et al., 2012] Johnston, D. T., Macdonald, F. A., Gill, B., Hoffman, P., and Schrag, D. P. (2012). Uncovering the Neoproterozoic carbon cycle. *Nature*, 483(7389):320.

[Jones et al., 2020] Jones, D. S., Brothers, R. W., Crüger Ahm, A.-S., Slater, N., Higgins, J. A., and Fike, D. A. (2020). Sea level, carbonate mineralogy, and early diagenesis controlled $\delta^{13}C$ records in Upper Ordovician carbonates. *Geology*, 48(2):194–199.

[Jones et al., 2015] Jones, D. S., Creel, R. C., Rios, B., and Santiago Ramos, D. P. (2015). Chemostratigraphy of an ordovician–silurian carbonate platform: δ13c records below glacioeustatic exposure surfaces. *Geology*, 43(1):59–62.

[Kabanov et al., 2019] Kabanov, P., Richards, B. C., Lee, H. S., Thapa, P., King, H. M., and Mort, A. (2019). Reference surface and subsurface sections of the Besa River Formation, Liard Basin, British Columbia. Technical report, Natural Resources Canada.

[Kaiser et al., 2016] Kaiser, S. I., Aretz, M., and Becker, R. T. (2016). The global Hangenberg Crisis (Devonian–Carboniferous transition): review of a first-order mass extinction. *Geological Society, London, Special Publications*, 423(1):387–437.

[Kaiser et al., 2006] Kaiser, S. I., Steuber, T., Becker, R. T., and Joachimski, M. M. (2006). Geochemical evidence for major environmental change at the Devonian–

Carboniferous boundary in the Carnic Alps and the Rhenish Massif. *Palaeogeography, Palaeoclimatology, Palaeoecology*, 240(1-2):146–160.

[Karhu and Epstein, 1986] Karhu, J. and Epstein, S. (1986). The implication of the oxygen isotope records in coexisting cherts and phosphates. *Geochimica et Cosmochimica Acta*, 50(8):1745–1756.

[Kasting et al., 2006] Kasting, J. F., Howard, M. T., Wallmann, K., Veizer, J., Shields, G., and Jaffrés, J. (2006). Paleoclimates, ocean depth, and the oxygen isotopic composition of seawater. *Earth and Planetary Science Letters*, 252(1-2):82–93.

[Kaylor, 1988] Kaylor, D. (1988). Facies and diagenesis of the Upper Devonian Palliser Formation, Front Ranges of the southern Rocky Mountains, Alberta and BC Unpublished M. Sc. Master's thesis, thesis, McGill University, Montreal.

[Keith and Weber, 1964] Keith, M. and Weber, J. (1964). Carbon and oxygen isotopic composition of selected limestones and fossils. *Geochimica et Cosmochimica Acta*, 28(10-11):1787–1816.

[Ketzer et al., 2018] Ketzer, J. M., Augustin, A., Rodrigues, L. F., Oliveira, R., Praeg, D., Pivel, M. A. G., dos Reis, A. T., Silva, C., and Leonel, B. (2018). Gas seeps and gas hydrates in the Amazon deep-sea fan. *Geo-Marine Letters*, 38(5):429–438.

[Knauth and Lowe, 2003] Knauth, L. P. and Lowe, D. R. (2003). High Archean climatic temperature inferred from oxygen isotope geochemistry of cherts in the 3.5 Ga Swaziland Supergroup, South Africa. *Geological Society of America Bulletin*, 115(5):566–580.

[Kouchinsky et al., 2007] Kouchinsky, A., Bengtson, S., Pavlov, V., Runnegar, B., Torssander, P., Young, E., and Ziegler, K. (2007). Carbon isotope stratigraphy of the Precambrian–Cambrian Sukharikha River section, northwestern Siberian platform. *Geological Magazine*, 144(4):609–618.

[Kump and Garrels, 1986] Kump, L. and Garrels, R. M. (1986). Modeling atmospheric O2 in the global sedimentary redox cycle. *American Journal of Science*, 286(5):337–360.

[Kump and Arthur, 1999] Kump, L. R. and Arthur, M. A. (1999). Interpreting carbon-isotope excursions: carbonates and organic matter. *Chemical Geology*, 161(1-3):181–198.

[Kump et al., 2004] Kump, L. R., Kasting, J. F., Crane, R. G., et al. (2004). *The earth system*, volume 432.

[Lees, 1997] Lees, A. (1997). Biostratigraphy, sedimentology and palaeobathymetry of Waulsortian buildups and peri-Waulsortian rocks during the late Tournaisian regression, Dinant area, Belgium. *Geological Journal*, 32(1):1–36.

[Lemieux et al., 2011] Lemieux, Y., Hadlari, T., and Simonetti, A. (2011). Detrital zircon geochronology and provenance of Devono-Mississippian strata in the northern Canadian Cordilleran miogeocline. *Canadian Journal of Earth Sciences*, 48(2):515–541.

[Lenton et al., 2016] Lenton, T. M., Dahl, T. W., Daines, S. J., Mills, B. J., Ozaki, K., Saltzman, M. R., and Porada, P. (2016). Earliest land plants created modern levels of atmospheric oxygen. *Proceedings of the National Academy of Sciences*, 113(35):9704–9709.

[Leprieur et al., 2016] Leprieur, F., Descombes, P., Gaboriau, T., Cowman, P. F., Parravicini, V., Kulbicki, M., Melián, C. J., De Santana, C. N., Heine, C., Mouillot, D., et al. (2016). Plate tectonics drive tropical reef biodiversity dynamics. *Nature Communications*, 7(1):1–8.

[Lloyd, 1964] Lloyd, R. M. (1964). Variations in the oxygen and carbon isotope ratios of Florida Bay mollusks and their environmental significance. *The Journal of Geology*, 72(1):84–111.

[Mac Niocaill and Smethurst, 1994] Mac Niocaill, C. and Smethurst, M. A. (1994). Palaeozoic palaeogeography of Laurentia and its margins: a reassessment of palaeomagnetic data. *Geophysical Journal International*, 116(3):715–725.

[Macdonald et al., 2009] Macdonald, F. A., McClelland, W. C., Schrag, D. P., and Macdonald, W. P. (2009). Neoproterozoic glaciation on a carbonate platform margin in Arctic Alaska and the origin of the North Slope subterrane. *Geological Society of America Bulletin*, 121(3-4):448–473.

[Macqueen and Sandberg, 1970] Macqueen, R. W. and Sandberg, C. A. (1970). Stratigraphy, age, and interregional correlation of the Exshaw Formation, Alberta Rocky Mountains. *Bulletin of Canadian Petroleum Geology*, 18(1):32–66.

[Magaritz, 1983] Magaritz, M. (1983). Carbon and oxygen isotope composition of recent and ancient coated grains. In *Coated grains*, pages 27–37. Springer.

[Maloof et al., 2005] Maloof, A. C., Schrag, D. P., Crowley, J. L., and Bowring, S. A. (2005). An expanded record of Early Cambrian carbon cycling from the Anti-Atlas Margin, Morocco. *Canadian Journal of Earth Sciences*, 42(12):2195–2216.

[Marynowski et al., 2012] Marynowski, L., Zatoń, M., Rakociński, M., Filipiak, P., Kurkiewicz, S., and Pearce, T. J. (2012). Deciphering the upper Famennian Hangenberg Black Shale depositional environments based on multi-proxy record. *Palaeogeography, Palaeoclimatology, Palaeoecology*, 346:66–86.

[Mazzini et al., 2004] Mazzini, A., Ivanov, M., Parnell, J., Stadnitskaia, A., Cronin, B., Poludetkina, E., Mazurenko, L., and van Weering, T. (2004). Methane-related authigenic carbonates from the Black Sea: geochemical characterisation and relation to seeping fluids. *Marine Geology*, 212(1-4):153–181.

[McCay et al., 2006] McCay, G., Prave, A., Alsop, G. I., and Fallick, A. (2006). Glacial trinity: Neoproterozoic earth history within the British-Irish Caledonides. *Geology*, 34(11):909–912.

[McClay and Insley, 1986] McClay, K. and Insley, M. (1986). Duplex structures in the lewis thrust sheet, crowsnest pass, rocky mountains, Alberta, Canada. *Journal of Structural Geology*, 8(8):911–922.

[McFadden et al., 2008] McFadden, K. A., Huang, J., Chu, X., Jiang, G., Kaufman, A. J., Zhou, C., Yuan, X., and Xiao, S. (2008). Pulsed oxidation and biological evolution in the Ediacaran Doushantuo Formation. *Proceedings of the National Academy of Sciences*, 105(9):3197–3202.

[McKirdy et al., 2001] McKirdy, D. M., Burgess, J. M., Lemon, N. M., Yu, X., Cooper, A. M., Gostin, V. A., Jenkins, R. J., and Both, R. A. (2001). A chemostratigraphic overview of the late Cryogenian interglacial sequence in the Adelaide Fold-Thrust Belt, South Australia. *Precambrian Research*, 106(1-2):149–186.

[McLaren and Mountjoy, 1962] McLaren, D. J. and Mountjoy, E. W. (1962). *Alexo equivalents in the Jasper region, Alberta*. Department of Mines and Technical Surveys.

[Meijer-Drees et al., 1993] Meijer-Drees, N., Richards, B. C., and Johnston, D. (1993). *The Devonian Palliser Formation and its equivalents, southern Alberta, Canada*. Geological Survey of Canada.

[Miller et al., 2004] Miller, K. G., Sugarman, P. J., Browning, J. V., Kominz, M. A., Olsson, R. K., Feigenson, M. D., and Hernández, J. C. (2004). Upper Cretaceous sequences and sea-level history, New Jersey coastal plain. *GSA Bulletin*, 116(3-4):368–393.

[Mitnick et al., 2018] Mitnick, E. H., Lammers, L. N., Zhang, S., Zaretskiy, Y., and DePaolo, D. J. (2018). Authigenic carbonate formation rates in marine sediments and implications for the marine $\delta^{13}C$ record. *Earth and Planetary Science Letters*, 495:135–145.

[Morrow et al., 2005] Morrow, J. R., Sandberg, C. A., and Harris, A. G. (2005). Late devonian alamo impact, southern nevada, usa: Evidence of size, marine site, and widespread effects. *Large meteorite impacts III: Geological Society of America Special Paper*, 384:259–280.

[Mountjoy and Halim-Dihardja, 1991] Mountjoy, E. W. and Halim-Dihardja, M. K. (1991). Multiple phase fracture and fault-controlled burial dolomitization, Upper Devonian Wabamun Group, Alberta. *Journal of Sedimentary Research*, 61(4):590–612.

[Müller et al., 1997] Müller, R. D., Roest, W. R., Royer, J.-Y., Gahagan, L. M., and Sclater, J. G. (1997). Digital isochrons of the world's ocean floor. *Journal of Geophysical Research: Solid Earth*, 102(B2):3211–3214.

[Murphy et al., 2000] Murphy, A. E., Sageman, B. B., Hollander, D. J., Lyons, T. W., and Brett, C. E. (2000). Black shale deposition and faunal overturn in the devonian appalachian basin: Clastic starvation, seasonal water-column mixing, and efficient biolimiting nutrient recycling. *Paleoceanography*, 15(3):280–291.

[Myrow et al., 2011] Myrow, P. M., Strauss, J. V., Creveling, J. R., Sicard, K. R., Ripperdan, R., Sandberg, C. A., and Hartenfels, S. (2011). A carbon isotopic and

sedimentological record of the latest Devonian (Famennian) from the Western US and Germany. *Palaeogeography, Palaeoclimatology, Palaeoecology*, 306(3-4):147–159.

[O'Connell et al., 1990] O'Connell, S. C., Dix, G. R., and Barclay, J. E. (1990). The origin, history, and regional structural development of the Peace River Arch, Western Canada. *Bulletin of Canadian Petroleum Geology*, 38(1):4–24.

[Odin and Fullagar, 1988] Odin, G. and Fullagar, P. (1988). Chapter C4 geological significance of the glaucony facies. In *Developments in Sedimentology*, volume 45, pages 295–332. Elsevier.

[Oehlert and Swart, 2014] Oehlert, A. M. and Swart, P. K. (2014). Interpreting carbonate and organic carbon isotope covariance in the sedimentary record. *Nature Communications*, 5(1):1–7.

[Pană and van der Pluijm, 2015] Pană, D. I. and van der Pluijm, B. A. (2015). Orogenic pulses in the Alberta Rocky Mountains: Radiometric dating of major faults and comparison with the regional tectono-stratigraphic record. *Bulletin*, 127(3-4):480–502.

[Patterson and Walter, 1994] Patterson, W. P. and Walter, L. M. (1994). Depletion of ^{13}C in seawater ΣC02 on modern carbonate platforms: Significance for the carbon isotopic record of carbonates. *Geology*, 22(10):885–888.

[Paul et al., 2007] Paul, D., Skrzypek, G., and Fórizs, I. (2007). Normalization of measured stable isotopic compositions to isotope reference scales–a review. *Rapid Communications in Mass Spectrometry: An International Journal Devoted to the Rapid Dissemination of Up-to-the-Minute Research in Mass Spectrometry*, 21(18):3006–3014.

[Pawlik et al., 2020] Pawlik, Ł., Buma, B., Šamonil, P., Kvaček, J., Gałazka, A., Kohout, P., and Malik, I. (2020). Impact of trees and forests on the devonian landscape and weathering processes with implications to the global earth's system properties-a critical review. *Earth-Science Reviews*, page 103200.

[Perkins et al., 2008] Perkins, R., Piper, D., and Mason, C. (2008). Trace-element budgets in the ohio/sunbury shales of kentucky: constraints on ocean circulation

and primary productivity in the devonian–mississippian appalachian basin. *Palaeogeography, Palaeoclimatology, Palaeoecology*, 265(1-2):14–29.

[Peterhänsel et al., 2008] Peterhänsel, A., Pratt, B. R., and Holmden, C. (2008). The Famennian (Upper Devonian) Palliser platform of Western Canada–architecture and depositional dynamics of a post-extinction epeiric giant. *Dynamics of Epeiric Seas: Geological Society of Canada Special Paper*, 48:247–281.

[Peters et al., 2018] Peters, S. E., Husson, J. M., and Czaplewski, J. (2018). Macrostrat: a platform for geological data integration and deep-time Earth crust research. *Geochemistry, Geophysics, Geosystems*, 19(4):1393–1409.

[Planavsky et al., 2014] Planavsky, N. J., Reinhard, C. T., Wang, X., Thomson, D., McGoldrick, P., Rainbird, R. H., Johnson, T., Fischer, W. W., and Lyons, T. W. (2014). Low Mid-Proterozoic atmospheric oxygen levels and the delayed rise of animals. *Science*, 346(6209):635–638.

[Pokrovsky and Bujakaite, 2015] Pokrovsky, B. and Bujakaite, M. (2015). Geochemistry of C, O, and Sr isotopes in the Neoproterozoic carbonates from the southwestern Patom paleobasin, southern Middle Siberia. *Lithology and Mineral Resources*, 50(2):144–169.

[Potter et al., 1993] Potter, J., Richards, B. C., and Goodarzi, F. (1993). The organic petrology and thermal maturity of lower Carboniferous and Upper Devonian source rocks in the Liard basin, at Jackfish Gap-Yohin Ridge and North Beaver River, northern Canada: implications for hydrocarbon exploration. *Energy sources*, 15(2):289–314.

[Potter et al., 2012] Potter, P. E., Maynard, J. B., and Pryor, W. A. (2012). *Sedimentology of shale: study guide and reference source*. Springer Science & Business Media.

[Prave, 1999] Prave, A. (1999). The Neoproterozoic Dalradian Supergroup of Scotland: an alternative hypothesis. *Geological Magazine*, 136(6):609–617.

[Prave et al., 2009] Prave, A., Fallick, A., Thomas, C., and Graham, C. (2009). A composite C-isotope profile for the Neoproterozoic Dalradian Supergroup of Scotland and Ireland. *Journal of the Geological Society*, 166(5):845–857.

[Pysklywec and Mitrovica, 2000] Pysklywec, R. and Mitrovica, J. (2000). Mantle flow mechanisms of epeirogeny and their possible role in the evolution of the Western Canada Sedimentary Basin. *Canadian Journal of Earth Sciences*, 37(11):1535–1548.

[Rakociński et al., 2020] Rakociński, M., Marynowski, L., Pisarzowska, A., Bełdowski, J., Siedlewicz, G., Zatoń, M., Perri, M. C., Spalletta, C., and Schönlaub, H. P. (2020). Volcanic related methylmercury poisoning as the possible driver of the end-devonian mass extinction. *Scientific Reports*, 10(1):1–8.

[Ricci et al., 2013] Ricci, J., Quidelleur, X., Pavlov, V., Orlov, S., Shatsillo, A., and Courtillot, V. (2013). New $^{40}Ar/^{39}Ar$ and K–Ar ages of the Viluy traps (Eastern Siberia): further evidence for a relationship with the Frasnian–Famennian mass extinction. *Palaeogeography, Palaeoclimatology, Palaeoecology*, 386:531–540.

[Richards et al., 1993] Richards, B., Bamber, E., Henderson, C., Higgins, A., Johnston, D., Mamet, B., and Meijer-Drees, N. (1993). Uppermost Devonian (Famennian) and Lower Carboniferous (Tournaisian) at Jura Creek, and Mount Rundle, southwestern Alberta: Geological Survey of Canada. *Open File*, 2866:81.

[Richards et al., 1994] Richards, B., Barclay, J., Bryan, D., H. A., Henderson, C., and Hinds, R. (1994). Carboniferous strata of the Western Canada Sedimentary Basin. *Geological Atlas of the Western Canada Sedimentary Basin. Canadian Society of Petroleum Geologists*, pages 221–250.

[Richards et al., 1990] Richards, B., Barclay, J., Osadetz, K., Trollope, F., and Hartling, A. (1990). Carboniferous strata of the Western Canada Sedimentary Basin. *Bulletin of Canadian Petroleum Geology*, 38(1):178–178.

[Richards and Higgins, 1988] Richards, B. and Higgins, A. (1988). Devonian-Carboniferous boundary beds of the Palliser and Exshaw formations at Jura Creek, Rocky Mountains, southwestern Alberta. *CSPG Special Publications*, pages 399–412.

[Richards et al., 2002] Richards, B. C., Ross, G. M., Utting, J., and Hills, L. (2002). U–Pb geochronology, lithology and biostratigraphy of tuff in the upper Famennian to Tournaisian Exshaw Formation: evidence for a mid-Paleozoic magmatic arc on the northwestern margin of North America. *Canadian Society of Petroleum Geologists Memoir*, 19:158–207.

[Riegel, 2008] Riegel, W. (2008). The Late Palaeozoic phytoplankton blackout—Artefact or evidence of global change? *Review of Palaeobotany and Palynology*, 148(2-4):73–90.

[Ripperdan, 2001] Ripperdan, R. L. (2001). Stratigraphic variation in marine carbonate carbon isotope ratios. *Reviews in Mineralogy and Geochemistry*, 43(1):637–662.

[Riquier et al., 2006] Riquier, L., Tribovillard, N., Averbuch, O., Devleeschouwer, X., and Riboulleau, A. (2006). The Late Frasnian Kellwasser horizons of the Harz Mountains (Germany): two oxygen-deficient periods resulting from different mechanisms. *Chemical Geology*, 233(1-2):137–155.

[Root, 2001] Root, K. G. (2001). Devonian Antler fold and thrust belt and foreland basin development in the southern Canadian Cordillera: implications for the Western Canada Sedimentary Basin. *Bulletin of Canadian Petroleum Geology*, 49(1):7–36.

[Rose et al., 2012] Rose, C. V., Swanson-Hysell, N. L., Husson, J. M., Poppick, L. N., Cottle, J. M., Schoene, B., and Maloof, A. C. (2012). Constraints on the origin and relative timing of the Trezona $\delta^{13}C$ anomaly below the end-Cryogenian glaciation. *Earth and Planetary Science Letters*, 319:241–250.

[Saitoh et al., 2015] Saitoh, M., Ueno, Y., Isozaki, Y., Shibuya, T., Yao, J., Ji, Z., Shozugawa, K., Matsuo, M., and Yoshida, N. (2015). Authigenic carbonate precipitation at the end-Guadalupian (Middle Permian) in China: implications for the carbon cycle in ancient anoxic oceans. *Progress in Earth and Planetary Science*, 2(1):41.

[Sandberg et al., 2002] Sandberg, C. A., Morrow, J. R., and Ziegler, W. (2002). Late Devonian sea-level changes, catastrophic events, and mass extinctions. *Special Papers-Geological Society of America*, pages 473–488.

[Savoy et al., 1999] Savoy, L. E., Harris, A. G., and Mountjoy, E. W. (1999). Extension of lithofacies and conodont biofacies models of Late Devonian to Early Carboniferous carbonate ramp and black shale systems, southern Canadian Rocky Mountains. *Canadian Journal of Earth Sciences*, 36(8):1281–1298.

[Savoy and Mountjoy, 1995] Savoy, L. E. and Mountjoy, E. W. (1995). Cratonic-margin and Antler-age foreland basin strata (Middle Devonian to Lower Carbonif-

erous) of the southern Canadian Rocky Mountains and adjacent plains. volume 52. Special Publications of SEPM.

[Sawaki et al., 2008] Sawaki, Y., Ohno, T., Fukushi, Y., Komiya, T., Ishikawa, T., Hirata, T., and Maruyama, S. (2008). Sr isotope excursion across the Precambrian–Cambrian boundary in the Three Gorges area, South China. *Gondwana Research*, 14(1-2):134–147.

[Schieber and Baird, 2001] Schieber, J. and Baird, G. (2001). On the origin and significance of pyrite spheres in Devonian black shales of North America. *Journal of Sedimentary Research*, 71(1):155–166.

[Schlager, 2005] Schlager, W. (2005). *Carbonate sedimentology and sequence stratigraphy*. Number 8. SEPM Soc for Sed Geology.

[Schrag et al., 2013] Schrag, D. P., Higgins, J. A., Macdonald, F. A., and Johnston, D. T. (2013). Authigenic carbonate and the history of the global carbon cycle. *science*, 339(6119):540–543.

[Selby and Creaser, 2005] Selby, D. and Creaser, R. A. (2005). Direct radiometric dating of the Devonian-Mississippian time-scale boundary using the Re-Os black shale geochronometer. *Geology*, 33(7):545–548.

[Shackleton, 1967] Shackleton, N. (1967). Oxygen isotope analyses and Pleistocene temperatures re-assessed. *Nature*, 215(5096):15–17.

[Sibley and Gregg, 1987] Sibley, D. F. and Gregg, J. M. (1987). Classification of dolomite rock textures. *Journal of Sedimentary Research*, 57(6):967–975.

[Sleep and Zahnle, 2001] Sleep, N. H. and Zahnle, K. (2001). Carbon dioxide cycling and implications for climate on ancient Earth. *Journal of Geophysical Research: Planets*, 106(E1):1373–1399.

[Smith and Bustin, 2000] Smith, M. G. and Bustin, R. M. (2000). Late Devonian and Early Mississippian Bakken and Exshaw black shale source rocks, Western Canada Sedimentary Basin: a sequence stratigraphic interpretation. *AAPG bulletin*, 84(7):940–960.

[Smith et al., 1993] Smith, M. T., Dickinson, W. R., and Gehrels, G. E. (1993). Contractional nature of Devonian-Mississippian Antler tectonism along the North American continental margin. *Geology*, 21(1):21–24.

[Sorauf, 1989] Sorauf, J. (1989). Rugosa and the Frasnian-Famennian extinction event: a progress report. *Association of Australasian Palaeontology*, 8:327–338.

[Speed and Sleep, 1982] Speed, R. and Sleep, N. (1982). Antler orogeny and foreland basin: A model. *Geological Society of America Bulletin*, 93(9):815–828.

[Stanley, 2016] Stanley, S. M. (2016). Estimates of the magnitudes of major marine mass extinctions in Earth history. *Proceedings of the National Academy of Sciences*, 113(42):E6325–E6334.

[Stanley and Hardie, 1998] Stanley, S. M. and Hardie, L. A. (1998). Secular oscillations in the carbonate mineralogy of reef-building and sediment-producing organisms driven by tectonically forced shifts in seawater chemistry. *Palaeogeography, Palaeoclimatology, Palaeoecology*, 144(1-2):3–19.

[Stanley and Hardie, 1999] Stanley, S. M. and Hardie, L. A. (1999). Hypercalcification: paleontology links plate tectonics and geochemistry to sedimentology. *GSA today*, 9(2):1–7.

[Stearn, 1988] Stearn, C. W. (1988). Stromatoporoids from the Famennian (Devonian) Wabamun Formation, Normandville oilfield, north–central Alberta, Canada. *Journal of Paleontology*, 62(3):411–419.

[Stevenson et al., 2000] Stevenson, R. K., Whittaker, S., and Mountjoy, E. W. (2000). Geochemical and Nd isotopic evidence for sedimentary-source changes in the Devonian miogeocline of the southern Canadian Cordillera. *GSA Bulletin*, 112(4):531–539.

[Stoakes, 1992] Stoakes, F. (1992). Wabamun megasequence. In *Devonian-Early Mississippian Carbonates of the Western Canada Sedimentary Basin: A Sequence Stratigraphic Framework*, volume 28. Special Publications of SEPM.

[Streel et al., 2000] Streel, M., Caputo, M. V., Loboziak, S., and Melo, J. H. G. (2000). Late Frasnian-Famennian climates based on palynomorph analyses and the question of the Late Devonian glaciations. *Earth-Science Reviews*, 52(1-3):121–173.

[Sun and Turchyn, 2014] Sun, X. and Turchyn, A. V. (2014). Significant contribution of authigenic carbonate to marine carbon burial. *Nature Geoscience*, 7(3):201.

[Tartèse et al., 2016] Tartèse, R., Chaussidon, M., Gurenko, A., Delarue, F., and Robert, F. (2016). Warm archaean oceans reconstructed from oxygen isotope composition of early-life remnants. *Geochemical Perspectives Letters*, 3:55–65.

[USGS, 2008] USGS (2008). Geochemistry of rock samples from the national geochemical database. *US Geological Survey*, 97.

[van Loevezijn and Raven, 2017] van Loevezijn, G. B. and Raven, J. (2017). From carbonate platform to euxinic sea–the collapse of an Early/Middle Devonian reef, Cantabrian Mountains (Spain). *Geologos*, 23(3):143–161.

[Veevers and Powell, 1987] Veevers, J. t. and Powell, C. M. (1987). Late Paleozoic glacial episodes in Gondwanaland reflected in transgressive-regressive depositional sequences in Euramerica. *Geological Society of America Bulletin*, 98(4):475–487.

[Veizer et al., 1999] Veizer, J., Ala, D., Azmy, K., Bruckschen, P., Buhl, D., Bruhn, F., Carden, G. A., Diener, A., Ebneth, S., Godderis, Y., et al. (1999). $^{87}Sr/^{86}Sr$, $\delta^{13}C$ and $\delta^{18}O$ evolution of Phanerozoic seawater. *Chemical geology*, 161(1-3):59–88.

[Veizer et al., 1997] Veizer, J., Bruckschen, P., Pawellek, F., Diener, A., Podlaha, O. G., Carden, G. A., Jasper, T., Korte, C., Strauss, H., Azmy, K., et al. (1997). Oxygen isotope evolution of phanerozoic seawater. *Palaeogeography, Palaeoclimatology, Palaeoecology*, 132(1-4):159–172.

[Veizer and Hoefs, 1976] Veizer, J. and Hoefs, J. (1976). The nature of O^{18}/O^{16} and C^{13}/C^{12} secular trends in sedimentary carbonate rocks. *Geochimica et Cosmochimica Acta*, 40(11):1387–1395.

[Verdel et al., 2011] Verdel, C., Wernicke, B. P., and Bowring, S. A. (2011). The Shuram and subsequent Ediacaran carbon isotope excursions from southwest Laurentia, and implications for environmental stability during the metazoan radiation. *Bulletin*, 123(7-8):1539–1559.

[Wallmann, 2001] Wallmann, K. (2001). The geological water cycle and the evolution of marine $\delta^{18}O$ values. *Geochimica et Cosmochimica Acta*, 65(15):2469–2485.

[Webb, 1994] Webb, G. (1994). The Frasnian-Famennian extinction event: dominance of extrinsic over intrinsic factors in the recovery of reef communities. In *New Developments Regarding the KT Event and Other Catastrophes in Earth History*, volume 825, page 132.

[Webb, 2002] Webb, G. E. (2002). Latest Devonian and Early Carboniferous reefs: depressed reef building after the Middle Paleozoic collapse.

[Wigley and Compton, 2006] Wigley, R. A. and Compton, J. S. (2006). Late Cenozoic evolution of the outer continental shelf at the head of the Cape Canyon, South Africa. *Marine Geology*, 226(1-2):1–23.

[Wilkin and Barnes, 1996] Wilkin, R. and Barnes, H. (1996). Pyrite formation by reactions of iron monosulfides with dissolved inorganic and organic sulfur species. *Geochimica et Cosmochimica Acta*, 60(21):4167–4179.

[Wonfor and Andrichuk, 1956] Wonfor, J. and Andrichuk, J. (1956). The Wabamun group in the Stettler area, Alberta. *Bulletin of Canadian Petroleum Geology*, 4(5):99–111.

[Wood, 1993] Wood, R. (1993). Nutrients, predation and the history of reef-building. *Palaios*, pages 526–543.

[Workman et al., 2002] Workman, R., Grotzinger, J., and Hart, S. (2002). Constraints on Neoproterozoic ocean chemistry from $\delta^{13}C$ and $\delta^{11}B$ analyses of carbonates from the Witvlei and Nama Groups, Namibia. *Geochimica et Cosmochimica Acta*, 66(15A).

[Workum and Hedinger, 1992] Workum, R. H. and Hedinger, A. S. (1992). *Devonian Frasnian stratigraphy, Rocky Mountain Front Ranges Crowsnest Pass to Jasper, Alberta*. Geological Survey of Canada.

[Wright et al., 2013] Wright, N., Zahirovic, S., Müller, R., and Seton, M. (2013). Towards community-driven paleogeographic reconstructions: integrating open-access paleogeographic and paleobiology data with plate tectonics. *Biogeosciences*, 10(3).

[Zachos et al., 2001] Zachos, J., Pagani, M., Sloan, L., Thomas, E., and Billups, K. (2001). Trends, rhythms, and aberrations in global climate 65 Ma to present. *science*, 292(5517):686–693.

[Zambito et al., 2012] Zambito, J. J., Brett, C. E., and Baird, G. C. (2012). The Late Middle Devonian (Givetian) Global Taghanic Biocrisis in its type area (northern Appalachian Basin): geologically rapid faunal transitions driven by global and local environmental changes. In *Earth and Life*, pages 677–703. Springer.

[Zeebe and Wolf-Gladrow, 2001] Zeebe, R. E. and Wolf-Gladrow, D. (2001). *CO2 in seawater: equilibrium, kinetics, isotopes*. Gulf Professional Publishing.

[Zervas et al., 2009] Zervas, D., Nichols, G. J., Hall, R., Smyth, H. R., Lüthje, C., and Murtagh, F. (2009). SedLog: A shareware program for drawing graphic logs and log data manipulation. *Computers & Geosciences*, 35(10):2151–2159.

[Zhao et al., 2016] Zhao, M.-Y., Zheng, Y.-F., and Zhao, Y.-Y. (2016). Seeking a geochemical identifier for authigenic carbonate. *Nature Communications*, 7(1):1–7.

Appendix A

Additional Information

Sample depth (mbs)	**Lithofacies**	**Lithology**	$\delta^{13}C$	$\delta^{18}O$	**$CaCO_3$ (wt%)**
3985	B2	Black Shale	-1.64	-11.36	2.73*
3986	B2	Black Shale	-	-	0.185*
3987	B2	Black Shale	4.6	-10.24	0.281
3988	B2	Black Shale	-	-	0.808*
3989	B2	Black Shale	-	-	0.368*
3990	B2	Black Shale	-	-	0.455*
3991	B2	Black Shale	2.09	-9.39	11.65*
3992	B2	Black Shale	-	-	0.307*
3993	B2	Black Shale	-	-	0.06
3994	B2	Black Shale	-	-	0.09*
3995	B2	Black Shale	-	-	7.08
3996	B2	Black Shale	-	-	0.503*
3997	B1	Calcareous Black Shale	-0.44	-10.44	3.17*
3998	B1	Calcareous Black Shale	-	-	3.23
3999	B1	Calcareous Black Shale	-1.24	-10.25	2.13*
3999.38	B3	Carbonate Concretion	3.25	-10.09	7.78*
4000	B1	Calcareous Black Shale	-2.55	-9.9	8.25
4001	B1	Calcareous Black Shale	-0.44	-10.95	2.13*
4001.75	B1	Calcareous Black Shale	-0.34	-8.97	4.6*
4003	B1	Calcareous Siltstone	-0.06	-10.4	2.23*

4004	B1	Calcareous Siltstone	-1.42	-11.06	15.28
4004.5	B2	Siltstone	0.1	-10.04	2.43*
4005	B2	Siltstone	0.26	-7.47	8.50
4005.5	B2	Siltstone	-1.27	-10.65	7.17*
4006	B2	Siltstone	0.49	-8.64	4.2*
4007	B1	Calcareous Siltstone			0.97*
4008	B2	Siltstone	1.07	-10.18	19.67*
4009	B2	Siltstone	-0.09	-10.95	4.84
4010	B1	Calcareous Siltstone	0.06	-9.78	2.25*
4011	B2	Siltstone	0.80	-8.91	1.53*
4012	B2	Siltstone	0.50	-11	5.15*
4013	B2	Siltstone	-	-	0.17
4014	B1	Calcareous Siltstone	1.19	-10.37	5.97*
4015	B1	Calcareous Siltstone	-	-	1.23*
4016	B2	Siltstone	-2.26	-11.17	4.17*
4017	B1	Calcareous Siltstone	-0.80	-8.32	0.24
4018	B2	Siltstone	-	-	0.13*
4019	B1	Calcareous Siltstone	-	-	1.27*
4020	B1	Calcareous Siltstone	1.41	-9.92	7.47*
4021	B1	Calcareous Siltstone	-1.41	-10.08	4.89*
4022	B1	Calcareous Siltstone	-1.39	-12.98	3.63*

Table A.1: Stable isotope and bulk calcium carbonate data from Besa River section core samples. (-) indicate a lack of data, (*) inferred measurements.

Sample height (m)	**Lithofacies**	**Lithology**	$\delta^{13}C$	$\delta^{18}O$
0	OP1	Lime Mudstone	2.23	-5.01
1	OP1	Lime Mudstone	2.04	-5.40
2	OP1	Lime Mudstone	2	-5.44
3	OP1	Lime Mudstone	2.16	-4.95
4	OP1	Lime Mudstone	2.06	-5.50
5	OP1	Lime Mudstone	1.76	-5.23
6	OP2	Lime Mudstone	2.19	-5.55
7	OP2	Lime Mudstone	2.11	-5.60
8	OP2	Lime Mudstone	1.95	-5.49
9	OP2	Lime Mudstone	2.14	-4.93
10.1	OP2	Lime Mudstone	1.92	-5.49
10.9	OP2	Lime Mudstone	2.00	-5.61
12	OP2	Lime Mudstone	2.14	-5.24
13	OP2	Lime Mudstone	2.21	-5.95
14	OP2	Lime Mudstone	2.21	-5.27
15	OP2	Lime Mudstone	2.22	-5.44
16	OP2	Lime Mudstone	2.34	-5.40
17	OP2	Lime Mudstone	2.19	-5.52
18.1	OP2	Lime Mudstone	2.00	-5.66
19.1	OP2	Lime Mudstone	1.94	-8.62
20	OP2	Lime Mudstone	1.97	-5.66
21	OP2	Lime Mudstone	1.78	-6.38
22	OP2	Lime Mudstone	2.00	-5.27
23	OP2	Lime Mudstone	2.25	-5.77
24	OP2	Lime Mudstone	2.10	-5.29
25	OP2	Lime Mudstone	2.02	-5.60
26	OP2	Lime Mudstone	2.07	-5.46
27	OP2	Lime Mudstone	1.88	-5.59
28	OP2	Lime Mudstone	1.67	-4.91
29	OP2	Lime Mudstone	1.88	-5.59
30	OP2	Lime Mudstone	1.84	-5.89
31	OP2	Lime Mudstone	1.86	-5.75

32	OP2	Lime Mudstone	1.84	-6.23
33	OP2	Lime Mudstone	2.05	-5.74
34	OP3	Lime Mudstone	1.96	-5.86
35	OP3	Lime Mudstone	1.87	-5.73
36.5	OP3	Lime Mudstone	1.93	-6.31
37	OP3	Lime Mudstone	1.96	-5.86
38	OP3	Lime Mudstone	2.11	-5.60
39	OP3	Lime Mudstone	1.70	-5.65
40	OP3	Lime Mudstone	1.87	-5.83
41	OP3	Lime Mudstone	1.55	-5.68
42	OP3	Lime Mudstone	1.76	-7.91
43	OP3	Lime Mudstone	1.74	-6.00
48.4	OP3	Lime Mudstone	1.58	-6.35
49	OP3	Lime Mudstone	2.11	-6.24
50	OP3	Lime Mudstone	1.72	-5.72
51	OP3	Lime Mudstone	1.74	-6.03
52	OP3	Lime Mudstone	2.01	-6.28
53	OP3	Lime Mudstone	2.00	-5.70
55	OP3	Lime Mudstone	2.00	5.38
56	OP3	Lime Mudstone	1.69	-5.57
56.8	OP3	Lime Mudstone	2.00	-5.46
58.2	OP2	Lime Mudstone	1.44	-5.80
59	OP2	Lime Mudstone	1.64	-5.70
60.2	OP2	Lime Mudstone	1.75	-4.84
61	OP2	Lime Mudstone	2.04	-5.62
62	OP2	Lime Mudstone	2.16	-5.46
63	OP2	Lime Mudstone	2.05	-5.68
64	OP2	Lime Mudstone	1.59	-5.75
64.9	OP2	Lime Mudstone	1.86	-6.00
65.2	OP2	Lime Mudstone	1.21	-5.95
71.7	O1	Wackestone	1.39	-6.19
73	OP1	Wackestone	1.66	-5.82
74	OP1	Wackestone	1.53	-5.69

74.9	OP1	Wackestone	0.96	-5.70
76.5	OP1	Wackestone	1.39	-6.03
78.6	OP1	Wackestone	1.77	-6.19
79.6	OP1	Wackestone	0.92	-6.36
81	OP1	Wackestone	1.28	-6.64
81.3	OP1	Wackestone	1.30	-6.31
106.5	OP4	Mudstone - Siltstone	1.47	-8.24
107.5	OP4	Mudstone - Siltstone	2.19	-8.10
109	OP4	Mudstone - Siltstone	1.55	-7.55
110	OP4	Mudstone - Siltstone	1.59	-7.83
111	OP4	Mudstone - Siltstone	1.52	-8.50
112	OP4	Mudstone - Siltstone	2.03	-8.22
113	OP4	Mudstone - Siltstone	1.83	-8.30
114	OP4	Mudstone - Siltstone	2.02	-8.09
115	OP4	Mudstone - Siltstone	1.18	-8.48
116.4	OP4	Mudstone - Siltstone	1.72	-8.73
117	OP4	Mudstone - Siltstone	1.81	-8.60
118	OP4	Mudstone - Siltstone	1.60	-8.76
119.5	OP4	Mudstone - Siltstone	1.70	-8.87
120.1	OP4	Sandstone	0.48	-10.93
121	OP4	Sandstone	0.88	-8.27
122	OP4	Sandstone	1.61	-9.40
123	OP4	Sandstone	1.06	-9.48
124	OP4	Sandstone	1.54	-9.68
125	OP4	Sandstone	1.13	-9.04
126.8	OP5	Siltstone	-	-
127.3	OP5	Lime Mudstone	1.37	-10.51
127.7	OP5	Siltstone	-	-
128	OP5	Calcareous Siltstone	1.50	-9.20
129	OP5	Calcareous Siltstone	0.89	-9.64
130	OP5	Calcareous Siltstone	-	-
131.1	OP5	Lime Mudstone	1.53	-9.90
132	OP5	Calcaerous Siltstone	0.64	-8.76

132.7	OP5	Lime Mudstone	0.44	-8.59
134.1	OP5	Lime Mudstone	1.71	-8.25
135.1	OP5	Lime Mudstone	1.73	-8.09
136.1	OP5	Lime Mudstone	1.63	-7.85
137.1	OP5	Lime Mudstone	1.72	-8.07
138	OP5	Lime Mudstone	1.61	-8.13
139	OP5	Lime Mudstone	1.70	-7.98
140	OP5	Lime Mudstone	1.56	-8.10
141	OP5	Lime Mudstone	0.45	-7.98
142	OP5	Calcareous Siltstone	0.61	-10.00
143.2	OP5	Calcareous Siltstone	0.92	-9.22
144.2	OP5	Lime Mudstone	0.9	-8.26
144.9	OP5	Lime Mudstone	0.15	-8.85
146	OP5	Lime Mudstone	0.97	-8.30
147	OP5	Lime Mudstone	1.40	-7.80
148	OP5	Lime Mudstone	1.40	-8.20
149	OP5	Lime Mudstone	1.28	-7.80
150	OP5	Lime Mudstone	1.53	-8.05
151	OP5	Lime Mudstone	1.55	-7.77
152	OP5	Calcareous Siltstone	1.35	-8.31
152.6	OP5	Siltstone	-	-
154.9	OP5	Calcareous Siltstone	1.34	-8.37
156	OP5	Lime Mudstone	1.51	-8.90
157	OP5	Lime Mudstone	1.48	-8.92
158	OP6	Calcareous Siltstone	1.76	-8.03
159	OP6	Calcareous Siltstone	1.29	-8.09
160	OP6	Calcareous Siltstone	1.35	-8.94
161	OP6	Calcareous Siltstone	1.45	-8.49
162	OP6	Calcareous Siltstone	1.47	-8.06
163	OP7	Calcareous Siltstone	1.40	-8.42
164	OP7	Calcareous Siltstone	1.13	-9.36
165	OP7	Calcareous Siltstone	1.36	-8.87
166	OP7	Calcareous Siltstone	1.25	-8.13

167	OP7	Calcareous Siltstone	1.87	-8.23
168	OP7	Calcareous Siltstone	1.16	-8.35
169	OP7	Calcareous Siltstone	1.51	-8.06
170	OP7	Calcareous Siltstone	1.65	-8.87
171.1	OP7	Calcareous Siltstone	1.28	-7.78
178.5	OP8	Calcareous Siltstone	1.19	-7.37
180	OP8	Calcareous Siltstone	1.59	-7.56
181	OP8	Calcareous Siltstone	1.62	-6.93
182	OP8	Calcareous Siltstone	1.72	-7.48
183	OP8	Calcareous Siltstone	1.59	-7.37
184	OP8	Calcareous Siltstone	1.57	-7.62
185	OP8	Calcareous Siltstone	1.46	-7.24
186	OP8	Calcareous Siltstone	1.53	-7.71
187	OP8	Calcareous Siltstone	1.52	-7.20
188	OP8	Calcareous Siltstone	1.44	-7.44
189	OP8	Calcareous Siltstone	1.66	-6.95
190	OP8	Calcareous Siltstone	1.60	-7.34
191	OP8	Calcareous Siltstone	1.46	-7.28
192	OP8	Calcareous Siltstone	1.45	-7.26
193	OP8	Calcareous Siltstone	-	-
194	OP8	Calcareous Siltstone	1.48	-7.33
195	OP8	Calcareous Siltstone	1.42	-10.60
196	OP8	Calcareous Siltstone	-	-
197	OP8	Calcareous Siltstone	1.43	-7.50
198	OP8	Calcareous Siltstone	1.48	-7.33
199	OP8	Calcareous Siltstone	1.57	-7.56
200	OP8	Calcareous Siltstone	1.44	-7.57
201	OP8	Calcareous Siltstone	1.61	-7.51
202	OP8	Calcareous Siltstone	1.54	-6.94
203	OP8	Calcareous Siltstone	1.59	-7.42
204	OP8	Calcareous Siltstone	1.51	-7.68
205	OP8	Calcareous Siltstone	1.73	-7.64
206	OP8	Calcareous Siltstone	1.17	-8.04

207	OP8	Calcareous Siltstone	1.23	-8.94
208	OP8	Calcareous Siltstone	1.10	-7.71
209	OP8	Calcareous Siltstone	1.26	-8.01
210	OP8	Calcareous Siltstone	1.57	-7.93
211	OP8	Calcareous Siltstone	1.49	-8.06
212	OP8	Calcareous Siltstone	1.47	-8.24
213	OP8	Calcareous Siltstone	1.53	-8.13
214	OP8	Calcareous Siltstone	1.52	-7.92
215	OP8	Calcareous Siltstone	1.39	-7.05
216	OP8	Calcareous Siltstone	1.55	-7.81
217	OP9	Lime Mudstone	1.49	-7.76
218	OP9	Lime Mudstone	1.57	-7.26
218.9	OP9	Lime Mudstone	1.56	-8.28
220.2	OP9	Lime Mudstone	-	-
220.8	OP9	Lime Mudstone	1.48	-7.47
222	OP9	Lime Mudstone	1.14	-7.67
223	OP9	Lime Mudstone	1.34	-8.29
224	OP9	Lime Mudstone	1.24	-8.11
225	OP9	Lime Mudstone	0.78	-8.00
226	OP9	Lime Mudstone	0.65	-8.44
226.8	OP9	Lime Mudstone	-	-
250.8	OP8	Calcareous Siltstone	-	-
251.3	OP8	Calcareous Siltstone	0.17	-9.37
252	OP8	Calcareous Siltstone	0.73	-8.68
253.1	OP8	Calcareous Siltstone	0.45	-8.43
254	OP8	Calcareous Siltstone	0.57	-8.02
255	OP8	Calcareous Siltstone	0.81	-8.59
256	OP8	Calcareous Siltstone	0.79	-7.81
257	OP8	Calcareous Siltstone	0.83	-8.54
259	OP8	Calcareous Siltstone	0.57	-7.46
260	OP8	Calcareous Siltstone	0.56	-9.39
261	OP8	Calcareous Siltstone	-	-
262	OP8	Calcareous Siltstone	0.59	-9.51

263.8	OP8	Calcareous Siltstone	0.46	-9.34
264.4	OP8	Calcareous Siltstone	0.61	-7.88
267.1	OP8	Calcareous Siltstone	0.62	-8.05
268.1	OP8	Calcareous Siltstone	0.53	-8.45
269.1	OP8	Calcareous Siltstone	0.81	-7.75
270.1	OP8	Calcareous Siltstone	0.52	-8.46
284.8	OP8	Calcareous Siltstone	0.76	-7.39
285.8	OP8	Calcareous Siltstone	0.39	-7.71
287	OP8	Calcareous Siltstone	0.3	-8.53
288	OP8	Calcareous Siltstone	0.4	-8.43
290	OP8	Calcareous Siltstone	0.77	-8.78
292	OP8	Calcareous Siltstone	0.76	-8.22
293	OP8	Calcareous Siltstone	1.06	-9.77
293.9	OP8	Calcareous Siltstone	1.34	-9.61
294.5	OP8	Calcareous Siltstone	0.56	-10.62
295.5	OP8	Calcareous Siltstone	1.01	-10.21
297	OP8	Calcareous Siltstone	1.07	-9.29
298	OP8	Calcareous Siltstone	0.94	-10.14
299	OP8	Calcareous Siltstone	0.92	-8.32
300	OP6	Calcareous Siltstone	0.72	-9.7
301	OP6	Calcareous Siltstone	1.1	-8.65
302	OP6	Calcareous Siltstone	0.83	-9.97
303	OP6	Calcareous Siltstone	0.85	-9.82
304.1	OP6	Calcareous Siltstone	1.1	-9.95
305	OP6	Calcareous Siltstone	1	-9.8
306	OP6	Calcareous Siltstone	0.58	-10.52
307	OP6	Calcareous Siltstone	0.89	-8.73
308	OP6	Calcareous Siltstone	0.62	-10.31
309	OP6	Calcareous Siltstone	0.47	-9.8
310	OP6	Calcareous Siltstone	0.72	-10.82
310.9	OP6	Calcareous Siltstone	0.55	-10.73
312	OP6	Calcareous Siltstone	0.44	-10.82
313	OP5	Calcareous Siltstone	0.79	-10.38

314	OP5	Calcareous Siltstone	0.65	-11.27
315	OP5	Calcareous Siltstone	0.62	-11.51
316	OP5	Calcareous Siltstone	0.56	-11.19
317	OP5	Calcareous Siltstone	0.73	-10.55
318	OP5	Calcareous Siltstone	0.81	-10.43
319	OP5	Calcareous Siltstone	0.75	-10.28
320	OP5	Calcareous Siltstone	0.63	-11.04
321	OP5	Calcareous Siltstone	0.79	-9.71
321.9	OP5	Calcareous Siltstone	0.39	-11.02
323	OP5	Calcareous Siltstone	0.57	-10.38
324	OP5	Calcareous Siltstone	0.64	-10.49
325	OP5	Calcareous Siltstone	0.74	-10.3
326	OP5	Lime Mudstone	0.45	-10.71
327	OP5	Lime Mudstone	0.5	-9.69
328	OP5	Calcareous Siltstone	0.48	-9.4
329	OP5	Calcareous Siltstone	0.6	-7.76
330.2	OP5	Calcareous Siltstone	0.66	-6.33
331.1	OP5	Lime Mudstone	0.76	-5.57
332	OP5	Lime Mudstone	0.74	-7.01
333	OP5	Lime Mudstone	0.55	-6.1
334	OP5	Lime Mudstone	0	-6.62
335	OP5	Lime Mudstone	-0.45	-6.85
336	OP6	Calcareous Siltstone	-0.29	-6.32
337	OP6	Calcareous Siltstone	0.16	-6.62
338	OP6	Calcareous Siltstone	-0.92	-7.14
339	OP1	Lime Mudstone	-0.11	-6.51
340	OP1	Lime Mudstone	0.18	-6.43
341	OP1	Lime Mudstone	-0.05	-6.46
342	OP1	Lime Mudstone	0.23	-6.1
343	OP1	Lime Mudstone	0.28	-6.2
344	OP1	Dolostone	0.73	-4.57
345	OP1	Dolostone	0.57	-5.75
346	OP1	Lime Mudstone	0.52	-5.94

347	OP1	Lime Mudstone	0.54	-6.29
348	OP1	Lime Mudstone	0.9	-6.00
349	OP1	Lime Mudstone	0.80	-5.69
350	OP1	Lime Mudstone	0.99	-6.29
351	OP1	Lime Mudstone	0.87	-6.54
352	OP1	Lime Mudstone	0.63	-6.34
353	OP1	Lime Mudstone	0.59	-6.48
354	OP1	Lime Mudstone	0.81	-6.06
355	OP1	Lime Mudstone	0.31	-6.50
356	OP1	Lime Mudstone	1.03	-5.36
357	OP1	Lime Mudstone	1.05	-5.92
358	OP1	Lime Mudstone	0.88	-6.27
359	OP3	Lime Mudstone	0.88	-6.49
360	OP3	Lime Mudstone	0.70	-5.62
361	OP3	Lime Mudstone	0.60	-6.51
362	OP3	Lime Mudstone	0.23	-6.60
363	OP3	Lime Mudstone	0.31	-6.35
364.1	OP3	Lime Mudstone	0.54	-6.10
365	OP3	Lime Mudstone	0.16	-6.35
366	OP3	Lime Mudstone	-5.60	-6.52
367	OP3	Lime Mudstone	-0.14	-6.38
368	OP3	Lime Mudstone	0.32	-6.15
369	OP3	Lime Mudstone	0.18	-6.45
370	OP3	Lime Mudstone	0.44	-6.03
371	OP3	Lime Mudstone	0.31	-6.02
372	OP3	Lime Mudstone	0.23	-6.20
373	OP11	Packstone	0.26	-6.15
374	OP11	Packstone	-0.67	-6.25
375	OP11	Packstone	-0.15	-6.36
376	OP11	Packstone	0.15	-6.37
377	OP11	Packstone	0.38	-6.38
378	OP11	Packstone	7.28	-6.61
379	OP11	Packstone	0.20	-6.20

380	OP11	Packstone	-0.32	-5.77
381	OP11	Packstone	-0.06	-6.14
381.9	OP1	Wackestone	-0.51	-6.01
383	OP1	Wackestone	-0.12	-6.17
384	OP1	Wackestone	-0.39	-6.16
385	OP1	Wackestone	-0.2	-5.9
386	OP1	Wackestone	0.4	-5.55
387	OP1	Wackestone	0.8	-6.14
388	OP10	Packstone	0.63	-6.3
389	OP10	Packstone	-0.02	-7.01
389.8	OP10	Packstone	-0.2	-6.03

Table A.2: Stable isotope data from Snaring section samples. (-) indicate a lack of data.

Sample height (m)	**Lithofacies**	**Lithology**	$\delta^{13}C$	$\delta^{18}O$
0	OP12	Dolostone	-1.18	-2.68
1	OP12	Dolostone	-3.32	-3.03
2	OP1	Lime Mudstone	-1.57	-5.14
3	OP18	Dolostone	-0.82	-2.17
4	OP18	Dolostone	-0.46	-2.27
5	OP18	Dolostone	-2.95	-4.46
6	OP18	Dolostone	-0.63	-3.15
7	OP1	Lime Mudstone	-1.5	-5.81
8	OP1	Lime Mudstone	-0.49	-3.37
9	OP1	Lime Mudstone	0	-5.37
10	OP1	Lime Mudstone	-0.62	-5.31
11	OP1	Lime Mudstone	-0.54	-6.2
12	OP1	Lime Mudstone	0.55	-5.11
13	OP1	Lime Mudstone	-0.09	-5.57
14	OP1	Wackestone	0.31	-3.95
15.1	OP1	Wackestone	0.03	-6.11
16	OP1	Wackestone	0.53	-6.87
17	OP1	Wackestone	0.34	-6.83
18	OP1	Wackestone	0.75	-6.3
19	OP1	Wackestone	-0.07	-7.11
20	OP1	Wackestone	0.25	-6.5
21	OP13	Wackestone	-0.03	-6.7
22	OP13	Wackestone	0.06	-5.98
23	OP13	Wackestone	-0.11	-6.03
24	OP13	Wackestone	-0.24	-6.36
25	OP13	Wackestone	-0.08	-6.2
26	OP13	Wackestone	0.21	-6.12
27	OP13	Wackestone	0.23	-7.03
28	OP13	Wackestone	0.13	-5.78
29	OP13	Wackestone	0.22	-5.31
30	OP13	Wackestone	0.21	-4.96
31	OP13	Wackestone	-0.17	-5.36

32	OP13	Wackestone	-0.36	-6.93
32.5	OP11	Packstone	-	-
33	OP11	Packstone	-0.15	-6.41
34.1	OP11	Packstone	-0.03	-5.93
35	OP11	Packstone	0.95	-5.78
36.1	OP11	Packstone	0.62	-7.47
37	OP15	Lime Mudstone	1.88	-6.54
38	OP15	Lime Mudstone	0.33	-6.81
39	OP15	Lime Mudstone	-0.63	-7.91
40	OP15	Lime Mudstone	-0.42	-5.85
40.1	OP15	Lime Mudstone	-	-

Table A.3: Stable isotope data from Nordegg section samples. (-) indicate a lack of data.

Sample height (m)	**Lithofacies**	**Lithology**	$\delta^{13}C$	$\delta^{18}O$
0	OP12	Dolostone	1.08	-5.21
1.1	OP12	Dolostone	1.17	-4.02
2	OP12	Dolostone	1.11	-4.66
3	OP12	Dolostone	0.96	-5.18
4	OP12	Dolostone	0.98	-4.84
5	OP12	Dolostone	0.52	-5.71
6	OP12	Dolostone	0.53	-4.74
7	OP12	Dolostone	0.28	-7.4
8	OP12	Dolostone	0.55	-5.06
9	OP12	Dolostone	0.43	-11.95
10	OP12	Dolostone	-0.16	-9.22
11	OP12	Dolostone	0.21	-6.57
12	OP12	Dolostone	-0.07	-7.76
13	OP12	Dolostone	0.21	-6.84
14	OP12	Dolostone	0.57	-4.66
15	OP12	Dolostone	0.4	-5.48
16	OP12	Dolostone	-0.12	-6.91
17	OP12	Dolostone	0.19	-6.23
18	OP12	Dolostone	-0.05	-8.05
19	OP12	Dolostone	-0.46	-8.24
20	OP13	Wackestone	-0.28	-8.11
21	OP13	Wackestone	0.01	-7.5
22	OP13	Wackestone	0.33	-5.96
23	OP13	Wackestone	0.21	-5.95
24	OP13	Wackestone	0.2	-6.5
25	OP13	Wackestone	-0.07	-7.47
26	OP13	Wackestone	0.13	-7.26
27	OP13	Wackestone	-	-
28	OP13	Wackestone	0.26	-7.13
29	OP13	Wackestone	0.06	-7.65
30	OP13	Wackestone	0.8	-6.37
31	OP13	Wackestone	0.58	-6.22

32.3	OP13	Wackestone	0.89	-6.11
33	OP13	Wackestone	0.43	-7.72
34	OP13	Wackestone	0.83	-5.63
35	OP13	Wackestone	0.56	-5.51
36	OP13	Wackestone	0.38	-5.83
37	OP13	Wackestone	0.19	-7.45
37.8	OP13	Wackestone	0	-7.9
38.5	OP13	Wackestone	-0.39	-8.23
39.5	OP13	Wackestone	-0.49	-7.72
40	OP13	Wackestone	-0.06	-7.43
41	OP13	Wackestone	0.21	-7.41
42	OP13	Wackestone	0.18	-8.47
43	OP13	Wackestone	0.49	-7.54
44	OP13	Wackestone	0.31	-8.3
45	OP13	Wackestone	0.69	-7.3
46	OP13	Wackestone	0.94	-6.31
47	OP13	Wackestone	1.45	-4.45
48	OP13	Wackestone	0.8	-8.47
49	OP13	Wackestone	1.17	-5.53
50	OP13	Wackestone	0.91	-6.85
51	OP13	Wackestone	1.14	-6.48
52	OP13	Wackestone	0.98	-6.2
52.8	OP13	Wackestone	0.64	-7.88
56	OP13	Wackestone	0.26	-7.9
57	OP13	Wackestone	0.52	-7.6
58	OP13	Wackestone	0.23	-7.58
59	OP13	Wackestone	0.53	-6.49
59.9	OP13	Wackestone	0.16	-7.93
60	OP1	Wackestone	0.59	-8.64
61	OP1	Wackestone	0.65	-8.01
62	OP1	Wackestone	0.47	-8.8
63	OP1	Wackestone	0.72	-7.86
64	OP1	Wackestone	0.4	-8.06

65	OP1	Wackestone	0.39	-7.31
66	OP1	Wackestone	0.46	-6.71
66.5	OP1	Wackestone	-	-
70.4	OP1	Wackestone	-0.26	-7.76
71	OP1	Wackestone	-0.32	-8.23
72	OP1	Wackestone	-0.17	-8.67
73	OP1	Wackestone	-0.03	-7.69
74	OP1	Wackestone	-0.13	-7.7
75	OP1	Wackestone	-0.18	-6.52
76	OP1	Wackestone	-0.77	-7.91
77	OP1	Wackestone	-0.5	-8.26
78	OP1	Wackestone	-0.48	-7.26
79	OP1	Wackestone	-0.74	-8.06
80	OP1	Wackestone	-0.77	-7.91
81	OP1	Wackestone	-0.2	-6.4
82	OP1	Wackestone	-0.51	-7.52
83	OP1	Wackestone	-0.17	-6.13
83.5	OP1	Wackestone	-0.7	-6.98
85.3	OP1	Lime Mudstone	-0.24	-7.24
89.1	OP11	Packstone	0.23	-6.61
90	OP11	Packstone	-0.03	-6.93
91	OP11	Packstone	-0.22	-7.22
92	OP11	Packstone	-0.07	-7.2
93	OP11	Packstone	-0.98	-10.42
94	OP11	Packstone	-0.6	-6.83
97	OP11	Packstone	0.1	-7.17
98	OP11	Packstone	0.52	-7.64
99	OP11	Packstone	0.24	-7.54
100	OP11	Packstone	0.4	-7.36
101	OP11	Packstone	0.36	-7.69
102	OP11	Packstone	-	-
103	OP11	Packstone	-0.07	-7.34
104	OP11	Packstone	-0.55	-8.43

105	OP11	Packstone	-0.68	-6.96
106	OP11	Packstone	-0.71	-8.2
107	OP11	Packstone	-0.3	-7.72
108	OP11	Packstone	-0.08	-7.31
109	OP11	Packstone	-0.08	-7.06
110	OP11	Packstone	-0.16	-7.37
111	OP1	Wackestone	-0.04	-6.51
112	OP1	Wackestone	-0.01	-7.54
113	OP1	Wackestone	0.51	-5.49
114	OP1	Wackestone	0.14	-7.38
115	OP1	Wackestone	0.38	-6.5
116	OP1	Wackestone	0.38	-6.67
117	OP1	Wackestone	0.27	-7.22
118	OP1	Wackestone	0.25	-8.78
119	OP1	Wackestone	0.22	-7.96
120	OP1	Wackestone	0.39	-7.54
121	OP1	Wackestone	0.22	-8.11
122	OP1	Wackestone	0.43	-7.82
123	OP13	Packestone	0.55	-7.23
124	OP13	Packestone	0.4	-7.51
125	OP13	Packestone	0.28	-8
126	OP13	Packestone	0.53	-7.1
127	OP13	Packestone	0.55	-8.02
128	OP13	Packestone	0.56	-7.66
129	OP13	Packestone	0.57	-7.9
130	OP13	Packestone	0.68	-7.48
131	OP13	Packestone	0.95	-6.94
132	OP13	Packestone	0.89	-8.09
133	OP13	Packestone	0.68	-9.99
134	OP13	Packestone	0.9	-8.04
135	OP14	Wackestone	0.84	-8.1
136	OP14	Wackestone	1.05	-7.45
137	OP14	Wackestone	1.04	-7.11

138	OP14	Wackestone	0.91	-7.03
139	OP14	Wackestone	1.16	-7.05
140	OP14	Wackestone	1.44	-5.16
141	OP14	Wackestone	1.32	-7.35
142	OP1	Lime Mudstone	1.24	-6.18
143	OP1	Lime Mudstone	1.38	-6.4
144	OP1	Lime Mudstone	1.16	-7.35
145	OP1	Lime Mudstone	1.15	-7.27
146	OP1	Lime Mudstone	0.97	-7.96
147	OP10	Packstone	0.93	-6.96
148	OP10	Packstone	1.09	-7.35
149	OP10	Packstone	0.63	-7.01
150	OP10	Packstone	1.13	-7.36
151	OP10	Packstone	1.12	-7.37
152	OP10	Packstone	1.13	-7.32
153	OP10	Packstone	0.88	-7.46
154	OP10	Packstone	0.88	-7.8
155	OP10	Packstone	1.07	-7.1
156	OP10	Packstone	0.96	-6.93
157	OP10	Packstone	0.85	-7.26
158	OP10	Packstone	1.02	-7.42
159	OP10	Packstone	1.07	-10.7
159.5	OP10	Packstone	0.68	-7.88
163.6	OP10	Packstone	0.7	-7.34
165	OP10	Packstone	0.34	-7.78
166	OP10	Packstone	0.35	-7.7
167	OP10	Packstone	0.3	-8.11
168	OP10	Packstone	0.28	-7.72
169	OP10	Packstone	0.37	-8.11
170	OP15	Lime Mudstone	0.39	-8.09
171	OP15	Lime Mudstone	0.21	-8.37
172	OP15	Lime Mudstone	0.26	-7.56
173	OP15	Lime Mudstone	0.04	-7.64

174	OP11	Packstone	-0.12	-7.53
175	OP11	Packstone	-0.44	-7.61
176	OP11	Packstone	-0.34	-7.99
177	OP11	Packstone	-0.24	-6.05
178	OP11	Packstone	-0.4	-7.37
179	OP11	Packstone	-0.62	-7.71
179.7	OP11	Packstone	-0.69	-6.96
181.1	OP11	Packstone	-0.57	-6.64
182	OP11	Packstone	-0.62	-6.7
183	OP11	Packstone	-0.55	-5.86
184	OP16	Dolostone	-0.31	-4.47
185	OP16	Dolostone	-0.45	-5.18
186	OP16	Dolostone	0.06	-4.45
187	OP16	Dolostone	-0.46	-7.52
188	OP16	Dolostone	-0.2	-5.16
189	OP16	Dolostone	-0.15	-4.83
190	OP16	Dolostone	-0.16	-5.13
191	OP16	Dolostone	-0.22	-6.67
192	OP16	Dolostone	-0.32	-6.12
193	OP16	Dolostone	-0.2	-6.1
193.5	OP16	Dolostone	-	-
194	OP3	Lime Mudstone	-0.45	-6.94
194.7	OP3	Lime Mudstone	-0.31	-7.59
195.3	OP3	Lime Mudstone	-	-
210.8	OP17	Packstone	-0.03	-7.24
212	OP17	Packstone	-0.23	-7.94
212.2	OP17	Lime Mudstone	-	-
213	OP17	Lime Mudstone	-0.09	-6.95
214	OP17	Packstone	-0.15	-7.71
215	OP17	Lime Mudstone	-0.08	-6.14
217	OP17	Packstone	-0.18	-7.44
218	OP17	Lime Mudstone	-0.38	-6.89
219	OP17	Lime Mudstone	-0.3	-7.58

220	OP17	Lime Mudstone	-0.11	-6.94
221	OP17	Lime Mudstone	-0.02	-6.82
222.2	OP17	Lime Mudstone	-0.18	-7.3
289	OP1	Lime Mudstone	-0.76	-7.14
289.7	OP1	Lime Mudstone	-0.5	-6.89
290.2	OP1	Lime Mudstone	-0.68	-7.21
290.6	OP1	Lime Mudstone	-0.8	-6.27
290.9	OP1	Wackestone	-0.24	-7.15
291.2	OP1	Lime Mudstone	0.29	-7.88
291.5	OP1	Lime Mudstone	1.17	-7.81
291.8	OP1	Lime Mudstone	0.03	-8.07
292.1	OP15	Lime Mudstone	-0.14	-7.91
292.4	OP15	Lime Mudstone	-0.16	-7.85
292.7	OP15	Lime Mudstone	-2.99	-7.71

Table A.4: Stable isotope data from Jura Creek section samples. (-) indicate a lack of data.

Sample height (m)	**Lithofacies**	**Lithology**	$\delta^{13}C$	$\delta^{18}O$
0	OP1	Lime Mudstone	-0.94	-5.60
1	OP1	Lime Mudstone	-0.92	-5.34
2	OP1	Lime Mudstone	-0.55	-5.52
3	OP1	Lime Mudstone	-0.59	-5.50
4	OP1	Lime Mudstone	-0.82	-6.65
5	OP1	Lime Mudstone	-0.72	-5.70
6	OP13	Wackestone	-0.62	-5.65
7	OP13	Wackestone	-0.54	-5.31
8	OP13	Wackestone	-0.50	-5.96
9	OP13	Wackestone	-0.20	-5.53
10	OP13	Wackestone	0.49	-3.84
11	OP13	Wackestone	-0.29	-5.66
12	OP13	Wackestone	-0.22	-5.72
13	OP13	Wackestone	-0.28	-5.86
14	OP13	Wackestone	-0.05	-5.19
15	OP13	Wackestone	-0.16	-5.31
16	OP13	Wackestone	-0.06	-5.43
17	OP13	Lime Mudstone	-0.08	-5.22
18	OP13	Lime Mudstone	-0.11	-5.30
19	OP13	Lime Mudstone	0.16	-4.48
20	OP13	Lime Mudstone	0.09	-5.57
21	OP13	Lime Mudstone	0.43	-3.21
22	OP13	Lime Mudstone	-0.02	-5.34
23	OP13	Lime Mudstone	0.24	-3.63
24	OP3	Lime Mudstone	-0.32	-5.44
25	OP3	Lime Mudstone	-0.27	-5.40
26	OP3	Lime Mudstone	-0.45	-5.86
27	OP3	Lime Mudstone	-0.76	-5.67
28	OP3	Lime Mudstone	-0.45	-5.57
29	OP3	Lime Mudstone	-0.34	-5.51
30	OP3	Lime Mudstone	-0.72	-5.54
31	OP3	Lime Mudstone	-0.58	-5.58

32	OP10	Packstone	-0.23	-5.77
33	OP10	Packstone	-0.39	-5.30
34	OP10	Packstone	-0.22	-5.33
35	OP10	Packstone	-0.18	-5.51
36	OP10	Packstone	-0.23	-5.35
37	OP10	Packstone	-0.27	-5.47
38	OP10	Packstone	-0.23	-5.21
39	OP10	Packstone	-0.17	-5.87
40	OP10	Packstone	0.00	-5.67
41	OP14	Wackestone	-0.14	-5.42
42	OP14	Wackestone	-0.20	-5.99
43	OP14	Wackestone	-0.09	-5.72
44	OP14	Wackestone	-0.25	-5.96
45	OP14	Wackestone	-0.17	-6.52
46	OP14	Wackestone	-0.25	-5.92
47	OP14	Wackestone	-0.41	-6.09
48	OP14	Wackestone	-0.75	-6.03
49	OP14	Wackestone	-0.37	-5.61
50	OP14	Wackestone	-0.18	-5.61
51	OP1	Wackestone	-0.48	-5.99
52	OP1	Wackestone	-0.49	-5.86
53	OP1	Wackestone	-0.16	-5.46
54	OP1	Wackestone	-0.04	-5.47
55	OP1	Wackestone	-0.30	-5.68
56	OP1	Wackestone	-0.55	-6.13
57	OP1	Wackestone	-0.67	-5.66
58	OP1	Wackestone	-0.49	-5.64
59	OP1	Wackestone	-0.36	-5.81
60	OP1	Wackestone	-0.33	-6.76
61	OP1	Wackestone	-0.29	-5.78
62	OP13	Wackestone	-0.03	-7.32
63	OP13	Wackestone	0.15	-5.51
64	OP13	Wackestone	0.20	-5.64

65	OP13	Wackestone	0.11	-5.42
66	OP13	Wackestone	-0.04	-5.50
67	OP13	Wackestone	0.16	-5.46
68	OP13	Wackestone	-0.02	-5.64
69	OP13	Wackestone	-0.21	-5.83
70	OP13	Wackestone	-0.26	-6.15
71	OP1	Wackestone	-0.43	-5.70
72	OP1	Wackestone	-0.10	-5.84
73	OP1	Wackestone	-0.30	-6.22
74	OP3	Lime Mudstone	0.18	-5.64
75	OP3	Lime Mudstone	-0.01	-6.35
76	OP3	Lime Mudstone	-0.15	-5.85
77	OP3	Lime Mudstone	-0.24	-5.77
78	OP3	Lime Mudstone	-0.11	-5.70
79	OP3	Lime Mudstone	-0.04	-5.77
80	OP3	Lime Mudstone	-0.25	-5.56
81	OP1	Wackestone	0.02	-4.47
82	OP1	Wackestone	-0.01	-5.22
83	OP10	Packstone	-0.16	-5.50
84	OP10	Packstone	-0.02	-5.57
85	OP10	Packstone	0.14	-4.48
86	OP1	Wackestone	0.27	-5.69
87	OP1	Wackestone	0.70	-5.55
87.5	OP1	Wackestone	0.33	-5.97
93.5	OP13	Wackestone	-0.25	-4.83
94.5	OP13	Wackestone	-0.20	-5.86
95.5	OP13	Wackestone	-0.31	-5.99
96.5	OP15	Lime Mudstone	-0.52	-6.05
97.1	OP15	Lime Mudstone	-0.91	-5.13

Table A.5: Stable isotope data from Crowsnest Pass section samples. (-) indicate a lack of data.

Sample depth (mbs)	**Lithofacies**	**Lithology**	$\delta^{13}C$	$\delta^{18}O$	$Wt\%\ CaCO_3$
1788	IP2	Wackestone	-0.09	-6.49	-
1787	IP2	Wackestone	-0.02	-6.09	-
1786	IP2	Wackestone	0.30	-5.93	-
1785	IP2	Wackestone	0.07	-5.85	-
1784	IP2	Wackestone	0.26	-6.55	-
1783	IP2	Wackestone	0.13	-6.24	-
1782	IP2	Wackestone	0.53	-6.93	-
1781	IP2	Wackestone	0.12	-6.55	-
1780	IP2	Wackestone	0.40	-6.34	-
1779	IP2	Wackestone	0.17	-6.58	-
1778	IP2	Wackestone	0.48	-5.83	-
1777	IP2	Wackestone	0.57	-6.18	-
1776	IP2	Wackestone	0.35	-6.84	-
1775	IP2	Wackestone	0.29	-6.55	-
1774	IP2	Wackestone	0.18	-6.54	-
1772.9	IP2	Wackestone	0.21	-6.78	-
1772	IP2	Wackestone	0.14	-6.22	-
1771	IP2	Wackestone	0.40	-6.08	-
1770	IP2	Wackestone	0.18	-6.43	-
1769	IP2	Wackestone	0.30	-5.99	-
1768	IP2	Wackestone	0.18	-6.47	-
1767	IP2	Wackestone	0.33	-10.2	-
1766	IP2	Wackestone	0.25	-6.46	-
1765	IP2	Wackestone	0.25	-6.46	-
1764	IP1	Packestone	0.07	-6.65	-
1763.47	IP1	Packestone	0.12	-9.79	-
1763.38	IP1	Packestone	0.51	-6.43	-
1763	IP1	Packestone	0.65	-5.89	-
1762.5	IP1	Packestone	-0.01	-5.49	-
1762	IP1	Packestone	2.31	-5.79	-
1761.5	IP1	Packestone	2.53	-5.41	-
1761	IP1	Packestone	0.59	-6.62	-

1760.5	IP1	Packestone	0.44	-6.00	-
1760	IP1	Packestone	0.19	-6.43	-
1759.5	IP1	Packestone	0.01	-6.26	-
1759.33	IP1	Packestone	0.00	-6.02	-
1759.28	B1	Black Shale	-0.53	-7.15	3.97
1759	B1	Black Shale	-0.07	-6.63	15.29
1758.5	B1	Black Shale	-0.60	-6.59	11.83
1758	B1	Black Shale	-0.11	-6.45	26.25
1757.5	B1	Black Shale	-0.32	-5.72	11.04
1757	B1	Black Shale	-	-	1.52
1756.5	B1	Black Shale	-	-	0.55
1756	B1	Black Shale	-	-	0.19
1755.5	B1	Black Shale	-	-	0.62*
1755	B1	Black Shale	-	-	0.21

Table A.6: Stable isotope data from CNRL Tangent section samples. (-) indicate a lack of data. (*) inferred measurements.

Sample depth (mbs)	**Lithofacies**	**Lithology**	$\delta^{13}C$	$\delta^{18}O$	$Wt\%\ CaCO_3$
1961.5	IP2	Dolostone	-4.44	-3.73	-
1961	IP2	Dolostone	-3.81	-2.86	-
1960.5	IP2	Dolostone	-3.92	-3.68	-
1960	IP2	Dolostone	-4.84	-2.84	-
1959.5	IP2	Grainstone	-3.88	-3.92	-
1959	IP2	Grainstone	-3.55	-2.94	-
1958.5	IP2	Grainstone	-3.71	-6.33	-
1958	IP2	Grainstone	-3.02	-6.42	-
1957.5	IP2	Grainstone	-2.16	-10.19	-
1957	IP2	Grainstone	-4.33	-5.69	-
1956.5	IP2	Grainstone	-3.29	-5.14	-
1956	IP2	Grainstone	-3.8	-5.31	-
1955.5	IP2	Grainstone	-3.97	-5.63	-
1955	IP2	Grainstone	-4.75	-4.38	-
1954.5	IP2	Grainstone	-4.18	-5.13	-
1954	IP1	Grainstone	-4.57	-4.59	-
1953.5	IP1	Grainstone	-1.95	-4.83	-
1953	IP1	Grainstone	-2.26	-5.06	-
1952.6	IP1	Grainstone	-7.86	-4.41	-
1952.55	B2	Black Shale	-8.36	-4.35	-
1952.50	B2	Black Shale	-1.85	-1.96	4.63*
1952	B2	Black Shale	-2.66	-5.4	6.25
1951.85	B2	Black Shale	-3.21	-5.49	9.85

Table A.7: Stable isotope data from Gulf Mohawk section samples. (-) indicate a lack of data. (*) inferred measurements.

Appendix B

Compilation of Late Devonian Formations

The following is a summary of formations that were used in figures 5.5, 5.6 and 5.9. Note that these formations do not all classify as black shales but also include calcareous cherts, argillites and siltstones. Certain formations (e.g. Chattanooga shale) have defined ages that extend beyond the Late Devonian, thus the mean averages for wt% inorganic carbon only provide a rough estimate for Late Devonian authigenic carbonate deposition. Sources for this data are predominantly from the USGS National Geochemical Database [USGS, 2008] (https://mrdata.usgs.gov/ngdb/), [Barnes et al., 2019] and this study.

Formation Name	**Number of data points**
Antrime Shale	6
Bakken Formation (Lower)	66
Besa River Formation	22
Chattanooga Shale	151
Devils Gate Limestone	3
Exshaw Formation (Lower)	32
Huron Shale	26
Leatham Formation	16
New Albany	23
Ohio Shale	30
Pilot Shale	88

Sappington Member	5
Slaven Chert	3
Undifferentiated Upper Devonian	19
West Range Limestone	3
Woodford Chert	4
Woodruff Formation	5

Table B.1: Late Devonian shale formations.

Appendix C

Model Parameters

$F_{org} = 12.01 \times 10^{16}\ gC/ky$ [Kump and Arthur, 1999]
$F_{carb} = 48.04 \times 10^{16}\ gC/ky$ [Kump and Arthur, 1999]
Terrigenous Sediment Flux= $1.70 \times 10^{19}\ g/ky$ [Schrag et al., 2013]
Average wt% $CaCO_3$ shale = 4.6%
(Mean average calculated from data in tables:A.1, A.6 and A.7)

$\delta^{13}C_{in}$ = -5 [Kump and Arthur, 1999]
$\delta^{13}C_{basin}$ = -0.35
(Mean average calculated from tables: A.1, A.6 and A.7)
$\delta^{13}C_{platform}$ = 0.5
(Mean average calculated from tables: A.2, A.3, A.4, A.5)
$\delta^{13}C_{restricted}$ = -3.9
(Mean average calculated from table A.7. Note, this average represents data from Gulf Mohawk section only, which is the sole section which is sedimentologicaly defined as a restricted marine depositional environment.)

ϵ_p = 25 [Kump and Arthur, 1999]
ϵ_{mc} = -2 [Zeebe and Wolf-Gladrow, 2001]
ϵ_{ac} = -1.42
(This value represents the difference between $\delta^{13}C_{basin}$ and $\delta^{13}C_{platform}$)
ϵ_{ox} = 2.26
(This value represents the difference between $\delta^{13}C_{basin}$ and $\delta^{13}C_{restricted}$)